Understanding Massive Disk Galaxy Formation Through Resolved Stellar Populations

David Streich

Potsdam, den 20. März 2015

Contents

Contents

List of Figures

List of Figures

List of Tables

Abstract

In this thesis we utilize resolved stellar populations to improve our understanding of galaxy formation and evolution. In the first part we improve a method for metallicity determination of faint old stellar systems, in the second and third part we analyze the individual history of six nearby disk galaxies outside the Local Group.

A New Calibration of the Color Metallicity Relation of Red Giants for HST data: It is well known, that the color distribution of stars on the the Red Giant Branch (RGB) can be used to determine metallicities of old stellar populations that have only shallow photometry. Based on the largest sample of globular clusters ever used for such studies, we quantify the relation between metallicity and color in the widely used HST ACS filters F606W and F814W.

We use a sample of globular clusters from the ACS Globular Cluster Survey and measure their RGB color at given absolute magnitudes to derive the color-metallicity relation. We find a clear relation between metallicity and RGB color; we investigate the scatter and the uncertainties in this relation and show its limitations. A comparison with isochrones shows reasonably good agreement with BaSTI models, a small offset to Dartmouth models, and a larger offset to Padua models.

Even for the best globular cluster data available, the metallicity of a simple stellar population can be determined from the RGB alone only with an accuracy of $0.3\,\mathrm{dex}$ for $[\mathrm{M/H}] \lesssim -1$, and $0.15\,\mathrm{dex}$ for $[\mathrm{M/H}] \gtrsim -1$. For mixed populations, as they are observed in external galaxies, the uncertainties will be even larger due to uncertainties in extinction, age, etc. Therefore caution is necessary when interpreting photometric metallicities.

The Structural History of Nearby Low Mass Disk Galaxies: We study the individual evolution histories of three nearby, low-mass, edge-on galaxies (IC 5052, NGC 4244, NGC 5023).

Using the color magnitude diagrams of resolved stellar populations, we construct star count density maps for populations of different ages and analyze the change of structural parameters with stellar age within each galaxy.

The three galaxies show low vertical heating rates, which are much lower than the heating rate of the Milky Way. This indicates that heating agents, as giant molecular clouds and spiral structure are weak in low mass galaxies.

We do not detect a separate thick disk in any of the three galaxies, even though our observations cover a larger range in equivalent surface brightness than any integrated light study. While scaleheights increase with age, each population can be well described by a single disk. Only two of the galaxies contain a very weak additional component, which we identify as the faint halo. The mass of these faint halos is less than 1% of the mass of the disk.

All populations in the three galaxies exhibit no or only little flaring. While this finding is consistent with previous integrated light studies, it poses strong constraints

Abstract

on galaxy formation models, because most theoretical simulations often find strong flaring due to interactions or radial migration.

Furthermore, we find breaks in the radial profiles of all three galaxies. The radii of these breaks are independent of age, and the break strength is decreasing with age in two of the galaxies (NGC 4244 and NGC 5023). This is consistent with break formation models, that combine a star formation cutoff with radial migration. The differing behavior of IC 5052 can be explained by a recent interaction or minor merger.

The Structural History of Massive Disk Galaxies: We extend the structural analysis of stellar populations with distinct ages to three massive galaxies, NGC 891, NGC 4565 and NGC 7814. While confusion effects due to the high stellar number densities in their central region, and the prominent dust lanes inhibit an detailed analysis of the radial profiles, we can study their vertical structure.

These massive galaxies also have a slower heating than the Milky Way, comparable to the low mass galaxies. This can be traced back to their already thick young populations and thick layers of their interstellar medium.

We do not find a clear separate thick disk in any of these three galaxies; all populations can be described by a single disk plus a Sérsic bulge/halo component. In contrast to the low mass galaxies, we cannot rule out the presence of thick disks in the massive galaxies, because of the strong influence of the halo, that might hide the possible contribution of the thick disk to the vertical star count profiles. However, the faintness of the possible thick disks still points to problems in the earlier ubiquitous findings of thick disks in external galaxies.

2

Zusammenfassung

Es ist noch nicht einmal einhundert Jahre her, dass sich in der "Großen Debatte" die beiden Astronomen Harlow Shapley und Heber Curtis über die Frage stritten, wie groß unsere Milchstraße sei und ob die Spiralnebel innerhalb dieser lägen oder eigene, von dieser getrennte Objekte seien. Seitdem diese Fragen in den darauffolgenden Jahren, insbesondere durch die Arbeiten Hubbles, gelöst werden konnten, hat das Forschungsfeld der Galaxienentstehung und -entwicklung bis heute enorme Fortschritte gemacht, und lässt doch noch so viele Frage offen.

Das Schwierige, aber eben auch das Interessante an der Physik der Galaxien besteht darin, dass sich hier so viele Teilbereiche der (Astro-)physik treffen: von der allgemeinen Relativitätstheorie und der Kosmologie, die die Anfangs- und Randbedingungen geben, über die Dynamik kollisionsfreier Systeme für die Bewegung von Sternen und die Hydrodynamik zum Verständnis der Sternentstehung, bis zur Kernphysik zur Entstehung der Elemente in Sternen und Supernovae. All diese verschiedenen Prozesse (und viele mehr) beeinflussen das Bild der Galaxien, das wir heute sehen.

In dieser Arbeit benutzen wir aufgelöste Sternenpopulationen, d.h. photometrische Messungen einer großen Zahl einzelner Sterne, um die Entstehungsgeschichte von Galaxien zu erforschen. Das Hauptwerkzeug dabei ist das Farben-Helligkeits-Diagramm der Sterne. Seit den frühen Arbeiten Ejnar Hertzsprungs und Henry Russels zu Beginn des zwanzigsten Jahrhunderts ist bekannt, dass Sterne in einem Diagramm, in dem die absolute Helligkeit (oder analog die Leuchtkraft) über der Spektralklasse (oder analog der Effektivtemperatur oder der Farbe) der Sterne aufgetragen ist, nur bestimmte Bereiche belegen. Die genaue Verteilung der Sterne in einem solchen Diagramm wird vor allem durch das Alter und die chemische Zusammensetzung, d.h. die Metallizität, bestimmt. Dies bedeutet, dass man aus der verteilung der Sterne im Farben-Helligkeits-Diagramm Rückschlüsse auf deren Alter und Metallizität, und daraus Rückschüsse auf die Entwicklund einer Galaxie ziehen kann.

Im ersten Teil der Arbeit widmen wir uns der Farb-Metallizitäts-Beziehung von Roten Riesensternen, die genutzt weden kann, um die Metallizität alter Sternenpopulation aus rein photometrischen Messungen zu bestimmen. Wir verbessern diese Beziehung, die im Grundsatz schon lange bekannt ist, für die Filtersysteme des Hubble-Weltraumteleskopes. Ausgehend von einer Probe von 71 Kugelsternhaufen, für die sowohl spektroskopische Metallizitätsbestimmungen als auch Photometrie mit den Hubble Filtern F606W und F814W verfügbar sind, haben wir die Farben-Helligkeitsbeziehung neu bestimmt und die Streuung um diese Beziehung sowie die Unsicherheiten untersucht. Im Vergleich mit theoretischen Sternentwicklungsmodellen zeigt sich, dass die beobachtete Beziehung gut mit den BaSTI-Modellen übereinstimmt, während die Dartmouth-Modelle eine kleine, und die Padua-Modelle eine größere Abweichung aufzeigen.

Desweiteren zeigen wir, dass selbst für die derzeit besten Daten von einfachen, eindeutig alten Populationen, wie die Kugelsternhaufen sie darstellen, eine Metal-

lizitätsbestimmung anhand des Roten-Riesenastes nur mit einer Genauigkeit von 0.3 dex für niedrige Metallizitäten ([M/H]$\lesssim -1$), und mit einer Genauigkeit von 0.15 dex für höhere Metallizitäten durchgeführt werden kann. In komplizierteren Fällen mit gemischten Populationen, wie sie in externen Galaxies häufig zu finden sind, sind die Unsicherheiten noch größer.

Im weiteren Teil der Arbeit erforschen wir die Entstehungsgeschichte von sechs nahen *edge-on* Scheibengalaxien, von denen drei eine Rotationsgeschwindigkeit ähnlich der Milchstraße haben, während drei weitere deutlich kleiner sind. Mit Hilfe der Farben-Helligkeits-Diagramme unterteilen wir deren Sterne in Populationen unterschiedlichen Alters und erstellen Karten der Anzahldichte einer jeden Population. Damit untersuchen wir dann die Abhängigkeit der strukturellen Parameter, wie z.B. Skalenhöhe und -länge, vom Alter der Sterne.

In allen Galaxien finden wir einen Anstieg der Skalenhöhe mit dem Alter, dessen Stärke jedoch deutlich unterhalb dem der Milchstraße liegt. In den drei massearmen Galaxien kann dies durch eine geringere Häufigkeit und Stärke der die Heizung verursachenden Streuzentren (z.B. Riesenmolekülwolken oder Spiralarme) erklärt werden. In den drei massereichen Galaxien hängt dies wahrschinlch mit der bereits intrinsisch dickeren Verteilung des interstellaren Mediums und der jungen Sterne zusammen.

Weiterhin untersuchen wir die Veränderung der Skalenhöhe mit zunehmenden Radius in den Galaxien und finden nur eine geringen Anstieg der Skalenhöhe zu den Außenbereichen der Galaxien hin. Dies ist in Übereinstimmung mit vorherigen Beobachten, stellt jedoch eine bedeutsamen Einschränkung für Galaxiensimulationen dar, in denen oftmals eine starke Aufweitung der Scheiben zu ihrem Rand hin stattfindet.

In keiner der Galaxien entdecken wir eine separate dicke Scheibe. In den massearmen Galaxien kann jede der Population gut durch eine einfache Scheibe beschrieben werden. Darüberhinaus finden wir in zwei Galaxien lediglich eine sehr schwache Halo-Komponente, die mit einer maximalen Masse von nur 1% der Masse der Scheibe aber deutlich schwächer ist als es für eine dicke Scheibe erwartet würde. In den massereicheren Galaxien können die Populationen jeweils mit einer Kombination aus einer Scheibe und einer gemeinsamen Sérsic-Komponente für Halo und Bulge beschrieben werden. Hier können wir die Existenz einer dicken Scheiben nicht mit Sicherheit ausschließen, da die Präsenz einer massiven Halo/Bulge-Komponente eine mögliche Messung der dicken Scheibe verhindern könnte. Allerdings deutet das Fehlen der dicken Scheiben in unseren Beobachtungen darauf hin, dass eventuelle dicke Scheiben deutlich schwächer sein müssen als sie andere Studien bisher gefunden haben.

1. Introduction

The knowledge about the formation and evolution of galaxies has made tremendous progress during the last century. Less than a hundred years ago, it was still unknown, what galaxies are and how large the Milky Way is [see the "Great Debate": Shapley and Curtis, 1921]. About fifty years ago, the canonical model of the formation of the Milky Way through the contraction of a gas cloud was published Eggen et al. [1962]. Later, this smooth formation model was challenged by signs of more irregular structures [starting with Searle and Zinn, 1978], which have their theoretical counterpart in the hierarchical structure formation of cosmology [e.g. Press and Schechter, 1974]. Today, we can form (more or less) realistic galaxies in simulations within a fully cosmological context and observationally study structure, chemistry, and kinematics of galaxies in great detail. But still many aspects of the formation and evolution of galaxies are not understood.

What makes the field of galaxy evolution so intricate – but also interesting – is the variety of physical processes involved on all scales, from general relativity and structure formation in cosmology, over the dynamics of collisionless systems in galaxy dynamics and hydrodynamics of gas clouds for star formation, to nuclear physics for the element synthesis in stars and supernova explosions. All these (and many more) aspects can change the evolution of a galaxy, which makes the simulations very complicated and the interpretations of observations often difficult.

A further difficulty in galaxy evolution is, that we can never see it directly. The timescales involved are much larger than a human life. There are two ways to deal with this problem. By looking at galaxies at different redshifts, we can observe different times in the evolution of the universe and analyze how the properties of galaxy populations change with time. Or we can try to determine the history of individual galaxies. This second approach is often called near-field cosmology or, for the Milky Way, Galactic archeology.

There are many tracers that can reveal the past of a galaxy: Kinematic information are valuable, because structures in phase space can persist much longer than in 3D space, especially in the outskirts of galaxies, where dynamical time scales are long. The metallicity and the abundances of individual elements in stars also allow a look into the past, because its values in the stellar atmosphere hardly change during the life time of a star and, hence, they contain information about the gas cloud from which a star was born many millions or billions of years ago. Also the morphological structure of a galaxy alone can give us hints on its past; e.g. a thin disk is a sign for a quiescent phase of gas accretion, while a dominant bulge hints to an active merger history.

A key tool for studying the history of galaxies and determining ages of their

stellar populations is the color-magnitude diagram (CMD). Since the early work of Hertzsprung [1905] and Russell [1914] it is known that stars cover only certain regions in a plot of luminosity versus spectral type, or analogically magnitude versus color. The position of stars in such a diagram depends on their age and metallicity. Thus, it is possible to extract the age and metallicity of stars from their CMD. For a single star, this is a highly degenerate problem, but for a large number of stars with a common age and metallicity their population parameters can be derived from their distribution in the CMD.

A good age indicator in the CMD is the main sequence, because there is a mass luminosity relation, which also leads to a mass lifetime relation due to the fact the the fuel for nuclear fusion in a star is limited by its mass. From this follows that a star at a given magnitude along the main sequence has a maximum age. This mechanism also makes the evolutionary phases that follow directly after the main sequence stage, namely the helium burning branches for the massive supergiants and the subgiant branch for lower mass stars good age indicators, because they have a clear age luminosity relation. But these evolutionary phases are so short, that in most cases only very few stars can be found there.

In contrast, the red giant branch (RGB) cannot serve as an age indicator, because all low and intermediate mass stars go through a red giant phase. The presence of an RGB can thus only indicate a minimum age of about $2\,\mathrm{Gyr}$. Actually, the RGB does also depend on age, with an older population having a redder RGB, but this age dependance is dwarfed by the metallicity dependance, with a higher metallicity also leading to a redder RGB. This metallicity dependance is often used to estimate the metallicity of resolved old populations.

In this thesis we use the color magnitude diagrams of resolved stellar populations to improve the understanding of the formation and evolution of galaxies. In Chapter 2 we provide a new calibration of the color metallicity relation of old RGB stars in the most commonly used HST filters, using the largest sample of homogeneous globular clusters observations available, and discuss its possibilities and limitations. In Chapter 3 we study the age dependance of the structure of three nearby low mass disk galaxies. This includes the first determination of age–scaleheight relations and age–scalelength relations for galaxies beyond the local group. This study is extended to three massive galaxies in Chapter 4. We conclude with a summary and an outlook in Chapter 5.

2. On the relation between metallicity and RGB color in HST/ACS data[1]

2.1. Introduction

Measuring the metallicity and its gradients in galaxies is a key issue for understanding galaxy formation and evolution.

Outside the Local Group, spectroscopic metallicity determination of (resolved) stars is not feasible at the moment, except for the few very bright supergiants [Kudritzki et al., 2012]. At the same time, the number of available color magnitude diagrams (CMDs) of nearby galaxies is increasing rapidly, e.g. from the GHOSTS [Radburn-Smith et al., 2011] and ANGST [Dalcanton et al., 2009] surveys. These CMDs can be used to derive metallicities.

The color of the red giant branch (RGB) has long been known to depend on the metallicity [Hoyle and Schwarzschild, 1955, Sandage and Smith, 1966, Demarque et al., 1982]. This has been extensively used to measure metallicities of old populations.

There are many ways to convert the color to a metallicity: some authors define indices of an observed population, e.g. the color of the RGB at a given magnitude or the slope of the RGB, [as defined for example in Da Costa and Armandroff, 1990, Lee et al., 1993, Saviane et al., 2000, Valenti et al., 2004], while others measured metallicities on a star by star basis by interpolating between either globular cluster fiducial lines [e.g. Tanaka et al., 2010, Tiede et al., 2004] or analytic RGB functions [calibrated with globular cluster data, e.g. Zoccali et al., 2003, Gullieuszik et al., 2007, Held et al., 2010] or stellar evolution models [e.g. Richardson et al., 2009, Babusiaux et al., 2005], and therefore generating metallicity distribution functions for a population.

Uncertainties that arise from a specific calibration or a given isochrone or cluster template set are typically not well studied. Furthermore, an observational relation for the widely used HST ACS filters F606W-F814W is still missing in the literature[2]. Here we aim to address these shortcomings.

This paper is organized as follows: After an introduction to the data and isochrones we use in chapter 2.2, an observational color metallicity relation is derived in chapter 2.3. A discussion and summary follow in chapters 2.4 and 2.5.

---

[1]This chapter is already published in Streich et al. [2014]. We reproduce here the wording of the published manuscript.

[2]Momany et al. [2005] actually have found such a relation, but they used only three clusters and did not publish the details.

2.2. Data and Isochrones

In this work we use the data of 71 globular clusters observed as part of the ACS Globular Cluster Survey [ACSGCS; Sarajedini et al., 2007] and its extension [Dotter et al., 2011]. These data contain photometry in the F606W and F814W filters and is publicly available at the homepage of the ACSGCS team[3]. For the determination of photometric uncertainties and completeness, the results from artificial star tests are also available. A detailed description of the data reduction is given in Anderson et al. [2008].

To compare the different clusters, it is necessary to transform the apparent magnitudes into absolute, reddening-free magnitudes. For this purpose, we use the distance modulus and color excess from the GC database of W. Harris [Harris, 1996, 2010] and the extinction ratios for the ACS filters given by Sirianni et al. [2005, Table 14]. Metallicities, metallicity uncertainties and α-abundances are taken from Carretta et al. [2009, 2010], if not stated otherwise.

In order to measure the color of the clusters RGBs they must have a sufficient number of stars in the RGB region. We selected therefore only those clusters for our study, which have more than five stars brighter than $M_{F814W} = -2$ and least one star brighter than $M_{F814W} = -3$. A list of the clusters used is given in Appendix A.2 (Table A.1).

For comparison with theoretical models, we use four sets of isochrones: the new PARSEC isochrones [Bressan et al., 2012] and their predecessors, the (old) Padua isochrones[4] [Girardi et al., 2010, Marigo et al., 2008, and references therein], the BaSTI isochrones[5] [Pietrinferni et al., 2006, 2004] and the Dartmouth isochrones[6] [Dotter et al., 2007].

2.3. Results

2.3.1. Color measurement

We use two indices to define the color of the RGB: $C_{-3.0} = (F606W - F814W)_{M=-3.0}$ and $C_{-3.5} = (F606W - F814W)_{M=-3.5}$, i.e. the color of the RGB at an absolute F814W magnitude of -3.0 and -3.5, respectively (see Fig. A.1 for some typical CMDs). Equivalent indices for the Johnson-Cousins filter system were already used by Da Costa and Armandroff [1990], Lee et al. [1993] and also by Saviane et al. [2000]. These indices have the advantage of only depending on relatively bright stars and can therefore be measured in distant galaxies, as well. We use also a third index, the S-index, which is the slope of the RGB [Saviane et al., 2000, Hartwick, 1968]. This slope is measured between two points of the RGB, one at the level of the horizontal branch and the other two magnitudes brighter. While this index needs

---

[3] http://www.astro.ufl.edu/~ata/public_hstgc/
[4] http://stev.oapd.inaf.it/cgi-bin/cmd
[5] http://albione.oa-teramo.inaf.it/
[6] http://stellar.dartmouth.edu/~models/index.html

deeper data, and therefore its usage in extragalactic systems is limited, it has the advantage of being independent of extinction and distance errors.

In order to provide a robust measurement of the color at a given magnitude we interpolated the RGB with a hyperbola of the form:

$$M = a + b \cdot \text{color} + c/(\text{color} + d) \tag{2.1}$$

Such a function was already used by Saviane et al. [2000] to find a one-parameter representation of the RGB; they defined the parameters a, b, c, and d as a quadratic function of metallicity. Here, we are only interested in a good interpolation in sparse parts of the RGB and can therefore use a, b, c, and d as free parameters for each cluster. In order to reduce problems due to contamination, we define a region of probable RGB stars, which also excludes the horizontal branch/red clump part of the CMD. Note that we fit the curve directly to the color/magnitude points of the stars and not to the ridge line of the RGB [in contrast to Saviane et al., 2000]. More details of the fitting process and some example plots with the exclusion region are shown in the Appendix.

To calculate the S-index, we first determined the horizontal branch magnitude of each system by visual inspection of the associated CMDs. This was typically F606W≈0.40 mag, with a 1-sigma variation of 0.10 mag. We measured the color at this magnitude (and at 2 magnitudes brighter) from the fitted RGB used previously, and calculated the S-index as the slope between these points

2.3.2. Metallicity determination

The iron abundance [Fe/H] is often used synonymously with metallicity. However, from the theoretical point of view of stellar evolution, all elements are important in determining the properties of stellar atmospheres. Therefore the color of red giants is expected to depend on the overall metallicity [M/H] rather than on [Fe/H]. Unfortunately, there are very few measurements of the abundances of other elements in globular clusters.

We use here the abundances given in Carretta et al. [2010], who have measured [Fe/H] for all GCs in our sample and have compiled [α/Fe] values for many of them. According to Salaris et al. [1993], these two measurements can be combined to get the overall metallicity with the formula

$$[M/H] = [Fe/H] + \log_{10}(0.638 * 10^{[\alpha/Fe]} + 0.362). \tag{2.2}$$

For clusters that have no individual α measurement, we had to estimate its α abundance. Since the spread of [α/Fe] among globular clusters is rather small, such an estimate will only introduce small errors. In Fig. 2.1, [α/Fe] is plotted against [Fe/H], where we have assumed an uncertainty of 0.05 in the α abundance. The straight line is a linear regression, which we use for the estimation of [α/Fe], where it is not available. The scatter around this regression line is 0.1 dex, which we adopt as the individual uncertainty in the estimated [α/Fe].

2.3.3. Uncertainties

To determine the uncertainties of our color measurements, we performed a bootstrap analysis. The uncertainty in the fit is derived by fitting the RGB of 500 samples that are drawn randomly from the original data. Each re-sample has the same number of stars as the original sample, but may contain some stars multiple times while others are absent.

We also incorporated in the bootstraps a shift due to the uncertainties in extinction and distance. According to Harris [2010], the uncertainty in extinction is of the order 10% in E(B-V), but is at least 0.01 mag, while the uncertainty in distance modulus is 0.1 mag.

The uncertainty in distance is important because we measure the color at a given absolute magnitude. This is particularly significant for the metal-rich clusters where the color of the RGB is strongly dependent on magnitude, as opposed to metal-poor clusters where the RGB is nearly vertical on a CMD. The resulting uncertainty in $C_{-3.5}$ ranges from approximately 0.01 mag at [M/H]=-2 to approximately 0.1 mag at [M/H]=-0.2.

The uncertainties in the metallicity are the sum of the uncertainties in [Fe/H] Carretta et al. [as given by 2009], and in [α/Fe], which we adopt as 0.05 dex for clusters with individual alpha-abundance measurements and 0.1 dex for clusters with estimated values.
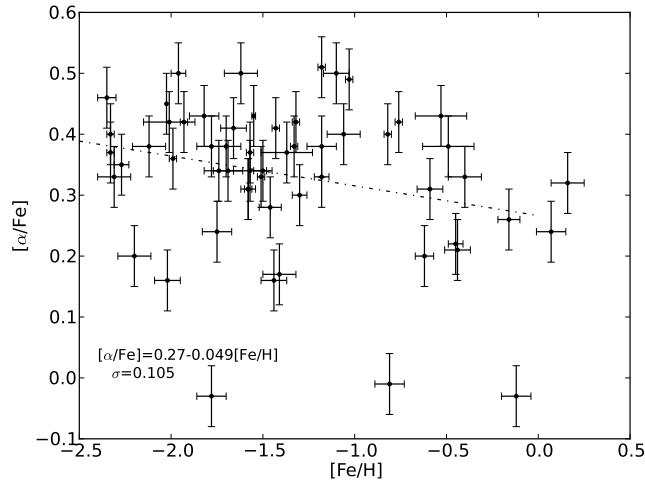
Figure 2.1.: Alpha abundance as a function of [Fe/H] for all clusters in Carretta et al. [2010]. The text in the lower left corner gives the formula of the regression line and the scatter around this line. We used these for estimating the [α/Fe] and its uncertainty for clusters without individual alpha measurement.

Table 2.1.: Fit parameters of the color–metallicity relations.

	a_0	a_1	a_2
$C_{-3.5}$	0.95 ± 0.11	0.602 ± 0.069	0.920 ± 0.015
$C_{-3.0}$	0.567 ± 0.056	0.75 ± 0.12	0.845 ± 0.018
S-index	3.67 ± 0.76	-9.3 ± 1.2	-2.08 ± 0.44

Notes. For $C_{-3.5}$ and $C_{-3.0}$ the color–metallicity relation is exponential: $C_i = a_0 \exp([\mathrm{M/H}]/a_1) + a_2$, for the S-index it is linear $S = a_0 + a_1[\mathrm{M/H}]$.

2.3.4. Color metallicity relation

Using the colors and metallicities described above, we can now look at the color-metallicity relations.

The results are shown in Fig. 2.2. There is a clear relation between RGB color and spectroscopic metallicity. This relation can be parametrized with the function $F606W - F814W = a_0 \exp([\mathrm{M/H}]/a_1) + a_2$. Using the orthogonal distance regression (ODR) algorithm [Boggs et al., 1987, 1992][7], we determined the three parameters, that are shown in Table 2.1. The ODR uses the uncertainties on both variables to determine the best fit. Hence, both the uncertainties in color and metallicity, as described above, are considered during the fit and their effects are included in the final uncertainties of the resulting fit parameters. The residual varinaces for both relations are $\sigma_{res}^2 < 1$, so the adopted uncertainties can explain the observed scatter in the relations.

2.3.5. The S-index

The slope of the RGB as a function of metallicity can be seen in Fig. 2.3. The reported uncertainties of the S-index are a combination of the uncertainties of the RGB fit (determined through a bootstrap analysis as described above) and the uncertainty in the determination of the HB level, which we set here to $\sigma_{HBmag} = 0.1\,\mathrm{mag}$.

As expected, the slope of the RGB gets smaller with increasing metallicity, while at the low-metallicity end the RGB slope is insensitive to metallicity. We have fitted a quadratic function to the data, which is shown in Fig. 2.3 together with the associated best-fit parameters. The choice of a quadratic function for the fit proves to be appropriate as no trends are seen in the residuals. Moreover, the variance of the residuals is only $\sigma_{res}^2 = 1.17$, i.e. the residuals are only slightly larger than expected from the individual measurement uncertainties. The maximum of the parabola is at [M/H]=-2.14, which is beyond the metallicity range of the observed clusters.

---

[7]We used the Python implementation of this algorithm that is part of the Scipy library: `http://docs.scipy.org/doc/scipy/reference/odr.html`
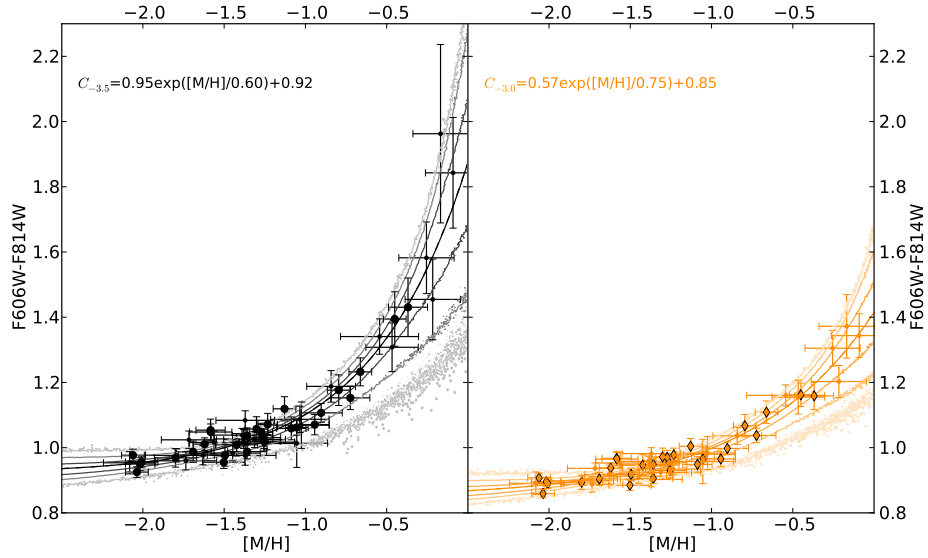
Figure 2.2.: Color of the RGB as function of metallicity, based on the fitted RGBs. Black circles are for the color at $M_{F814W} = -3.5$, orange diamonds for $M_{F814W} = -3.0$. Small points are for clusters without individual alpha measurements. The solid lines are the best-fitting functions as given in the upper left corner and the lighter contours show the 1σ, 2σ and 3σ regions of the fit.

2.4. Discussion

2.4.1. Analyzing residuals

We examine the residuals to look for a possible second parameter that influences the color or slope of the RGB and could produce some scatter in a simple color-metallicity relation. Figures 2.4 and 2.5 show the residuals of the fit of the color-metallicity relation, that is shown in Fig. 2.2, and Figures 2.6 and 2.7 the residuals of the fit to the slope metallicity relation, that is shown in Fig. 2.3.

The residuals as a function of metallicity, [Fe/H] and [α/Fe], are shown in Fig. 2.4 and Fig. 2.6. There is no trend with any of these parameters, neither in the color- nor slope-metallicity relations.

From theoretical studies, the age is known to have an effect on the color of the RGB. In fact, a weak trend of the residuals with age can be seen in Figure 2.5 (upper panel), with older clusters being slightly redder than younger clusters. The slope of the regression lines shown there is 1.94 ± 2.13 for $C_{-3.5}$ and 3.00 ± 1.85 for $C_{-3.0}$, which makes the trend significant for the $C_{-3.0}$ index. In order to quantify the effects of age on the CMD, we analyse the residuals in color space[8] in Figure 2.8. Assuming

---

[8]i.e. we ignore uncertainties in metallicity and only look at the color offset between the data and the best fit relation
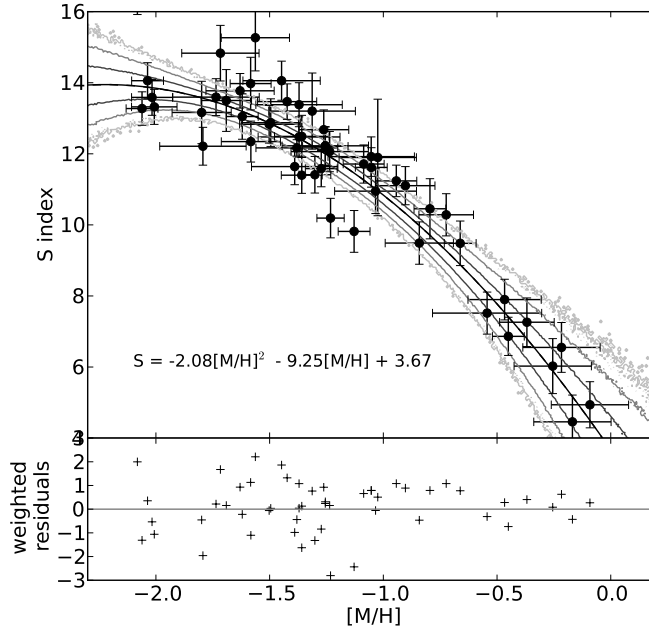
Figure 2.3.: *top panel:* The RGB slope as a function of metallicity. The solid black line is the best-fit quadratic function, as given in the equation in the bottom left. Grey lines give the 1σ, 2σ and 3σ confidence ranges of the the best fit relation. *Bottom panel:* weighted orthogonal residuals, i.e. the orthogonal distances to the best fit line divided by the respective uncertainties.

a typical age for globular clusters of $12.8\,\mathrm{Gyr}$ (as Marín-Franch et al. [2009] do using the isochrones of Dotter et al. [2007]) we can transform the slopes of the regression lines in Figure 2.8 to actual color changes. These are $0.0062 \pm 0.0041\,\mathrm{mag/Gyr}$ for $C_{-3.5}$ and $0.0078 \pm 0.0026\,\mathrm{mag/Gyr}$ for $C_{-3.0}$. While this is a very small effect for the age range observed in our globular clusters ($10\,\mathrm{Gyr}$ to $14\,\mathrm{Gyr}$), it can make significant differences when extrapolated to younger populations; e.g. an $8\,\mathrm{Gyr}$ old population would be bluer than predicted by our relation by about $0.03\,\mathrm{mag}$. Note also that the S index does not show any systematic trends with age.

To test for problems with the extinction values, we looked for trends with E(B-V) and galactic latitude (Fig. 2.5 and Fig. 2.7, middle and lower panel). We do not find any systematics here.

2.4.2. Comparison

We can compare our relations to those derived from stellar evolution models, and to relations from ground-based data transformed to the HST/ACS filter systems.

For comparison with theoretical relations, we use the isochrone set from the Padua,
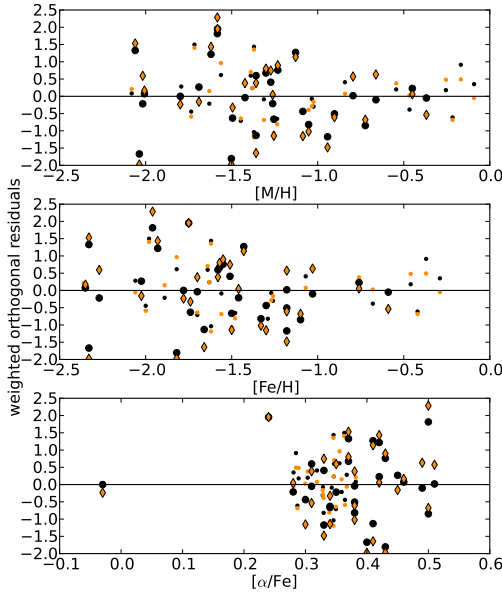
Figure 2.4.: Residuals of the fit of the color-metallicity relation as function of metallicity (upper panel), iron abundance (middle panel) and alpha enhancement (lower panel). Symbols and colors are as in Fig. 2.2.
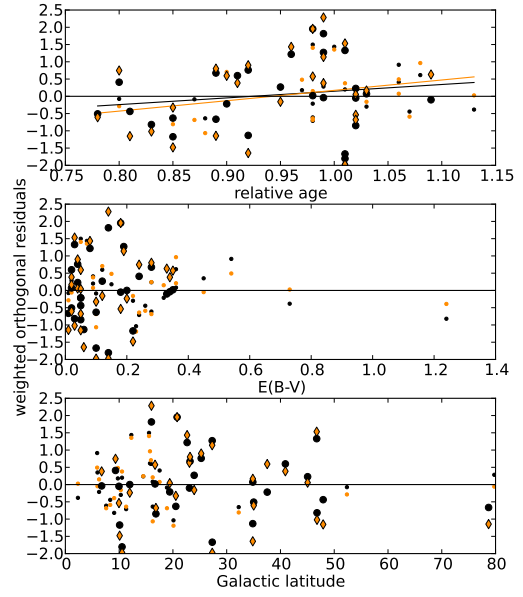
Figure 2.5.: Residuals of the fit of the color-metallicity relation as function of age [upper panel, Marín-Franch et al., 2009], extinction (middle panel) and galactic latitude (lower panel). Symbols and colors are as in Fig. 2.2.

Dartmouth and BaSTI groups. For all isochrone sets we used ages of 8 Gyr, 10 Gyr and 13 Gyr. For Dartmouth, we use α-enhancements of $[\alpha/Fe] = \{0.0, 0.2, 0.4\}$ and for BaSTI models $[\alpha/Fe] = \{0.0, 0.4\}$. The PARSEC[9] and Padua isochrones are available only with solar scaled abundances.

All these isochrone sets show a qualitatively similar behavior. The RGB gets redder (Fig. 2.9) and shallower (Fig. 2.10) with increasing metallicity. A higher age also leads to a redder RGB, but this effect is relatively small. An age difference of 5 Gyr causes the same color difference as a metallicity difference of only 0.1 dex (see Fig. 2.9, top row). At a given total metallicity [M/H], the α-abundance has almost no effect on the RGB color (Fig. 2.9, middle row). This supports the assumption that the color of the RGB is mainly influenced by [M/H] and not [Fe/H].

The increasing curvature of the RGB with increasing metallicity prevents the RGB of some metal rich clusters from reaching F814W$= -3.5$ mag, but bend down at fainter magnitudes. In the Dartmouth models this applies for isochrones with [M/H]> -0.4, in Padua models isochrones with [M/H]> -0.3. However, the BaSTI

---

[9]Actually, Bressan et al. [2012] write about α-enhanced PARSEC isochrones, but these are not (yet) publicly available.
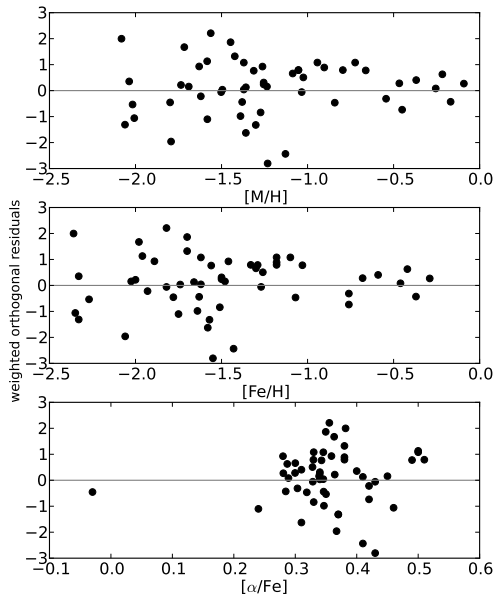
Figure 2.6.: Residuals of the fit of the slope-metallicity relation as function of metallicity (upper panel), iron abundance (middle panel) and alpha enhancement (lower panel).
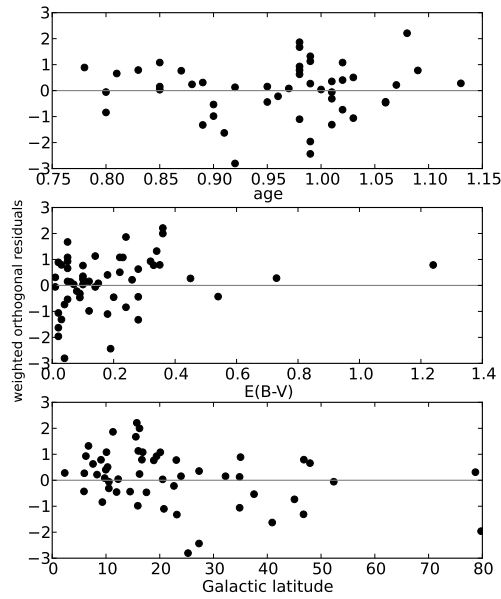
Figure 2.7.: Residuals of the fit of the slope-metallicity relation as function of age [upper panel, Marín-Franch et al., 2009], extinction (middle panel) and galactic latitude (lower panel).

RGB isochrones all reach F814W= -3.5 mag, even at super-solar metallicities. Among our clusters, NGC 6838 ([M/H]= -0.53; it also has very few stars in the RGB) and NGC 6441 ([M/H]= -0.29) are affected by this.

In order to quantify the agreement between our relations and other relations, we have performed a Monte Carlo resampling of our relations by drawing random parameter sets a_i from a multivariate Gaussian distribution with the mean and covariance matrix as given by the best fit. The 68.3%, 95.5%, and 99.7% confidence interval are shown as contours in Figures 2.2, 2.3, 2.9, and 2.10.

As can be seen in Figures 2.9 and 2.10, BaSTI isochrones show good agreement with our observational result. At most metallicities the α-enhanced BaSTI isochrone falls within the the 1σ confidence range of our observational relation; only for [M/H]>-0.4 are the isochrones significantly redder ($> 3\sigma$) and shallower than our relation. The Dartmouth isochrones agree well at very low metallicities, but tend to predict slightly redder colors and shallower slopes at intermediate and higher metallicities. In contrast, results from the Padua isochrones are bluer by almost 0.15 mag and much steeper at lower metallicities, and redder and shallower at the high metallicity end. Determining the reason for this offset is beyond the scope of this paper, but this problem has been known to lead to higher metallicity estimates,
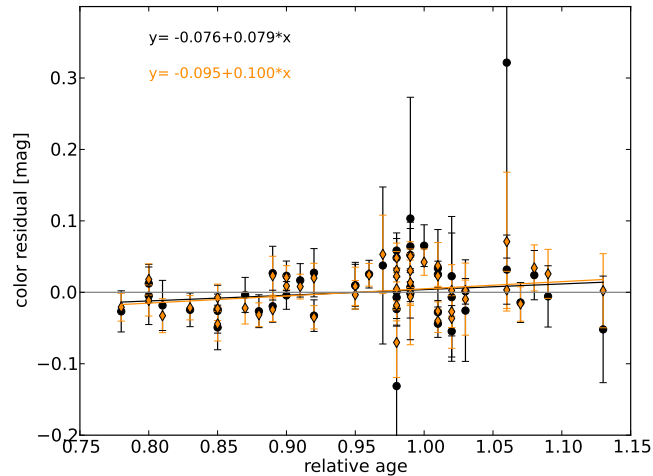
Figure 2.8.: Color residuals of the fit of the color-metallicity relation as function of age. The text gives the regression line formulas for both indices.

when Padua isochrones are used [Lejeune and Buser, 1999].

Existing color-metallicity relations are given in the standard Johnson-Cousin filters. Thus to compare these with our analysis we use the transformations to the HST/ACS filter set described in Sirianni et al. [2005]. Two such transformations are provided, one observationally based and the other synthetic. The former uses observations of horizontal branch and RGB stars in the metal-poor ([Fe/H]=-2.15) globular cluster NGC 2419. This cluster does not contain stars with $(V - I) > 1.3$, hence the transformation at these redder colors are extrapolated and should be used with caution. The transformation is:

$$F606W - F814W = -0.055 + 0.762(V - I) \qquad (2.3)$$

For the synthetic transformation, stellar models with $(V - I) < 1.8$ were used. Hence, for redder colors, the extrapolation should again be treated with caution. The transformation is given as:

$$F606W - F814W = 0.062 + 0.646(V - I) + 0.053(V - I)^2 \qquad (2.4)$$

We use both these transformations on the color-metallicity relations of Saviane et al. [2000], who determined relations for the indices $(V - I)_{-3.0}$ and $(V - I)_{-3.5}$, and for Da Costa and Armandroff [1990, for $(V - I)_{-3.0}$] and Lee et al. [1993, for $(V - I)_{-3.5}$]. To shift these transformations, which are defined for [Fe/H], to the [M/H] scale, we used the same [Fe/H]-[α/Fe] relation as for the data.
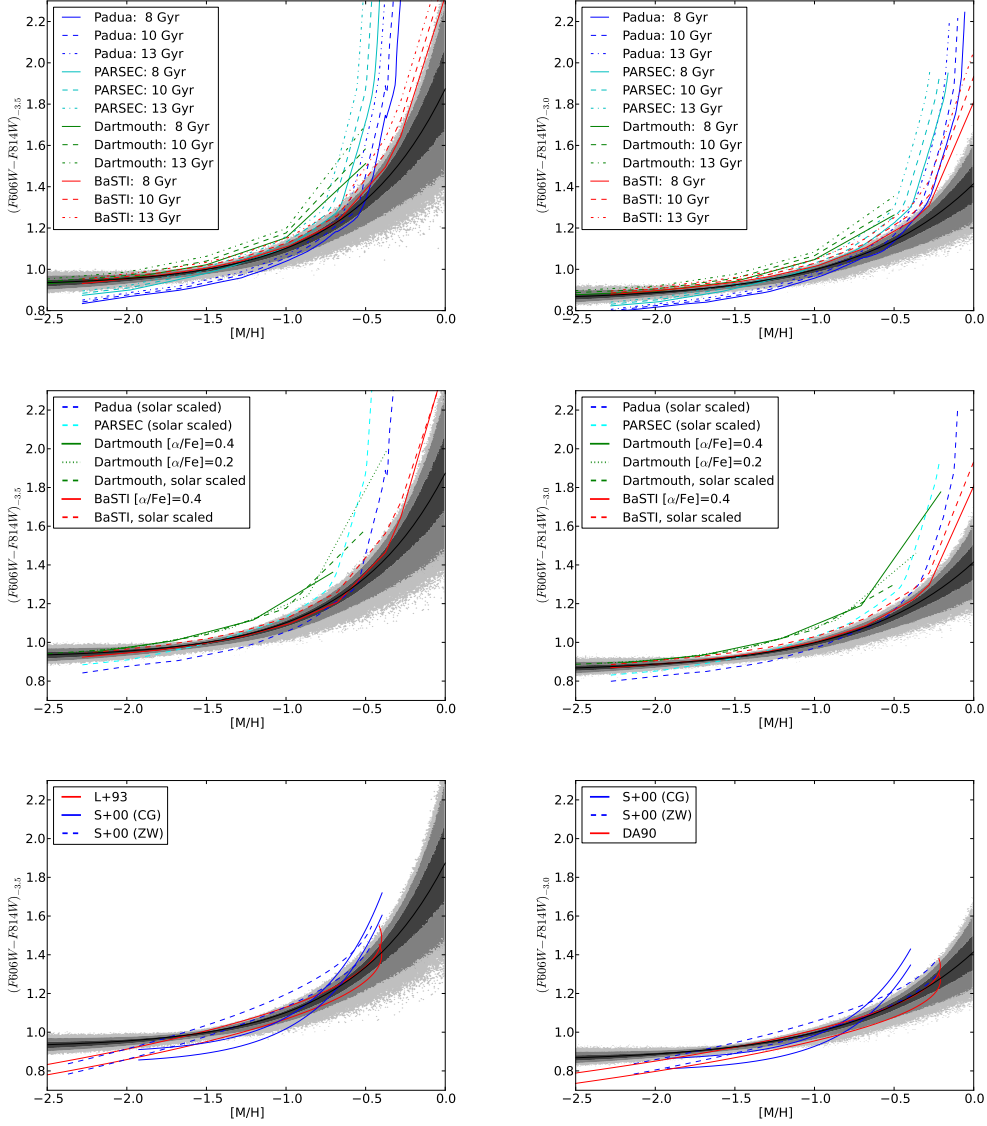
Figure 2.9.: Comparison of color-metallicity relations with theoretical isochrones of different age (top), different α-enhancement (middle), and transformed (V-I) relations (bottom). Left panels compare the relations at $M_{\mathrm{F814W}} = -3.5$, right panels at $M_{\mathrm{F814W}} = -3.0$. The (V-I) relations are taken from Saviane et al. [2000, S+00], Lee et al. [1993, L+93] and Da Costa and Armandroff [1990, DA90]. The S+00 relations are given on two metallicity scales: the ZW scale [Zinn and West, 1984] and the CG scale [Carretta and Gratton, 1997]. Gray contours show the 1σ, 2σ, and 3σ confidence levels of the fit. The two lines for the observational relations are due to differences between the observational and synthetic transformations from Sirianni et al. [2005].

17
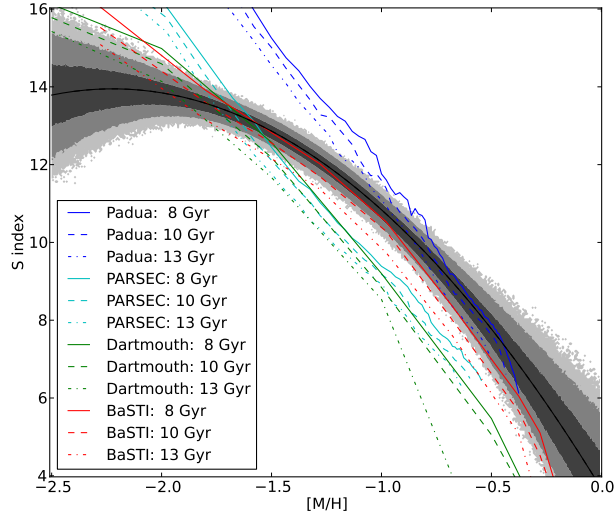
Figure 2.10.: Comparison of the observed S-index metallicity relation with isochrones of varying age. The gray contours show the 1σ, 2σ, and 3σ confidence levels of the fit.

Note that these two transformations have a relative offset of of about $0.05\,\mathrm{mag}$, which can be seen in Fig. 2.9 as the two almost parallel lines in the lower panel.[10]

From Fig. 2.9 it can be seen that these transformed relations are always bluer at the low metallicity end and have a steeper slope than our relations.[11]

Part of this discrepancy can be explained by the different metallicity scales used for the various relations. While we use the metallicity scale of Carretta et al. [2009, C+09], earlier relations were determined either in the Zinn & West scale [Zinn and West, 1984, ZW84] or the Carretta & Gratton scale [Carretta and Gratton, 1997, CG97]. The adopted C+09 scale is comparable to the ZW84 scale; however, the CG97 scale yields higher metallicities for $[\mathrm{Fe/H}] \lesssim -1$ and lower metallicities for $[\mathrm{Fe/H}] \gtrsim -1$ (see 2.11).

Hence, using the CG97 scale will lead to a steeper color-metallicty relation than found from our measurements (see the bottom panel of Fig. 2.9).

---

[10]The offset can already be seen in Sirianni et al. [2005, Fig. 21] as an offset in plot of (V-I) versus V-F606W.

[11]Strictly speaking, we compare slightly different things here: The transformed relations measure the color at constant I-band magnitude, while in this work we have measured the color at constant F814W magnitude. We can ignore this difference here because the difference between I-band and F814W is small. According to the transformations given above, the differences between F814W and I are always smaller than $0.05\,\mathrm{mag}$ and the resulting error in the color measurement of the RGB is always smaller than $0.01\,\mathrm{mag}$ (except for the two reddest clusters, for which it can reach $0.06\,\mathrm{mag}$). Therefore the effect on the total color-metallicity relation is negligible.
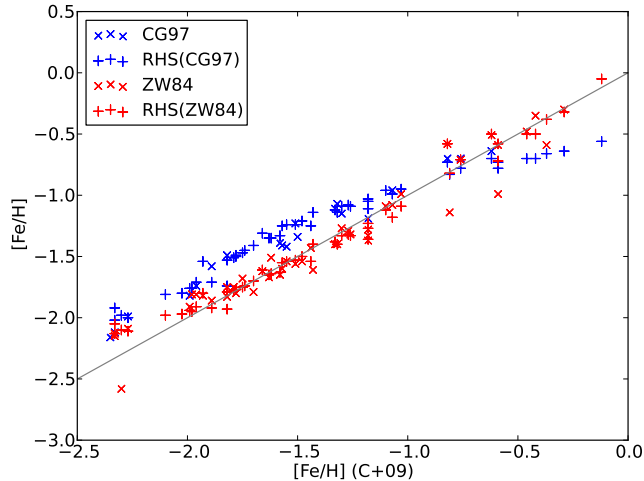
Figure 2.11.: Comparison of different metallicity scales. On the x-axis the C+09 scale, that is adopted in this paper, is shown. Blue crosses show the clusters from Carretta and Gratton [1997], red crosses from Zinn and West [1984]. The plus symbols show the metallicities determined in Rutledge et al. [1997, RHS] based on the Ca triplet, calibrated to both scales.

2.4.3. Inverting the relation

The main purpose of the color metallicity relation is to estimate metallicities of old stellar population. The uncertainties arising from the inverted relation are highly nonlinear. In Fig. 2.12 we plot the difference between the spectroscopic metallicities and the metallicities derived with our relation. It is apparent that for bluer colors (i.e. lower metallicities) the difference can be very large. If the color is near the pole of the metallicity-color function, the formal uncertainties can be infinite. Then only an upper limit on the metallicity can be derived. For all clusters with $C_{-3.5} < 1.2$ (or $C_{-3.0} < 1.0$) the scatter in the metallicity differences is about $0.3\,\text{dex}$. We suggest using this as a minimum uncertainty for metallicities derived from our relation in that color range. For redder colors, the uncertainty drops in half.

2.5. Conclusions and summary

In this paper, we derived relations between the colors and the slope of the RGB and metallicity using data from globular clusters. The details of the relations are summarized in Table 2.1. When using these relations for determining metallicities of old resolved stellar populations, the following points should be kept in mind:

- The color changes very little with metallicity for $[\text{M/H}] \lesssim -1.0$, the slope changes little below $[M/H] \lesssim -1.5$. Therefore, inverting the relation in this
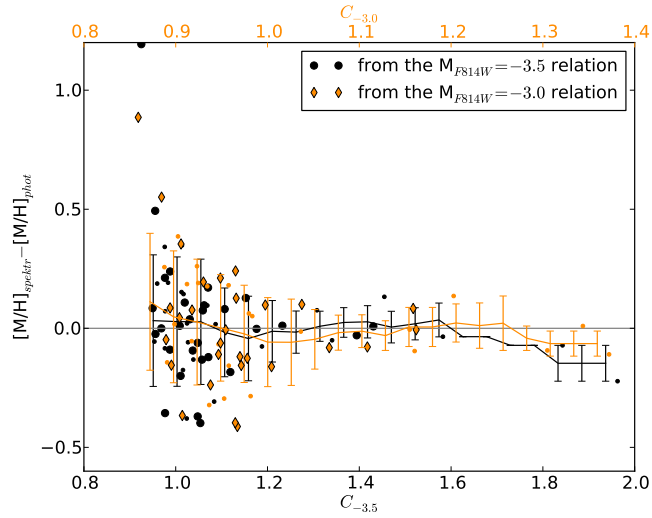
Figure 2.12.: Error distribution of the metallicity determination using the inverted color metallicity relations. Lines with errorbars are the running mean and standard deviation which are computed using a bin width of $0.3\,\mathrm{mag}$ for $C_{-3.5}$ and $0.15\,\mathrm{mag}$ for $C_{-3.0}$. Symbols and colors are as in Fig. 2.2. Note the different scales on the x-axis for the two distributions.

regime introduces large uncertainties. This makes a photometric metallicity determination rather inaccurate in this metallicity range.

- Our relation agrees well with the prediction from BaSTI isochrones. Dartmouth isochrones are slightly redder, Padua isochrones bluer than our data. Thus, for the purpose of determining metallicities of old populations we recommend the use of BaSTI isochrones.

- A comparison with other color-metallicity-relations from the literature, both empirical and theoretical, shows some scatter between these relations. Therefore a comparison of metallicities derived from different methods/relations will introduce systematic offsets. This should be kept in mind whenever the use of a homogenous method is not possible.

3. The age-resolved disk structure of nearby low mass galaxies[1]

3.1. Introduction

Studies of galaxy evolution have always faced the problem of the very large timescales involved: Galaxies only change very slowly over millions and billions of years. The study of galaxy evolution must therefore rely on indirect methods and measurements.

Fortunately, the finite speed of light opens a way to look into the past. By observing galaxies far away we automatically look at galaxies in the past. This allows us to study the evolution of galaxy properties from the early universe to the present time. This leads to a good knowledge of the evolution of the overall galaxy populations, but it does not help with the study of evolution of individual galaxies. The question, how the predecessor of the Milky Way, or any present galaxy in general, has looked like, cannot be answered through such studies.

A different approach to study galaxy evolution is the detailed analysis of present galaxies in order to disentangle their individual histories. The detailed knowledge of the kinematics, ages and chemistry of all stellar populations of a galaxy today would allow inference on its formation and evolution. This approach is often called "Galactic Archeology" or "near-field cosmology". But even without the full knowledge of the kinematical and chemical distribution of the stars, galaxies contain a lot of information about their past. Integrated colors (and their gradients) contain information about the ages and metallicities of the underlying stellar distribution, integrated spectra give valuable information about the ages, kinematics and metallicities and even the temporal evolution of them [e.g. Ocvirk et al., 2008], and deep color-magnitude-diagrams allow the determination of the star formation history (SFR) and metal enrichment function.

Most processes in the evolution of galaxies also leave their signature in the structure of galaxies; e.g. an active merger history will lead to a strong bulge, while the quiescent accretion of gas forms a thin galactic disk. In this paper we will aim for a better understanding of galaxy evolution through the analysis of the vertical and radial structure of stellar populations in nearby galaxy disks.

---

[1]This chapter is submitted to *Astronomy and Astrophysics* and is currently in the first round of the refereeing process.

3. The age-resolved disk structure of nearby low mass galaxies

3.1.1. Vertical structure of disks:

From simple modeling the vertical structure of galactic disks is expected to follow a sech^2 density profile, when an isothermal disk is assumed [van der Kruit and Searle, 1981a], but observationally a centrally more peaked profile, e.g. a sech or exponential profile[2], was found to be more appropriate for the stellar distribution [van der Kruit, 1988, de Grijs et al., 1997]. Such a deviation from the isothermal model can be explained by a mixture of stellar populations with different velocity dispersions, as they are observed in the Milky Way, where the velocity dispersion increases with the age of the stars [Wielen, 1977, Carlberg et al., 1985].

Observations show that a single disk profile is often not sufficient to describe the disk, but a second component with a larger scaleheight is necessary. These so called thick disks were first discovered in S0 galaxies [Burstein, 1979, Tsikoudi, 1979], then in many other galaxies and in our own Milky Way [Gilmore and Reid, 1983]. Later they were found to be ubiquitous [Pohlen et al., 2004, Yoachim and Dalcanton, 2006, Comerón et al., 2011a].

Thick disks were usually seen as a distinct component. In the Milky Way many properties of the thick disk could be determined: It is kinematically hot [e.g. Nissen, 1995, Girard et al., 2006], old, metal-poor and alpha-enhanced [e.g. Fuhrmann, 2008]. Recently, the picture of a clear distinct thick disk has been challenged by Bovy et al. [2012a,b]. They propose the disk to be a superposition of many "mono-abundance population disks", which can be each described by a single disk model.

In many studies it was found that thick disks do not only have larger scaleheights, but also larger scalelengths [Robin et al., 1996, Yoachim and Dalcanton, 2006, Jurić et al., 2008, and others], but this is also questioned for the MW by Bensby et al. [2011] and Bovy et al. [2012b] and recent simulations [Stinson et al., 2013, Bird et al., 2013, Minchev et al., 2014].

The possible formation processes of the thick disk are still unclear. Thick disks could

- already formed thick, e.g. in very massive star formation aggregates [Kroupa, 2002] or turbulent clumpy disks [Bournaud et al., 2009] as they would appear after gas rich mergers [Brook et al., 2004];

- be created from a pre-existing thin disk, which is thickened through internal heating/ scattering by giant molecular clouds or spiral arms[3];

- be created from a pre-existing disk by redistributing stars through outward radial migration [Schönrich and Binney, 2009, Loebman et al., 2011][4];

- result from external heating of an earlier disk by minor mergers [Quinn et al., 1993] or dark matter halo bombardment [Kazantzidis et al., 2008];

---

[2]Often the more general sech$^{2/n}(nz/z_0)$ is used, which also includes an exponential for $n \to \infty$. Those functions differ only in the midplane, for large z they are all asymptotically exponential.

[3]but this effect was shown to be too weak to form the observed thick disks [Villumsen, 1985].

[4]Note that various more recent simulations [Minchev et al., 2012a, Martig et al., 2014b, Vera-Ciro et al., 2014] question the heating effect of radial migration.

- be made of accreted material from satellite galaxies [Statler, 1988, Abadi et al., 2003].

Obviously, also a combination of these processes could play a role, with different ratios in different types of galaxies.

3.1.2. Radial structure of disks:

Disks are thin, rotational supported structures. They show a radial light profile that is (close to) exponential [Patterson, 1940, de Vaucouleurs, 1959, Freeman, 1970]. However, some disks are truncated in the outer parts [van der Kruit, 1979], which means that outside the break radius (at 1.5-6.0 scalelengths) a different exponential is needed to describe the surface brightness profile. In most cases (60%) the outer exponential is steeper than than the inner one, but in 30% of the cases it becomes shallower. Only the minority of 10% do not show a break in their radial light profile at all [Pohlen and Trujillo, 2006].

Disks form through the dissipational collapse of a cooling gas cloud, that forms stars after collapsing. How this leads to an exponential light profile is a still unsolved problem. The two prevailing ideas are: (1) the exponential profile reflects the initial angular momentum distribution of the gas cloud [Freeman, 1970, Larson, 1976] and (2) the viscosity of the gas leads to a redistribution of angular momentum that results in an exponential profile [Lin and Pringle, 1987]. More recently Elmegreen and Struck [2013] suggested that stellar scattering off of transient mass clumps in the disk naturally results in an exponential profile.

A widely accepted idea is that disks form from inside out: at first, gas with low angular momentum gathers in the center and forms stars, and later gas with higher angular momentum gathers around that and forms stars. This behavior is seen in many different models [e.g. Larson, 1976, White and Frenk, 1991, Burkert et al., 1992, Mo et al., 1998, Naab and Ostriker, 2006, Brook et al., 2006] and leads to negative age and metallicity gradients [e.g. Matteucci and Francois, 1989, Chiappini et al., 1997, Boissier and Prantzos, 1999, Prantzos and Boissier, 2000]. Observational evidence for the inside out formation of disks can be found in age gradients directly [Muñoz-Mateos et al., 2007, MacArthur et al., 2009, Williams et al., 2009], in metallicity gradients [MacArthur et al., 2009], color gradients [de Jong, 1996] and directly in the change in galaxy sizes with redshift [Patel et al., 2013, van der Wel et al., 2014] .

The interpretation of radial gradients has to take into account that stars can change their radial position in the galaxy with time. It has long been known that scattering effects can blur and heat galactic disks. But only relatively recently it has been found that stars can also change their radial position and still keep the circular nature of their orbits [Sellwood and Binney, 2002]. This radial migration process dramatically changes the chemical evolution and the metallicity gradients [Schönrich and Binney, 2009] and leads to a radial extension of disks [Roškar et al., 2008, Sánchez-Blázquez et al., 2009]. It might also cause the formation of a thick disk component [Loebman et al., 2011].

While the physical reason for the exponential disk profiles is still unclear, the reasons for a break in the radial profiles are even less understood. The breaks occur at a similar surface brightness in all galaxies [Kregel et al., 2004], at the same radius for all heights above the plane and for all populations [Pohlen et al., 2007, de Jong et al., 2007]. They can be observed even at redshifts of $z \approx 1$ [Pérez, 2004, Trujillo and Pohlen, 2005]. Truncated disks have a color minimum at the break radius, while anti-truncated, i.e. disks with a larger scalelength beyond the break, and unbroken disks only show a flattening of their color profile at large radii, both in the local universe and at higher redshifts ($z \approx 1$) [Bakos et al., 2008, Azzollini et al., 2008a,b].

Also the nature of breaks is still discussed. Bakos et al. [2008] claim that a break is only due to a change in stellar populations and that the mass profile is unbroken, but this is contrary to results from the GHOSTS survey [de Jong et al., 2007, Radburn-Smith et al., 2012], which show breaks in star counts of different populations. Also in simulations the break is connected to a steepening of the stellar mass profile [Roškar et al., 2008, Sánchez-Blázquez et al., 2009]. These simulations predict a minimum of the age distribution at the break radius and a smooth metallicity profile.

The numerous models of break formation can be roughly divided into two groups. The first connects the break to a break in star formation, either due to a limited gas distribution [van der Kruit, 1987] or to a star formation threshold [Fall and Efstathiou, 1980, Kennicutt, 1989, Dopita and Ryder, 1994, Schaye, 2004, Elmegreen and Hunter, 2006]. The second group contains models which dynamically redistribute stars after their formation, either due to secular angular momentum redistribution [Debattista et al., 2006, Foyle et al., 2008, Minchev et al., 2012b] or tidal interactions [Gnedin, 2003, Kazantzidis et al., 2008].

In this paper we examine the structure of different stellar populations with distinct ages to study the temporal evolution of galaxy disks. In Section 3.2 we explain the data and methods, in Section 3.3 we present our results, discuss them in Section 3.4 and conclude with a summary in Section 3.5.

3.2. Data and Methods

3.2.1. The GHOSTS Survey

GHOSTS is an extensive, multi-cycle HST survey to image the resolved stellar populations in the halos and outer disks of 17 nearby disk galaxies. The galaxies in the GHOSTS sample span a wide range of morphologies, from Sab to Sd, and masses (with V_{rot} ranging from $80\,\mathrm{km/s}$ to $230\,\mathrm{km/s}$).

The survey was performed using the cameras ACS and WFC3 and filters F814W and F606W. These filters were chosen because they have a high throughput and because red giants, which are supposed to be the majority of (bright) stars in the assumed old halos, have the flux maximum in this wavelength range.

The observations were designed so that red giant branch stars could be well resolved; usually the observations reach at least a S/N=10 at 1 mag below the tip of the red giant branch. For the nearer galaxies ($D < 5$ Mpc this requirement could be obtained with in the limits for HST SNAP programs, while for farther galaxies GO programs were done. The dedicated GHOSTS observations were complemented with all archived observations fulfilling the same requirements. The current GHOSTS database contains data from cycles 12 to 21.

3.2.1.1. GHOSTS Data Reduction

All details of the observations and the data reduction can be found in Radburn-Smith et al. [2011, for the ACS data] and Monachesi et al. (in prep., for the WFC3 data). Here, we only summarize the main points of the data reduction.

After basic data reduction (bias subtraction, flat-fielding, cosmic ray and bad pixel identification, drizzling), the program DOLPHOT, which is a modified version of HSTphot [Dolphin, 2000], is used for the identification and photometric measurements of the stars. We performed PSF photometry using the TINY TIM point-spread functions (PSF). Together with the positions and magnitudes of the stars, DOLPHOT reports many photometric parameters for diagnostic purposes, i.e. sharpness, roundness, crowding, signal-to-noise etc. These parameters can be used to discriminate between stars and other objects.

We defined a set of culls on the diagnostic parameters that ensure that a maximal number of stars and a minimal number of contaminants is detected. To estimate the number of contaminants that are expected for a given set of culls, observations from the Hubble archived are chosen which are aimed at high-redshift objects at high galactic latitudes. These observations are expected to be free of any detectable stars and thus the culls should minimize the detections in these fields. At the same time, the culls are requested to maximize the recovery fraction of artificial stars that are put into the same images. We call the culls we choose with those two requirements *sparse field culls*, because they are optimized for fields with low star cont numbers.

A second set of culls was optimized for a high recovery fraction of artificial stars in very crowded regions. This is called the *crowded field cull*. Compared to the sparse field cull it has a higher number of contaminants by about 60%, but at the same time the recovery fraction of stars in crowded regions is more than twice as high as for the sparse field culls. Since the typical number of contaminants is very small (about a few dozens per ACS field) compared to the number of stars in crowded regions (a few thousands per ACS field), the larger number of real detections outweighs the increased number of contaminants. For more details on the determination of optimal culls we refer the reader to the appendix of Radburn-Smith et al. [2011]. In the following we will always use the crowded field culls, if not stated otherwise.

To further increase the reliability of our star catalogs, we use SExtractor [Bertin and Arnouts, 1996] to create a segmentation mask which masks out all extended sources, i.e. background galaxies or nearby bright stars.

Table 3.1.: Details of the galaxy sample.

name	RA[1]	DEC[1]	z_0[1]	PA[2]	Incl.[2][a]	t[2]	V_{max}[2]	$(m-M)_0$[3]	dist[3]
	[°]	[°]	["]	[°]	[°]		[km/s]	[mag]	[Mpc]
IC 5052	313.0068	-69.1933	13.35	-38.0	90.0	7.1	79.8	28.76	5.6
NGC 5023	198.0525	44.0412	9.29	27.9	90.0	6.0	80.3	29.06	6.5
NGC 4244	184.3736	37.8071	22.14	42.2	88.0	6.1	89.1	28.21	4.4
NGC 4631	190.5334	32.5415	13.74	82.6	85.0	6.5	138.9	29.34	7.4
NGC 891	35.6392	42.3491	11.86	22.8	88.0	3.0	212.2	29.80	9.1
NGC 7814	0.8120	16.1454	-	134.4	70.6[a]	2.0	230.9	30.80	14.4
NGC 4565	189.0866	25.9877	13.67	-44.8	90.0	3.2	244.9	30.38	11.9

Notes. [1] Right ascension, declination and scaleheights from K-Band fits by Seth et al. [2005a];[2] position angle, inclination, morphology index t and rotational velocity from HyperLEDA [Paturel et al., 2003]; [3] distance modulus and distance from Radburn-Smith et al. [2011].
[a] Note that while we list the inclination value from HyperLEDA here, our selection of edge-on galaxies was made based on a visual inspection of the images. Therefore we have included NGC 7814 due to its thin and straight dust lane, but excluded NGC 253 due to its visible spiral structure.

3.2.1.2. Sample of edge-on Galaxies

The GHOSTS sample contains seven edge-on galaxies that have data on their disks[5], which we included in our analysis (see Table 3.1). In this first paper we examine the three low mass galaxies (75 km/s< V_{rot} < 100 km/s). The three massive galaxies (V_{rot} > 200 km/s will be covered in a subsequent paper. The intermediate mass galaxy NGC 4631 will be analyzed in an additional paper, because it needs a special treatment due to the strong effects of the interaction with its neighbor NGC 4627.

3.2.2. Age Selection in the CMD

Color-magnitude diagrams (CMD) allow us to dissect the stars into populations of different ages. The CMDs of the GHOSTS galaxies show clear distinguishable structures, which belong to different stellar populations (see Fig. 3.1). These populations are:

Main Sequence: Main sequence stars burn hydrogen to helium in their cores. Since the GHOSTS data covers only the luminous part of the CMD (M_{F814W} > −2), we can only observe the upper main sequence with massive ($M > 6\,M_\odot$) stars.

---

[5]An eighth galaxy, NGC 5907, turned out to be farther away (D= 16.8 Mpc) than previously measured. Therefore its CMD is not deep enough for our analysis, and it was excluded from further observations due to the long exposure times that would have been needed.
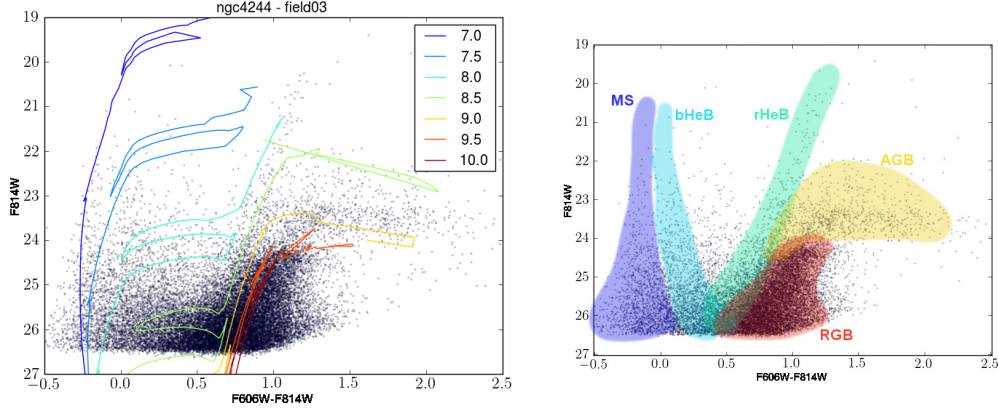
Figure 3.1.: *left*: Typical CMD of the GHOSTS survey (taken from NGC 4244) over-plotted with stellar isochrones from the Padova models [Girardi et al., 2010]. The legend shows the log(age) of the isochrones. *right*: Sketch of the different populations in the CMD.

Blue and Red Helium Burning Branch: When massive stars have depleted their central hydrogen, they start hydrogen shell burning until helium ignites in the center. When this happens, they are then more luminous and cooler than the main sequence and reside on the Helium Burning Branches. Similar to the main sequence more massive stars are more luminous. Within the GHOSTS limits we can detect helium burning branch stars with $M > 3\,M_\odot$.

Red Giant Branch: When a low mass star $M < 1.5\,M_\odot$ has depleted its central hydrogen, it starts burning hydrogen in a shell around a degenerate helium core. While the mass of the helium core grows with time, the stars moves upward in the CMD along the Hayashi line and form the Red Giant Branch. When the degenerate core reaches a mass of about $0.45\,M_\odot$, helium burning sets in and the star leaves the RGB. Since, for metal-poor populations ([Fe/H]<-0.7) this onset mass is almost independent of the initial mass or the age of the star, the tip of the RGB is well defined at $M_{F814W} \approx -4$.

Asymptotic Giant Branch: After low to intermediate mass stars have depleted their central helium, they start ascending from the horizontal branch/red clump region towards higher magnitudes parallel to the RGB, while burning helium in a shell. Large parts of the AGB do overlap with the RGB in the CMD, but the relatively massive stars ascend beyond the tip of the RGB and can be seen separately above the RGB.

In order to define age separated stellar populations, we have defined five CMD bins (see Fig. 3.2, left). These CMD bins were designed to cover different ages with as little overlap in age as possible (see Fig. 3.2, right). To define the bins and determine

Table 3.2.: Properties of the age distribution of the defined stellar populations, derived from models assuming a constant SFR and a flat metallicity distribution.

	MS	upHeB	lowHeB	AGB	RGB
mean(age) [Gyr]	0.028	0.089	0.21	1.36	5.07
std(age) [Gyr]	0.041	0.066	0.19	0.94	3.96
median(age) [Gyr]	0.010	0.082	0.18	1.16	4.41
10-percentile	0.005	0.037	0.12	0.52	0.81
90-percentile	0.037	0.146	0.27	2.52	11.5

their age distributions, we have used a synthetic CMD created with MATCH [Dolphin, 1997, 2002] and using the Padova isochrone set [Girardi et al., 2010, Marigo et al., 2008]. A constant star formation rate (from log(t)=10.15 to log(t)=6.6) and a flat metallicity distribution function (between [Z]=-2.2 and [Z]=0.2) were used.

The populations defined by these CMD bins are:

main sequence (MS, blue): contains mainly stars younger than 40 Myr, but stars up to 300 Myr can contribute to this population.

upper helium burning branches (upHeB, cyan): contains mainly stars between 40 Myr and 150 Myr, with smaller contribution from stars between 25 Myr and 300 Myr.

lower helium burning branches (lowHeB, green): contains mainly stars between 100 Myr and 400 Myr, with only little contamination by different ages.

asymptotic giant branch (AGB, yellow): contains mainly stars between 0.5 Gyr and 2 Gyr, but it might also contain a few stars as young as 350 Myr or as old as 6.5 Gyr

red giant branch (RGB, red): contains mainly stars older than 3.0 Gyr, but also younger AGB stars and even lower HeB stars may contribute here.

Throughout this paper, we use the median ages of these populations (see Table 3.2) for all plots showing the ages of the populations, and their errorbars give the range between the 10-percentile and the 90-percentile of the age distributions.

3.2.3. Creating Stellar Density Maps

We used the star catalogs of the GHOSTS survey (see Sect. 3.2.1) to create star count density maps for each of the populations defined in Sect. 3.2.2. The raw star count maps are simple two-dimensional histograms of the stars in each CMD selection box. The bin size of the maps is $(7.2'')^2$. These raw star count maps are then corrected for incompleteness effects, using completeness maps created from the artificial star tests, and for masked regions in the original images. In overlapping regions of different
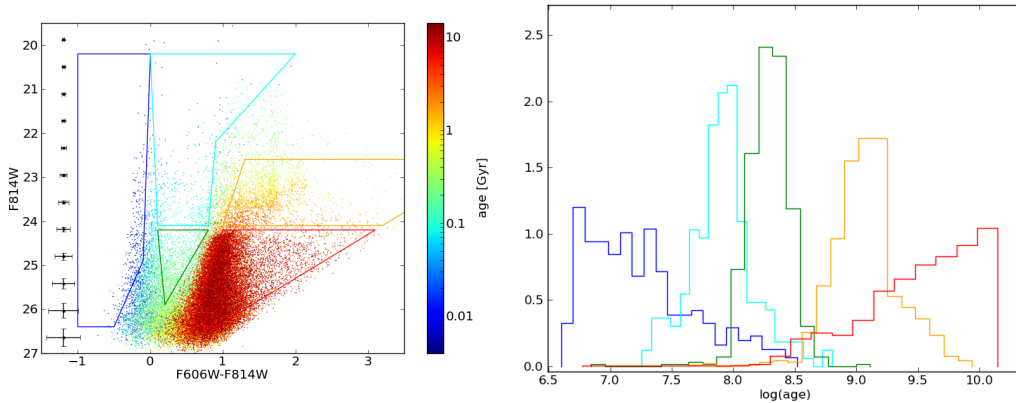
Figure 3.2.: *left*: An artificial CMD generated with a constant star formation rate and a flat metallicity distribution function ($-2.2 < [Z] < 0.2$). The colored boxes are the population boxes as described in the text. Stars are colored according to their age (see color-bar). *right*: The age distribution of stars in the five population boxes in the left figure.

fields the average of all fields is used. Finally bins with a completeness lower than 0.5 and bins which contain more than 40% masked area in the original image are masked out.

Completeness correction   Not all stars that are in our field can be reliably measured. Stars near the detection limit might be missed due to statistical variations in the photon flux, stars in crowded or bright sky regions might also be missed. We quantify the completeness of our observations through the recovery fraction from the artificial star tests. For each population the fraction of recovered artificial stars is calculated in each spatial bin, i.e. for each population we create a completeness map. Note that this is different from the approach in the GHOSTS DR1 [Radburn-Smith et al., 2011], where the completeness was presented as a function of magnitude, color and sky brightness, but not as a function of position. The change in the approach is necessary, because we found that the completeness can vary within a field independent of sky brightness, e.g. due to CTE effects.

3.2.4. Fitting Methods

In order to quantify the structural parameters of the disks, we fit different galaxy models to the star count maps. Because the star count maps often contain very low numbers of stars per pixel, the quality of the fit has to be calculated with a Poissonian likelihood estimator, instead of the often used χ^2. Such a Poissonian likelihood estimator was first proposed by Cash [1979] and is strongly argued for by Dolphin [2002]. It can be derived in the same way as the χ^2 statistics, but starting

from the Poissonian probability function

$$P_i = \frac{m_i^{n_i}}{n_i!} e^{-m_i}, \tag{3.1}$$

with m_i denoting the expected counts in pixel i in the model and n_i the observed counts in that pixel. Then the maximum likelihood model can be obtained by minimizing the Poissonian likelihood ratio (PLR)[6]

$$PLR = -2\ln P = -2\sum_i \left(n_i \ln m_i - m_i + n_i(1 - \ln n_i) \right). \tag{3.2}$$

Determining Scaleheights: To analyze the vertical structure of the population at different radii from the galaxy center, we fit an isothermal sheet model [van der Kruit and Searle, 1981a] to the stellar surface density profiles. The model reads:

$$n(z) = n_0 \operatorname{sech}^2 \left(\frac{z + z_c}{z_0} \right) + n_{bg}, \tag{3.3}$$

where n_0 is the star count density in the midplane, z_c the center of the stellar distribution relative to the galaxy's midplane (defined through the center coordinates and the position angle of the galaxy), z_0 the scaleheight and n_{bg} the surface density of contaminants.

We use an isothermal model despite the fact that many observations found a more peaked function to better fit the vertical light profile of galaxies. We do this, because we fit our model to distinct stellar population of well defined ages, for which the isothermal assumption is more justified than for the overall stellar content of a galaxy.

2D fits: In order to measure scalelengths, scaleheights and break radii we fit a simple model of an edge-on disk with a broken exponential as radial profile to the 2D maps of star count density:

$$n(x, z) = n_{bg} + n_0 \operatorname{sech}^2 \left(\frac{z - z_c}{z_0} \right) n(x) \tag{3.4}$$

with

$$n(x) = |x - x_c| \begin{cases} \mathrm{K}_1 \left(\frac{|x - x_c|}{h_{r,i}} \right) & \text{for } |x - x_c| < r_b \\ \frac{\mathrm{K}_1(r_b/h_{r,i})}{\mathrm{K}_1(r_b/h_{r,o})} \mathrm{K}_1 \left(\frac{|x - x_c|}{h_{r,o}} \right) & \text{for } |x - x_c| > r_b \end{cases}, \tag{3.5}$$

---

[6]Note that the last term in the sum only depends on the data which of course does not change during the fit. Therefore it could be omitted without effecting the best fit model, but including this term gives the advantage that each term under the sum is greater than zero (which is important for some numerical minimization routines) and that for large n_i the PLR converges to the same value as a χ^2.

where x_c is the x-coordinate of the galaxy's center, $h_{r,i}$ the inner and $h_{r,o}$ the outer scalelength, and r_b the break radius. $K_1(x)$ is the modified Bessel function of the second kind and $xK_1(x)$ is the projected surface density of an exponential disk seen edge-on, i.e.[7]

$$I(x) = \int\limits_{-\infty}^{\infty} \exp\left(-\frac{\sqrt{x^2 + y^2}}{h_r}\right) dy = 2 \int\limits_{x}^{\infty} \frac{r \exp(-\frac{r}{h_r})}{\sqrt{r^2 - x^2}} dr = 2xK_1\left(\frac{x}{h_r}\right). \qquad (3.6)$$

This model assumes a constant scaleheight along the disk. As we will see in Sect. 3.3, this assumption is justified. Note also that the model in Equation 3.4 is a single disk model, i.e. it does not contain any thick disk or bulge or halo components. This will of course limit its applicability; but for the low mass galaxies in our sample, this model is sufficient to describe the distribution of stars in each population.

For performing the actual 2D fits we use the program IMFIT[8] [Erwin, 2014], which permits the use the Poisson likelihood ratio statistics for the minimization process. IMFIT is also designed to make the inclusion of additional image functions simple and we have extended it with the broken edge-on disk model of equation 3.4.

3.2.5. Spitzer Data

For a comparison of the star count maps from GHOSTS with integrated light observations we use data from the InfraRed Array Camera [IRAC; Fazio et al., 2004] of the Spitzer Space Telescope. The data was reduced within the *Spitzer Edge-On Disk Galaxies Survey* project [Holwerda et al., 2006]. We give here a short description of the data and the reduction process.

The data contains mosaics of 32 edge-on disk galaxies in all four IRAC channels. It was taken in a dedicated GO program (GO 20268: The Formation of Dust Lanes in Nearby Edge-on Disk Galaxies; PI: R. S. de Jong) and complemented with archival data. The observing strategy and data reduction was set up in such a way that the final data products are equivalent in quality to the data products from the Spitzer Infrared Nearby Galaxy Survey [SINGS; Kennicutt et al., 2003].

The *IRAC* Basic Calibrated Data (BCD), together with the corresponding uncertainty (BUNC) and individual bad pixel mask (BDMSK), were retrieved with *Leopard* [Spitzer Software Team, 2008]. The data reduction was performed with the standard *Spitzer* Science Center's pipeline for raw *IRAC* data ; the mosaics were created with the MOPEX software [Spitzer Post-BCD Tools Team and Science User Support Team, 2012]. The reduction process includes bias and flatfield corrections, conversion from engineering to scientific units, addition of WCS coordinates, combination of single exposures into a mosaic and a removal of cosmic rays. The final images are aligned with the galaxy's major axes and have a pixel size of 0.75 arcsec. In addition to the images, noise maps and mask files were created.

---

[7] Note that this derivation assumes an infinite exponential disk, while we actually model a truncated disk. Therefore the model is not fully self-consistent.

[8] http://www.mpe.mpg.de/~erwin/code/imfit

The IRAC channels 1 and 2, with effective wavelengths of $\lambda \approx 3.6\,\mu m$ and $\lambda \approx 4.5\,\mu m$, respectively, trace mainly stellar emission and have the advantage of being nearly unaffected by dust. We use channel 1 to determine the structural parameters of the overall stellar population in our galaxies, by fitting the edge-on disk model (Equation 3.4) to the [3.6] data.

The IRAC channels 3 and 4, with effective wavelengths of $\lambda \approx 5.7\,\mu m$ and $\lambda \approx 8.0\,\mu m$, respectively, trace the emission of hot dust and polycyclic aromatic hydrocarbon molecules, but have also contributions from stellar emission. We use the data from channel 1 and 2 to estimate the stellar contribution to the light in channel 4 [as described in Pahre et al., 2004], and subtract it from the channel 4 data to create images of the nonstellar emission in the galaxies. We fitted the same edge-on disk model of Equation 3.4 to these nonstellar images to get estimates of the scaleheight and -length of the dust in our galaxies.

3.3. Results

In this section first the vertical stellar density profiles are studied at different galactocentric distances, followed by the radial distributions at different heights above the midplane. The sections concludes with a discussion of the observations and a comparison with integrated light observations.

3.3.1. Vertical Profiles

We have split the observed stars into the five age groups described in Sect. 3.2.2. The stellar density maps for all of these populations can be seen in Fig. 3.3. It is obvious that older populations are more extended than young ones. While this can be seen to some extent also in the radial direction, it is clearly evident in the vertical direction.

The thickness of the disks can be well examined in Fig. 3.4. There, vertical star count profiles are shown at different radial positions within the galaxies. The RGB stars (show in red) are the dominant population in all our galaxies at all radii; they have the highest star count density and the largest vertical extend. In order to quantify the thickness of each population, we have fitted a sech^2 model each radial bin (see equation 3.3), the fits are shown as dotted line in Fig. 3.4. Remarkably, each profile can be fitted well by a single sech^2 profile (plus background). There is no need to add a second component, i.e. a thick disk (for more details on this, see Sect. 3.3.3.2). It is also noteworthy that most profiles show a clear peak in the center and only the RGB profiles near the galaxy centers have a central dip. Such dips are often observed in vertical profile studies [e.g. Seth et al., 2005b] and usually attributed to the extincting effects of dust. We will discuss this issue further in Sect. 3.4.1.

The radially averaged scaleheights as a function of age are plotted in Fig. 3.5. In general an increase of scaleheights with age can be seen: While the three youngest
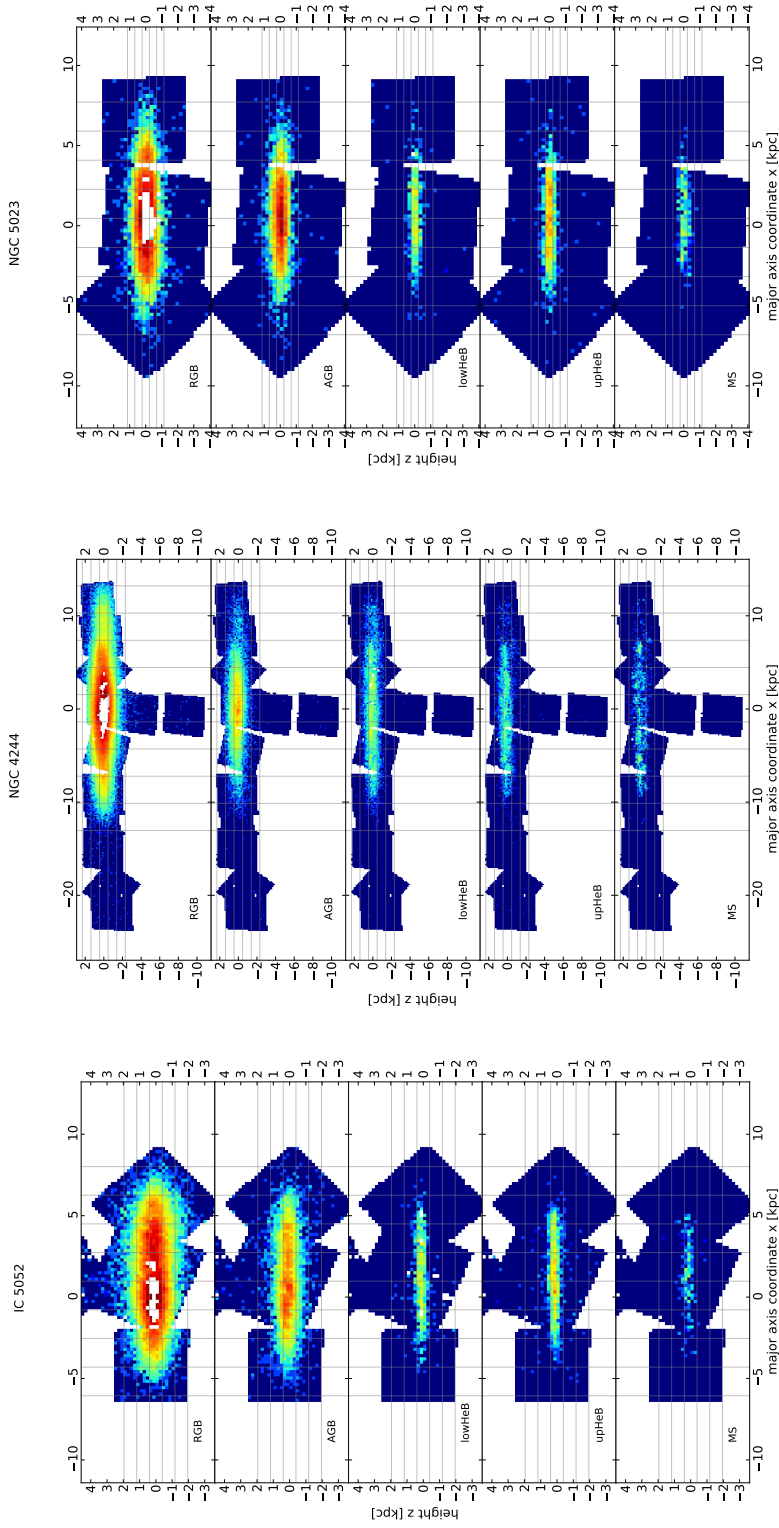
Figure 3.3.: Star count surface density maps (logarithmic scale) of stellar populations in three low mass edge-on galaxies: IC 5052, NGC 4244, NGC 5023 (left to right). Central white regions show the region that were masked due to our crowding limit. Vertical and horizontal gray lines are the bin edges for the extraction of the vertical and horizontal profiles in Figs. 3.4 and 3.7.
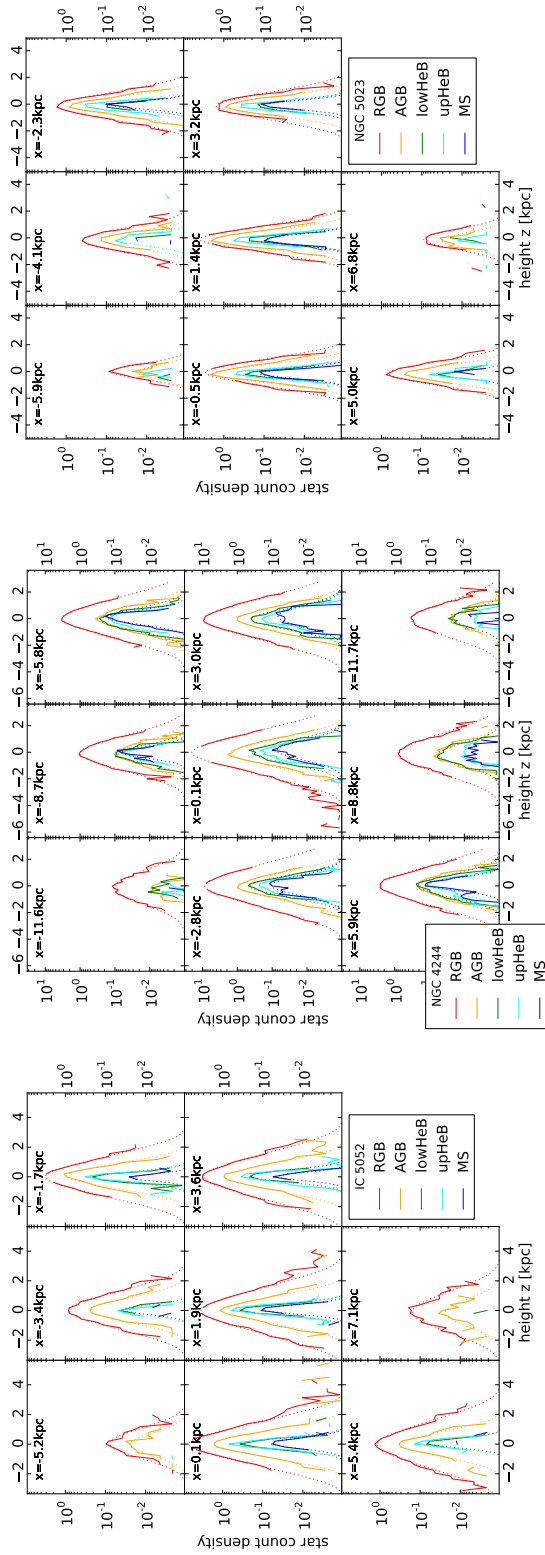
Figure 3.4.: Vertical density profiles of the five populations (red - RGB; yellow - AGB, green - lower HeB, cyan - upper HeB, blue - MS) at different radii in three low mass edge-on galaxies: IC 5052, NGC 4244, NGC 5023 (left to right). Solid lines are the data with uncertainties, dotted lines are the best sech^2 fits. The boundaries of the regions, where the profiles are extracted from, are shown in Fig. 3.3 as vertical gray lines.

Figure 3.5.: Change of the average scaleheight with stellar age. The blue dashed line show the results of fits of IC 5052 with an additional spheroidal component included. The dotted lines are power-law $z_0 \propto t^\beta$ fits to the data, excluding the youngest population, with the power-law indices β given given on the right.

populations (MS, upper HeB and lower HeB) have approximately the same scaleheight, this scaleheight is smaller than the AGB scaleheight, which is even smaller than the scaleheight of the RGB stars. The relative amount of this increase differs from galaxy to galaxy; in IC 5052 the scaleheight increases by 100% (from young to AGB) and 50% (from AGB to RGB), in NGC 5023 by 50% and 33%, in NGC 4244 by only 20% respectively from young to AGB and from AGB to RGB.

We have measured the scaleheights at different radial positions within the galaxies, as can also be seen in Figs. 3.4 and 3.6. Figure 3.6 nicely shows that for most populations the scaleheights change very little with radial position within each galaxy. While for the three young population, the scaleheight are constant along the disk, the older populations show a some mild flaring. We have quantified the strength of the flaring by fitting a straight line to the scaleheights as a function of projected radius. The slopes of these regression lines are given in Table 3.3.

The slopes the young populations (MS, upHeB and lowHeB) are are consistent with zero flaring. The intermediate and old populations in all three galaxies have very similar slopes of ≈ 10 parsec per kiloparsec, except for the RGB in IC 5052, which has almost 30 pc/kpc.

3.3.2. Radial Profiles and 2D Fits

We have also extracted the radial profiles from our data. The profiles at different heights from the midplane are plotted in Fig. 3.7. While the profiles do have some irregularities, they can in general be described as broken exponentials, with steeper
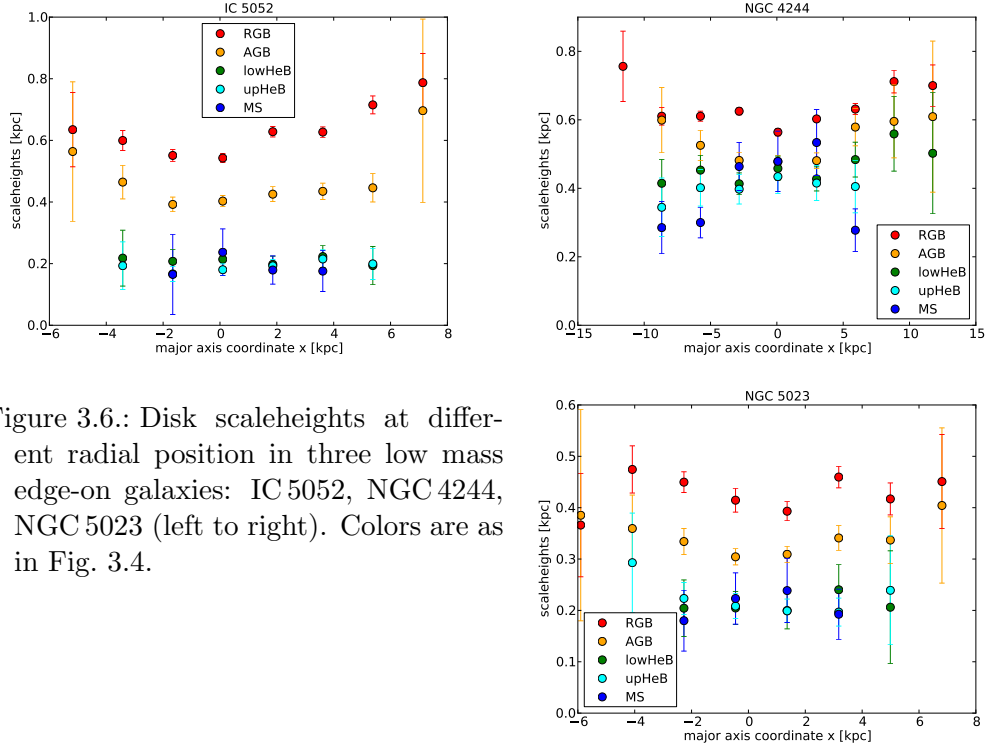
Figure 3.6.: Disk scaleheights at different radial position in three low mass edge-on galaxies: IC 5052, NGC 4244, NGC 5023 (left to right). Colors are as in Fig. 3.4.

Table 3.3.: Increase of scaleheights with projected radius.

galaxy	population	slope [pc/kpc]	rel. flaring [%]	R_{max} [kpc]
IC 5052	RGB	28±6	37±10	7.1
	AGB	11±4	19± 8	7.1
NGC 4244	RGB	9±3	19± 6	11.9
	AGB	11±3	27± 9	11.9
NGC 5023	RGB	9±7	14±12	6.8
	AGB	12±2	28± 5	6.8

Notes. This table gives the amount of flaring in the older populations of the three galaxies (younger populations do not flare). The column "slope" gives the absolute flaring dz_0/dR, the column "rel. flaring" the relative increase of scaleheight $(z_0(R_{max}) - z_0(R=0))/z_0(R=0)$ over the full observed range in radii, and the column R_{max} the maximum galactocentric radius, to which a scaleheight was measured.

slopes outside the break.

In two of the galaxies, NGC 4244 and NGC 5023, the scalelengths (inside the break) decrease with age, i.e. older populations are more centrally concentrated than younger populations. IC 5052 shows the opposite trend and the older popula-
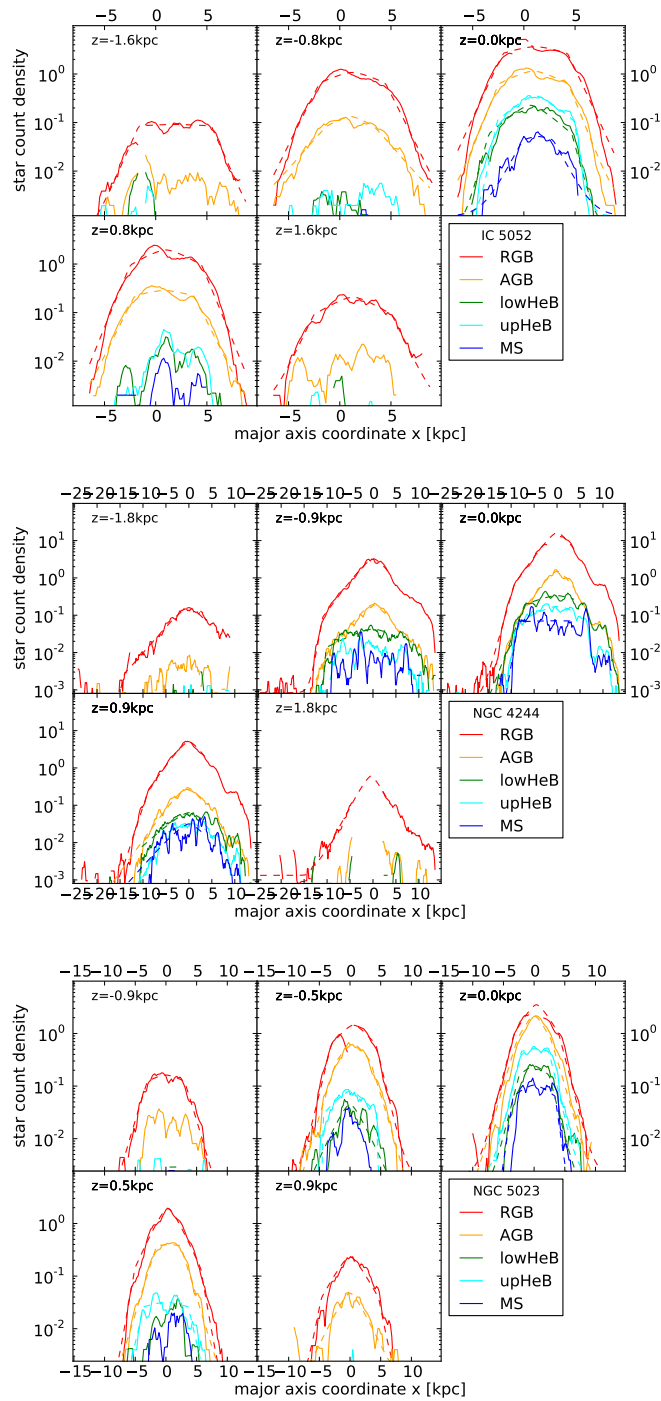
Figure 3.7.: Radial density profiles of the five populations at different heights above the plane in three low mass edge-on galaxies: IC 5052, NGC 4244, NGC 5023 (top to bottom). Solid lines are the data, dashed lines are the best fits.

Figure 3.8.: Disk scalelengths at differ-
ent position above/below the plane
in three low mass edge-on galaxies:
IC 5052, NGC 4244, NGC 5023 (left to
right). Colors are as in Fig. 3.4.

Figure 3.9.: Change of the average scalelength (inside the break) with stellar age.
The blue dashed line show the results of fits of IC 5052 with an additional
spheroidal component included.
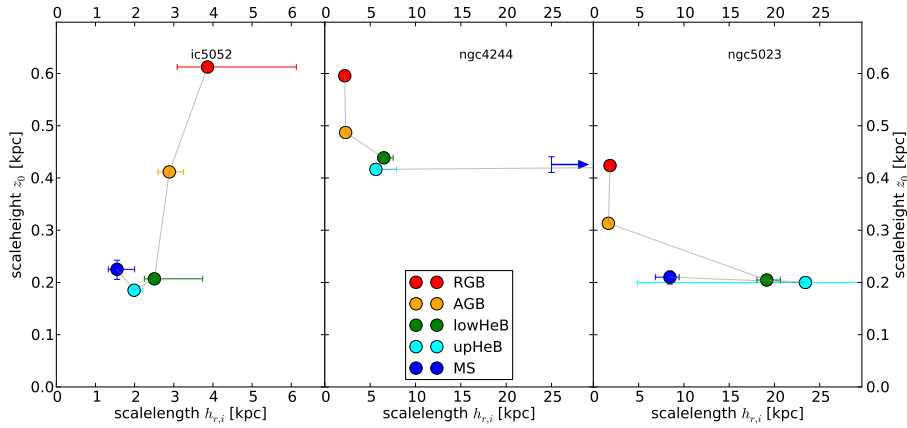
Figure 3.10.: Scaleheights vs. scalelengths (Note the different scales on the x-axes)
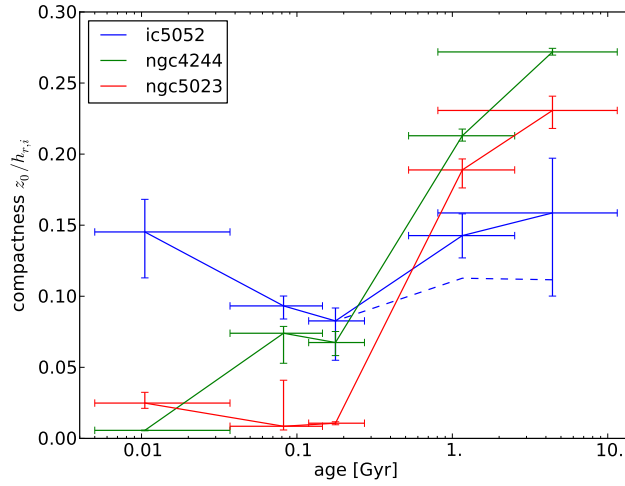
Figure 3.11.: Change of the compactness, i.e. the ratio of scaleheight to scalelength
with stellar age. The blue dashed line show the results of fits of IC 5052 with an
additional spheroidal component included.

tions have flatter profiles than the young populations (see Fig. 3.8 and Table 3.4).
Combining the results for scalelength and heights we get that younger populations
are in general thin and radially extended, while older populations are thicker and
radially more compact, as can be seen in Fig. 3.11. This is what is seen in the MW
for mono abundance populations, [e.g. Bovy et al., 2012b]

Breaks in Radial Profiles: The break radii for all populations within a galaxy
are approximately the same (within a kpc, see Fig. 3.12) and there is no trend with
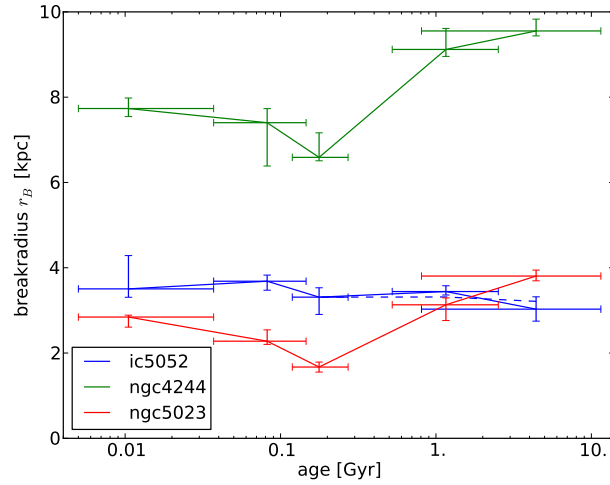
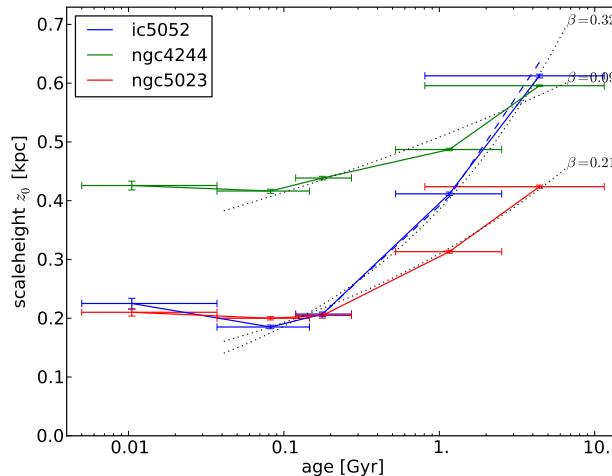Figure 3.12.: Change of the break radius with stellar age. The blue dashed line show the results of fits of IC 5052 with an additional spheroidal component included.

age.

Outside the break the younger populations have steeper profiles than older populations. This leads directly to a stronger break for younger populations; their profiles are rather flat inside the break and very steep outside, while for older populations the scalelength changes only little (by about a factor 2-3) across the break (see Fig. 3.14).

3.3.3. Discussion of observed profiles

3.3.3.1. Irregularities in the profiles:

IC 5052 appears to be lopsided. In Fig. 3.7 all disk fits for IC 5052 have the center about 1-2 kpc away from the literature value[9] of the galaxy's center, which is given as the zeropoint of the x-axis in the figure. The AGB and RGB profiles have their maximum actually near the literature value of the center, but the center of the fit is dominated by the central position between the breaks. In Fig. 3.15, the contours of young stars and RGB stars of IC 5052 can be seen on a R-band image [Meurer et al., 2006]. The innermost RGB contours coincide well with the brightest region of the R-band image and with the HyperLEDA position of IC 5052. In contrast the center of the outer RGB and the young star contours is further to the south east and coincide better with the dynamical center of the galaxy, taken from HI observation [Peters et al., 2013].

In the residuals images from our two-dimensional fitted models (see Fig B.2) the overdensity appears approximately circular. So we repeated the fits of the RGB

---

[9]from HyperLEDA, `http://leda.univ-lyon1.fr/`
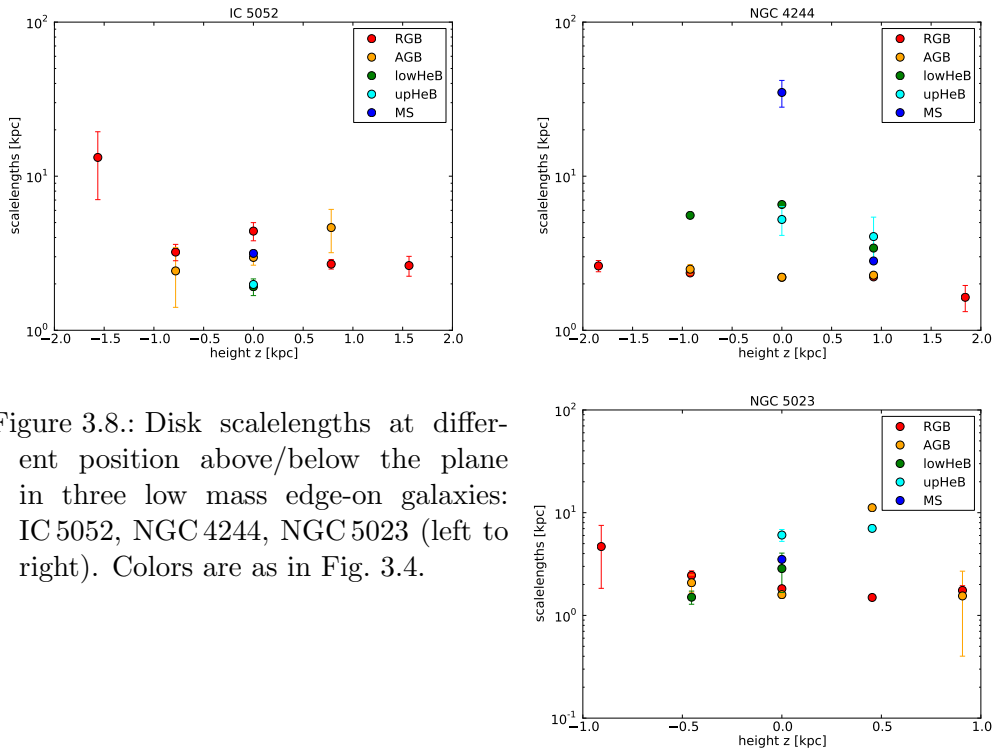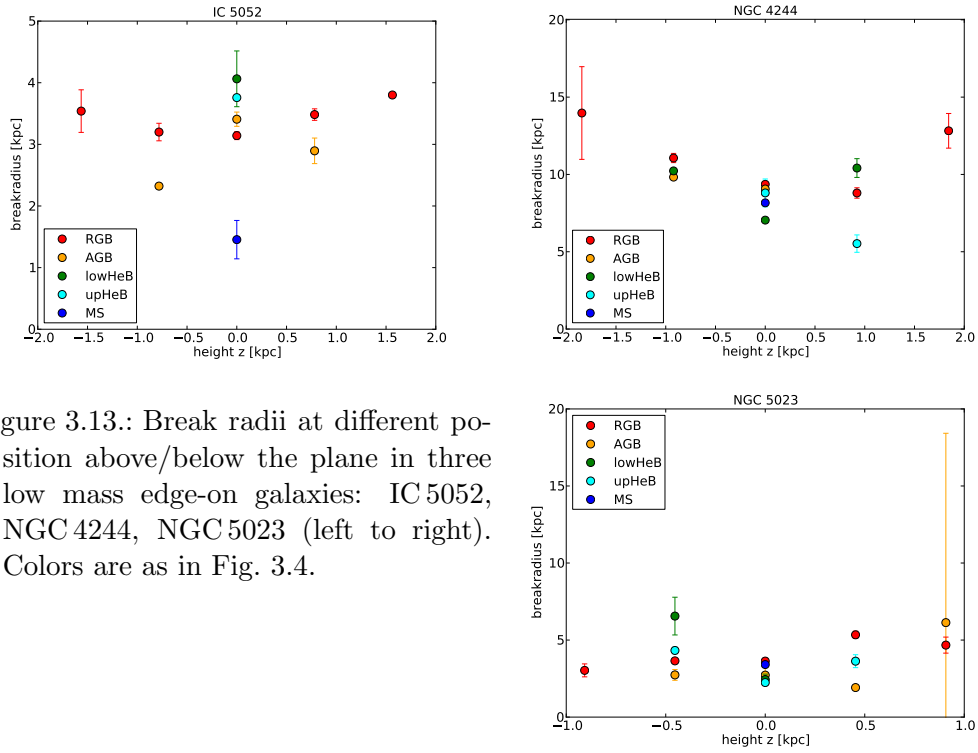
Figure 3.13.: Break radii at different position above/below the plane in three low mass edge-on galaxies: IC 5052, NGC 4244, NGC 5023 (left to right). Colors are as in Fig. 3.4.
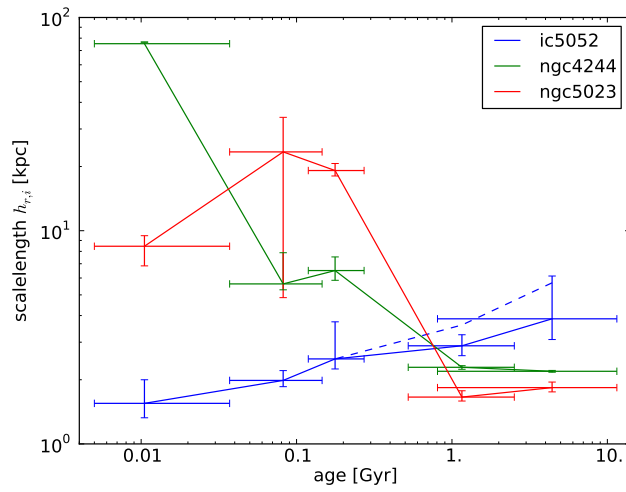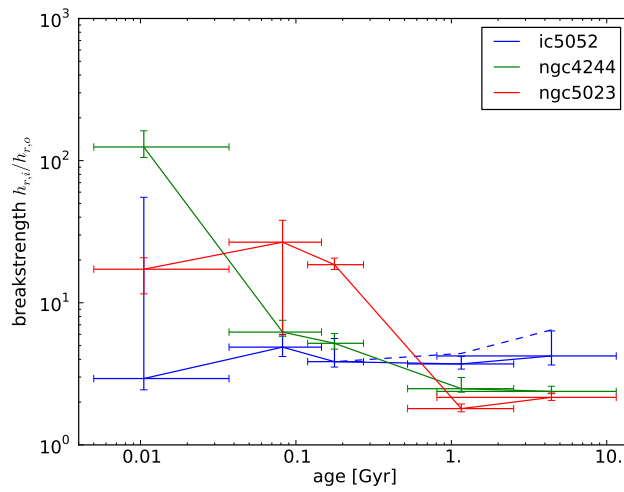

Figure 3.14.: Change of the break strength, i.e. the ratio of inner to outer scalelength with stellar age. The blue dashed line show the results of fits of IC 5052 with an additional spheroidal component included.

Table 3.4.: Scaleheights and scalelengths (inside the break) from the 2D fits of the different populations.

population	IC 5052		NGC 4244		NGC 5023	
	h_r	z_0	h_r	z_0	h_r	z_0
MS	$1.55^{+0.45}_{-0.22}$	$0.225^{+0.018}_{-0.019}$	$75.36^{+1.44}_{-1.19}$	$0.426^{+0.015}_{-0.015}$	$8.46^{+1.02}_{-1.62}$	$0.210^{+0.012}_{-0.013}$
upHeB	$1.99^{+0.22}_{-0.13}$	$0.185^{+0.007}_{-0.006}$	$5.63^{+2.25}_{-0.35}$	$0.416^{+0.006}_{-0.008}$	$23.42^{+10.60}_{-18.57}$	$0.200^{+0.006}_{-0.006}$
lowHeB	$2.50^{+1.23}_{-0.26}$	$0.207^{+0.007}_{-0.009}$	$6.50^{+1.03}_{-0.65}$	$0.439^{+0.006}_{-0.006}$	$19.15^{+1.51}_{-1.09}$	$0.205^{+0.008}_{-0.009}$
AGB	$2.89^{+0.37}_{-0.29}$	$0.412^{+0.006}_{-0.006}$	$2.29^{+0.04}_{-0.05}$	$0.487^{+0.004}_{-0.004}$	$1.66^{+0.12}_{-0.07}$	$0.313^{+0.005}_{-0.005}$
RGB	$3.86^{+2.27}_{-0.77}$	$0.612^{+0.006}_{-0.007}$	$2.19^{+0.02}_{-0.02}$	$0.596^{+0.003}_{-0.003}$	$1.84^{+0.11}_{-0.08}$	$0.424^{+0.005}_{-0.005}$
halo RGB	-	$2.30^{+0.69}_{-0.69}$	-	$3.0^{+2.1}_{-1.8}$	-	-
[3.6µm]	$2.145^{+0.018}_{-0.056}$	$0.433^{+0.037}_{-0.025}$	$1.845^{+0.077}_{-0.114}$	$0.468^{+0.043}_{-0.078}$	$1.248^{+0.038}_{-0.018}$	$0.301^{+0.043}_{-0.091}$
PAH [8µm]	$1.112^{+0.034}_{-0.067}$	$0.381^{+0.021}_{-0.036}$	$1.769^{+0.098}_{-0.171}$	$0.574^{+0.059}_{-0.068}$	$1.08^{+0.084}_{-0.056}$	$0.356^{+0.036}_{-0.076}$

Notes. All values in kpc.
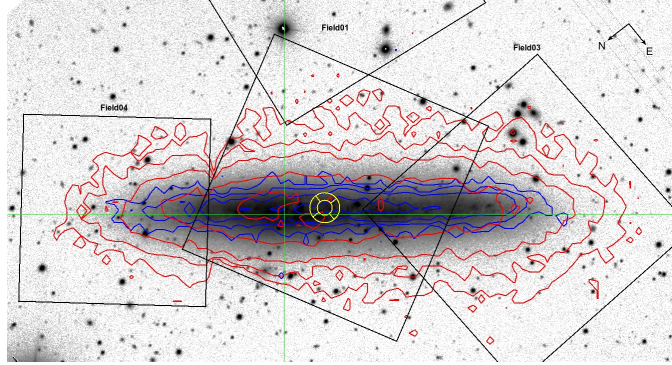
Figure 3.15.: R-band image of IC 5052 [Meurer et al., 2006]. The density of RGB stars is shown as red contours, the density of young stars as blue contours. The yellow reticle gives the dynamic center of the H I gas [Peters et al., 2013], the green cross the central position of the galaxy from HyperLEDA. The black boxes show the (approximate) coverage of our GHOSTS fields.

and AGB populations in IC 5052 with the overdensity described by an additional Sersic-component and evaluated the structural parameters of the disk again. While the scaleheights and the break radii of the two component fits are approximately the same as in the one component fit, the scalelengths are significantly larger. The results of the two component fits can be seen in Figs. 3.5, 3.9, 3.11, 3.12 and 3.14 as the dashed line.

NGC 4244 also has an asymmetric radial profile (see Fig. 3.7). At the north-eastern end of the disk, there is a break in all populations at about 9 kpc [see also de Jong et al., 2007]. On the south-western side there is break at about 7 kpc, followed by a plateau between 8 kpc and 12 kpc, where the profile again breaks. These structures cannot be modeled by our simple edge-on galaxy models and thus we only used the north-eastern part for our fit (up to $x < 4$ kpc).

3.3.3.2. Additional thick disk or halo component?

It is now widely accepted that galaxies contain multiple (disk) components. In contrast, as evident in Fig. 3.4, the vertical profiles of our low-mass galaxies could be fitted well by single disk models. This is remarkable, because more than three orders of magnitudes in surface density is covered between the central and the outermost parts of the galaxies; this corresponds to about eight magnitudes in surface brightness. This is significantly deeper than most of the integrated light observations that have been used to detect the thick disks.

However, the profiles presented so far were not optimized for low density regions. As written in Sect. 3.2.1, GHOSTS has two sets of culls for optimal star selection, one optimized for crowded regions, the other optimized for sparse regions. In previous sections we used the crowded field culls, to optimally sample the inner regions of the galactic disks. We will now use the sparse field culls, which are optimized for low density regions.

Additionally, the fine binning of the data we used before made it impossible to detect structures below a surface density of 0.019 arcsec^{-2} (which equals 1 star per bin). By using broader bins we can further extend the analysis to fainter regions. In the following we use the whole central region of each galaxy to create vertical profiles and look for additional structural components.

The result of this can be seen in Fig. 3.16. Compared to Fig. 3.4 we reach about one order of magnitude deeper now. A faint second component can now be detected in IC 5052 and NGC 4244. Since we are using star count data, this second component cannot be an effect of scattered light and extended PSFs, which might lead to similar detection in integrated light studies, if not modeled carefully [de Jong, 2008, Sandin, 2014]. We have fitted the whole profile with two sech^2 components. In both galaxies the second components are very faint, their central surface brightnesses are only 0.6% (IC 5052) and 0.08% (NGC 4244) of the main disk's central surface brightness. Due to their larger scaleheights ($z_{0,thick} = 2.30 \pm 0.69$ kpc for IC 5052 and $z_{0,thick} = 3.04 \pm 2.29$ kpc for NGC 4244), the second components dominate at $|z| > 2.2$ kpc and $|z| > 2.8$ kpc, respectively.

Note, that the choice of sech^2 for the fitting of the second component is a mere choice of convenience. It is not meant to imply that these components are really disk components. It is possible to fit these components equally well with other functions (e.g. exponential, Sersic, power law), but the sech^2 allows for the most direct comparison between the main disk and the second component. The possible nature of the second components will be discussed in Sect. 3.4.
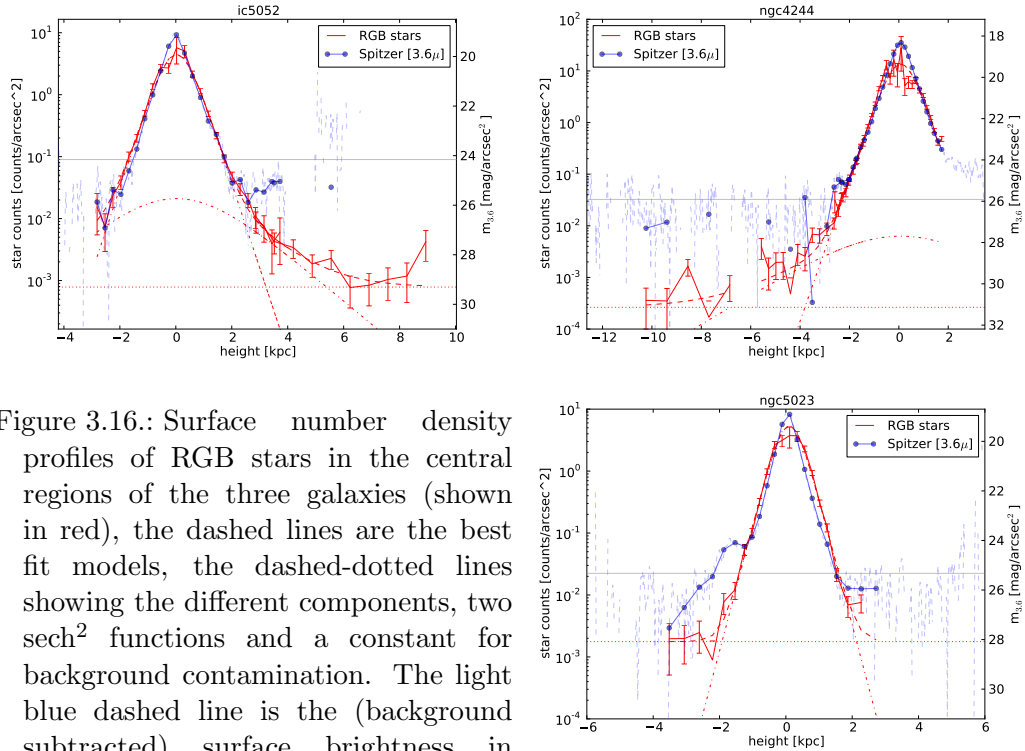
Figure 3.16.: Surface number density profiles of RGB stars in the central regions of the three galaxies (shown in red), the dashed lines are the best fit models, the dashed-dotted lines showing the different components, two $sech^2$ functions and a constant for background contamination. The light blue dashed line is the (background subtracted) surface brightness in Spitzers 3.6μm filter, the solid blue line the Spitzer data averaged to the same bin size as the star count data, the horizontal gray line is the estimated noise level of the background of the Spitzer data.

3.3.3.3. Comparison with Spitzer data

For all the galaxies in our sample we also have Spitzer imaging data in all four channels (Holwerda, priv. comm.). We use here the images from channel 1 (at 3.6μm) for comparison with the RGB count profiles. For the transformation from RGB counts to surface brightness we used the the same artificial CMDs as in Sect. 3.2.2 with a constant SFR and a flat MDF. By equating the number of RGB stars in the artificial CMDs with the expected flux of the underlying population, we calculated the counts-to-flux conversion factor. This factor can of course only be a rough estimate of the true conversion, because the exact transformation depends on the star formation history, which is unknown for the real galaxies. But as one can see in Fig. 3.16, where the Spitzer profiles are shown as light blue and the RGB counts as red lines, the transformation gives quite a good match between the profiles. At larger heights RGB stars are apparently the dominant contributor to the channel 1 light.

While the Spitzer and RGB profiles match well in a large part of their overlap regions there are two main differences:

First, the RGB profiles go much deeper than the Spitzer profiles. The Spitzer profiles are limited by a relatively bright background. To determine the sky brightness we measured the mean brightness of a large empty region far away from the galactic disk. The corresponding standard deviation in this region was used as an estimate for the noise and is shown as a horizontal gray line in Fig. 3.16.[10] Star counts are not affected by sky brightness, but they are limited by the number of contaminants, i.e. faint foreground stars and unresolved background galaxies. The density of these contaminants is so low, that our star counts can reach an equivalent surface brightness below $30\,[3.6\mu m]$-mag/arcsec^2.

Secondly, the Spitzer profiles have a sharper peak in the midplane regions than the star count profiles. The reason for this could be that the Spitzer data contains a mixture of all stellar populations, as well as dust and PAH emission [Meidt et al., 2012]. The younger populations, which have a much smaller scaleheight than the RGB stars (see Sect. 3.3.1), will add extra light to the central regions of the profile. It could also be that we miss some of the RGB stars in the central regions due to crowding effects or dust. While we do correct for a decreasing completeness with higher star count densities, we have not corrected for dust effects that will influence our optical data (where the star counts are done) more than the infrared Spitzer data.

In Table 3.4 the scaleheights and -lengths of the five populations and the Spitzer data are listed. The Spitzer scaleheight lies within the range of scaleheights of the resolved populations, supporting a interpretation as a combination of these different populations, but the Spitzer scalelengths (of NGC 4244 and NGC 5023) are shorter than those of any population, which precludes an interpretation of the Spitzer data as a simple combination of the stellar populations. From the two possible reasons for this mismatch, incompleteness and/or dust, we asses the former as unlikely. Through the extensive artificial star test we have a good estimate of the completeness and we have corrected for it. Furthermore, all regions with a completeness below 50% are excluded from the analysis, which leads to small uncertainties in the final star counts. On the other hand we do see signs of dust. Its effects are discussed in Sect. 3.4.1.

3.3.4. Summarizing results

Before we move on to the discussion, let us summarize all our results from this section: All three of the analyzed galaxies show the following trends in their structural parameters:

- The scaleheight of stellar populations increases with age, but only on timescales larger than about 300 Myr.

---

[10]The Spitzer images alos contain systematic deviations from a constant background level, e.g. large round areas of increased brightness in the image of NGC 5023. One of these bright spots lies near the center of NGC 5023 and can be seen in the vertical profile as the bump at $z \approx -2\,$kpc.

- The scaleheight of the young stellar populations is essentially constant along the disk, while AGB and RGB stars exhibit a mild flaring.

- The scalelength of stellar populations is essentially independent of the height above the plane.

- The break radius is independent of stellar population age.

Two out of three galaxies (NGC 4244 and NGC 5023) have similar trends in their radial profiles:

- The scalelength of stellar populations decreases with age.

- The break strength, i.e. the ratio of inner to outer scalelength, decreases with age.

A third galaxy (IC 5052) has an increasing scalelength with age, which leads to a constant break strength. This galaxy also has an additional overdensity of old stars, which lies off the center of the disk.

3.4. Discussion

3.4.1. The possible effects of extinction by gas and dust

In the previous section we have used a sech^2 profile for the vertical and a Bessel K$_1$ function for the radial profile of the star count surface density distribution of our galaxies. By doing this, we have implicitly assumed that the galaxies are transparent, i.e. that surface density is the result of the density integrated along the line of sight through the whole galaxy. The presence of dust will lead to a deviation from this idealized assumption.

The determination of the real distribution of dust in external galaxies is very difficult and beyond the scope of this paper; so we cannot correct for extinction effects directly, but we can model the effects of different dust distributions on star count maps of an idealized galaxy model.

We model the density of both the stars and the dust as exponential disks with a sech^2 distribution in the vertical direction. We calculate the "observed" surface brightness by solving the standard differential equation for the 1D radiative transfer along the line of sight:

$$\frac{dI}{dx} = -\kappa I + \epsilon, \tag{3.7}$$

with $\kappa \propto \rho_{dust}(x, y, z)$ and $\epsilon \propto \rho_{star}(x, y, z)$.

It could be questioned whether a radiative transfer equation is appropriate for treating star counts. But in fact, the effects of absorption are similar: It will attenuate and redden the light of a star until it falls below the detection limit of our observations (or out of our CMD selection boxes); and the higher the absorption,

the larger the fraction of stars that are removed from the CMD. Furthermore, star counts have the advantage that they are not affected by scattered or reflected light: the light of a star, that is absorbed, will not be re-emitted to become part of our star counts; thus the emissivity ϵ is proportional only to the local stellar density and has no scattered light term. The details of the effects of absorption on star counts do, of course, depend on the distribution of stars in the CMD, i.e. on the luminosity function and, thus, the star formation history. In this sense our approach is very simplified, but a full extinction modeling is beyond the scope of this paper.

We use three parameters for each, dust and stars, to model the 3D distribution: central density ρ_0, scaleheight z_0 and scalelength h_r. The density is then given by:

$$\rho(x, y, z) = \rho_0 \exp(-\sqrt{x^2 + y^2}/h_r)\mathrm{sech}^2(z/z_0) \qquad (3.8)$$

The parameters of the stellar disk are kept fixed, with $h_r = 1$ and $z_0 = 0.2$. The scales of the dust are varied to be either larger or smaller than the stellar ones. We have analyzed four models with all possible combinations of $h_r \in \{0.5, 2.\}$ and $z_0 \in \{0.1, 0.4\}$. The resulting vertical and radial profiles are shown in Fig. 3.17.

The qualitative effect of the dust on the vertical and radial profiles is similar: If the scaleheight (scalelength) of the dust is smaller than that of the stars, there is a dip in the vertical (radial) profile. If the scaleheight (scalelength) of the dust is larger than that of the stars, the vertical (radial) profile is flattened in the center, but no dip can be seen. The depth of the dip or the flattening depends on the dust mass [see also Seth et al., 2005b, for a similar analysis].[11]

We can compare the results of our simple dust models (Fig. 3.17) with the observed vertical profiles (Figs. 3.4, and also Figs. B.2 to B.4). The observed profiles have small dips only in the RGB profiles, while the profiles of the AGB and young stars still have peaks in the midplane. This suggests that the dust scaleheight is smaller then the RGB scaleheight, but larger than the AGB scaleheight. This is consistent with our measurements of the scaleheights of the PAH emission, which is near or above the AGB scaleheight (see Table 3.4).

Such large dust scaleheights agree well with the results of Seth et al. [2005b], who came to the same conclusion for a sample of low mass galaxies (including NGC 4244), and with the results of Dalcanton et al. [2004], who found the ISM of low mass galaxies ($V_{rot} < 120\,\mathrm{km/s}$) to be more diffuse and vertically extended than in massive galaxies.

The dust also affects the radial profiles and can lead to a dip or a flattening (see Fig. 3.17). In the data we do not see any central dip in our radial profiles (Fig. 3.4), but a flattening cannot be ruled out. Taking into account the smaller scalelength of the Spitzer $3.6\mu m$ data, it appears even very likely that the scalelength of the star count data is affected by dust. Thus, the true scalelength of the underlying populations might be smaller than given here.

---

[11]Note that all four dust models have the same central density. Therefore models with larger scaleheights/scalelengths have larger total dust masses.
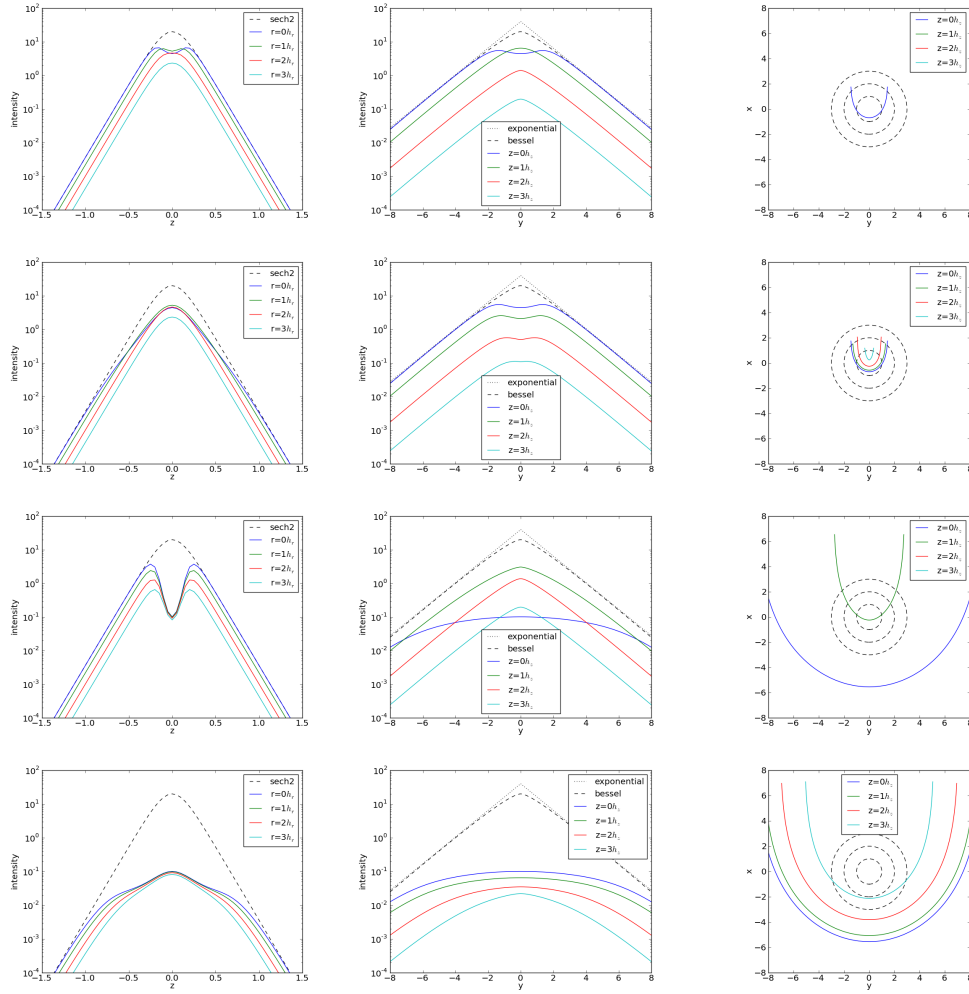
Figure 3.17.: Effects of dust on ideal galaxy models; Each row shows a model of different dust properties, from top to bottom they are defined by $(h_{z,dust}, h_{r,dust}) = (0.1,0.5)$ $(0.4,0.5)$, $(0.1,2.)$, $(0.4,2.)$. *left column:* vertical profiles at different radial positions (as given in the legend in terms of stellar scalelength); *middle column:* radial profile at different heights above the plane (see legend, given in stellar scaleheights); *right column:* face-on view of the position where the optical depth reaches one ($\tau = 1$), for different heights above the plane (see legend, given in stellar scaleheights); the dashed lines are circles of one, two and three scalelengths of the stellar component.

3.4.2. Direct comparison to other structural measurements in these galaxies

Star count measurements: Seth et al. [2005b] analyzed resolved stellar populations in the same three galaxies and divided them into three age groups (young, intermediate=AGB, old=RGB). At that time, they did not have enough data to study scalelengths or flaring, but they could measure scaleheights. Their results are given in Table 3.5; they are in agreement with our measurements.

In a series of papers Tikhonov and Galazutdinova studied the resolved stellar populations of a number of galaxies. In Tikhonov and Galazutdinova [2005] they analyzed, among other galaxies, NGC 4244. They used one central ACS field (which is in our field list Field01) and two WFPC2 fields. In agreement with our results they find an increasing thickness of the stellar populations from blue to AGB and RGB stars, but they do not quantify this. In one of the WFPC2 fields, they claim to detect the transition from a thick disk to a halo in form of a flattening of the vertical gradient of RGB star density at a height of z= 2.7 kpc. This is a similar height as we found for the transition to a weak halo in Sect. 3.3.3.2, but a detailed comparison is not possible, because their paper lacks a description of the selection of the stars, completeness correction and treatment of unresolved background galaxies.

Tikhonov et al. [2006] have analyzed the stellar populations of IC 5052 and NGC 5023. They also find an increase of thickness with increasing stellar age and a break in the vertical density gradient of RGB stars at z= 1.9 kpc and z= 1.6 kpc for IC 5052 and NGC 5023, respectively. While for IC 5052 this could be the same transition we found in Sect. 3.3.3.2, we do not see such a break in NGC 5023. A more detailed comparison is not possible due to the only rough description of their data and missing figures in their manuscript.

Infrared measurements: The galaxies are also in the S^4G survey [Sheth et al., 2010, Regan, 2013] who have also done structure decompositions [Salo et al., 2013]. They find somewhat larger scaleheights (IC 5052; 270/740 pc, NGC 4244 600 pc, NGC 5023 380 pc) than we did for the 3.6μm images, ranging near our RGB scaleheights.

IC 5052 is included in the sample of Comerón et al. [2011a], who use also S^4G data. They fit a thin (indexed with t) and a thick (indexed with T) disk with $z_{0,t} = 250$ pc and $z_{0,T} = 730$ pc in the outer part, and $z_{0,t} = 190$ pc and $z_{0,T} = 650$ pc in the inner part of the galaxy[12]; they obtain a ratio of column mass densities $\Sigma_T/\Sigma_t = 2.1$ in the outer part and $\Sigma_T/\Sigma_t = 2.5$ in the inner part. They state that their data is also compatible with a single disk structure.

NGC 4244 was separately analyzed in Comerón et al. [2011b]. They claim to detect a very subtle thick disk in NGC 4244, but only on one side of the galaxy, while on

---

[12]The original values in their paper are different (180 pc, 530 pc, 140 pc, 470 pc); we have converted them to our scale: While they use exponential scaleheights, we use sech^2, which differ by a factor of 2. Furthermore, Comerón et al. assumed a larger distance (8.1 Mpc). We have corrected for this.

Table 3.5.: Scaleheights from the literature.

	IC 5052	NGC 4244	NGC 5023	Ref.
counts z_0				
- young	0.26	0.33	0.20	1
- AGB	0.47	0.44	0.29	1
- RGB	0.66	0.55	0.39	1
NIR z_0	0.27/0.47	0.60	0.38	2
	0.25/0.73			3
	0.19/0.65			3
		0.60/0.74		4
optical z_0		0.58	0.46	5
dust z_0		0.6		6

Notes. All values in kpc. All scaleheights are scaled to our assumed distances.

References. (1) Seth et al. [2005b];(2) Salo et al. [2013]; (3) Comerón et al. [2011a]; (4) Comerón et al. [2011b]; (5) van der Kruit and Searle [1981a, 1982a]; (6) Holwerda et al. [2012]

the other side a single exponential is sufficient to describe the vertical profile. They get $h_z = 350\,\text{pc}$ on the northern side and $h_{z,t} = 300\,\text{pc}$ and $h_{z,T} = 370\,\text{pc}$ on the southern side, which corresponds to $z_0 = 700\,\text{pc}$ $z_{0,t} = 600\,\text{pc}$ and $z_{0,t} = 740\,\text{pc}$ for a sech^2 fit. This is significantly larger than our results. A possible reason for this discrepancy is the use of different fit function. While an exponential and a sech^2 do coincide for $z \gtrsim 4h_z = 2z_0$, they do differ for lower values. The fact, that both Comerón et al. and we fit also regions nearer to the plane, results in larger scaleheights for the exponential fit than for the sech^2 fit.

Visual measurements: van der Kruit and Searle [1981a, 1982a] have measured g-band[13] scaleheights as a function of position in NGC 4244 and NGC 5023. They find constant scaleheights along the plane with values of $z_0 = 0.58\,\text{kpc}$ for NGC 4244 and $z_0 = 0.46\,\text{kpc}$ for NGC 5023. This is in agreement with our RGB scaleheights.

3.4.3. Disk heating timescales and mechanisms

The heating of galaxy disks has mostly been studied in the Milky Way, mostly due to the lack of good age indicators in external galaxies. In the Milky Way the heating is usually examined through the age–velocity dispersion relation (AVR), which is

---

[13]The authors denote their band "J", but with an effective bandpass from 400 nm to 540 nm [van der Kruit, 1979] it lies between the B and V band and covers a wavelength range similar to the SDSS g-band.

equivalent to an age–scaleheight relation, because scaleheight h_z and vertical velocity dispersion σ_z are connected by

$$\sigma_z^2 = c\pi G \Sigma h_z, \tag{3.9}$$

where G is the gravitational constant, Σ the surface mass density and c a constant that depends on the form of the vertical mass profile[14].

Despite the fact that work on the AVR has been going on for decades, there is still no consensus on the form of the AVR. Some authors find a smooth power-law increase of the velocity dispersion with time [Wielen, 1977, Nordström et al., 2004, Koval' et al., 2009], while others find a flattening for stars older than a few Gyr [Carlberg et al., 1985, Soubiran et al., 2008], with a possible increase for very old stars ($> 9\,$Gyr) in the thick disk [Edvardsson et al., 1993, Quillen and Garnett, 2001, Anguiano et al., 2012, Anguiano, 2012]. Possible reasons for the discrepancies could be difficulties in age dating stars[15] or selection effects (dwarf stars vs. giants; including all stars vs. excluding moving groups and thick disk stars). But also the authors choice of model can influence their conclusions. For example, Seabroke and Gilmore [2007] showed that, though the data of Nordström et al. [2004] is indeed consistent with a power-law increase of σ_z, it also cannot reject a saturation of σ_z at ages older than $4.5\,$Gyr.

As possible mechanisms for heating the disk, scattering by giant molecular clouds (GMC) were the first to be proposed by Spitzer and Schwarzschild [1951], followed by spiral structure [Barbanis and Woltjer, 1967] and massive compact halo objects [MACHOS, e.g. black holes Lacey and Ostriker, 1985]. None of these alone were found to be supported by the observations [see e.g. Binney and Tremaine, 2008, and references therein]. Other proposed mechanism include minor mergers [Toth and Ostriker, 1992], which can lead to a sudden increase of velocity dispersion, when the satellite is relatively massive [Quinn et al., 1993], or to a smooth heating, when many small galaxies are accreted over a long time span [Velazquez and White, 1999], resonances from the bar [Kalnajs, 1991] and dissipating star clusters [Kroupa, 2002]. Another idea is that the increase of scaleheight and velocity dispersion is not due to a heating of a thin disk, but that it reflects the decreasing thickness of the gas disk, that slowly settles from a turbulent phase at high redshift to a more ordered rotation later on [Kassin et al., 2012, Bird et al., 2013].[16] Note that the two most accepted models, namely scattering by GMC and spiral arms would lead to a saturation. This is especially comprehensible for the vertical motion σ_z, since GMC and spiral arms act on stars in the very midplane of the disk and any star with a large vertical velocity will spend most of its orbital time far away from the plane. Thus, it would not be affected by GMCs or spiral arms any more.

---

[14]e.g. for a sech^2 it is c=2 and for an exponential c=3/2.

[15]For example, an age uncertainty of only 30% for the oldest stars, which is much lower than the uncertainties in current data, can erase a sharp increase in velocity dispersion at $9\,$Gyr [Martig et al., 2014a]

[16]We will still use the term "heating" for the increase of scaleheight or velocity dispersion with age. This does not reflect a preference for some of the models, but it is chosen merely for convenience.

Our data do not have the necessary age resolution to answer the question of a possible saturation of the heating, but we can constrain heating efficiencies. We have fitted a power law $z_0 \propto t^\beta$ to our data (see Fig. 3.5, excluding the data point of the youngest stars) and find indices β in the range 0.09-0.32. According to Equation 3.9 this corresponds to a power law for the velocity dispersion $\sigma_z \propto t^\alpha$ with $\alpha = \beta/2$. This is significantly lower than the Milky Way value $\alpha_{\mathrm{MW}} > 0.3$ [e.g. Hänninen and Flynn, 2002, Nordström et al., 2004][17], but consistent with the values for low mass galaxies found by Seth et al. [2005b]. A probable explanation for the lower disk heating in low mass galaxy is that the two main heating mechanisms, scattering by GMCs and by spiral structure, are less efficient, because low mass galaxy are gravitational more stable, i.e. have less spiral structure, and a more extended, but less dense interstellar medium, i.e. fewer GMCs [Dalcanton et al., 2004].

3.4.4. Structural evolution of stellar populations

Martig et al. [2014a,b] have analyzed seven simulations of disk galaxies representing a variety of merger histories. They have sliced each galaxy in so called "mono-age populations", each representing an age range of $500\,\mathrm{Myr}$, and analyzed how their structural parameters (scalelength and -height, velocity dispersion) change as a function of age (at z=0).

In galaxies with a quiescent merger history they find a smooth decrease of scalelength with age, and a smooth increase of scaleheight (and vertical velocity dispersion). Only for very old star (age$> 8.5\,\mathrm{Gyr}$), a jump in vertical velocity dispersion can be seen. These very old stars are centrally more concentrated and show strong flaring; they are more likely associated with a bulge or inner halo component. The physical reason for the smooth evolution of scalelengths is seen in radial migration. Stars are born in an irregular, but relatively flat profile with a break. With time stars migrate and populate the outer disk, thus erasing the break. At the same time the central parts contract (due to conservation of angular momentum), which leads to a steepening of the radial profile. The vertical heating in their simulation is caused by spiral arms, overdensities in the disk, the bar and bending waves, but not by radial migration.

As expected, mergers have a significant effect on the evolution of scaleheight: A merger leads to a sharp increase in the AVR by increasing the velocity dispersion/ scaleheights of all populations born before the merger. But it also has an interesting effect on the scalelength evolution: Near the time of a merger the normal trend of scalelengths with age is reversed. For a certain age range (usually about $2\,\mathrm{Gyr}$) the scalelength increases with age. This leads to V-shaped structures in a scalelength vs. age plot. During this period, scaleheight and scalelength are correlated.

The increase (decrease) of scaleheight (scalelength) with age and the corresponding anti-correlation in a h_z–h_r plot, that Martig et al. see in quiescent galaxies, is

---

[17]There is no clear consensus on the value of α for the MW, but almost all authors find values in the range $0.3 < \alpha < 0.6$, with the exception of Anguiano [2012], who find $\alpha = 0.12$ for the MW thin disk.

very similar to what we see in NGC 4244 and NGC 5023 (see Fig. 3.10).

The exceptional behavior of IC 5052 can also be explained in the light of the results of Martig et al., if we assume that IC 5052 had a merger recently. This assumption is strongly supported by the irregular radial profile of IC 5052 (see Sect. 3.3.3.1); the overdensity of old stars, that is found with an offset from the dynamical center of the galaxy, could be the remnant of a merging satellite. Furthermore the residual map from the fit (Fig. B.2) reveals a stream like feature, that connects the overdensity on the north-western side of the disk with a smaller overdensity at the south-eastern side. Martig et al. [2014a] have also shown that a merger will lead to a strong flaring of the pre-existing disk. That fits well the fact that the old population of IC 5052 has the strongest hints on flaring (see Table 3.3) and the highest heating efficiency (see Fig. 3.5) of all our galaxies.

Bird et al. [2013] have analyzed a high-resolution cosmological simulation of a Milky-Way-mass galaxy. They also dissect their simulated galaxy into different age groups and find an increasing scaleheight and a decreasing scalelength with age. These trends are similar to Martig et al. [2014a,b] and our observations, but in contrast to Martig et al. [2014a,b] these trends are imprinted on the populations during their formation and change only little during the evolution of the galaxy. In their model the age evolution of the structural parameters is a direct consequence of the time evolution of the properties of the gas from which the stars are formed. While the gas at high redshift has a large vertical extent and is mainly dispersion supported, it gets thinner and radially more extended with time; and the stars follow this behavior.

There is another feature in the galaxy of Bird et al. [2013], that we can compare our observations with. Their galaxy has a strong flaring in all age groups and velocity dispersion profiles that are almost constant with radius for each age group. This is in strong disagreement with our observations, and with integrated light [van der Kruit and Searle, 1981a,b, 1982a,b, Shaw and Gilmore, 1990, de Grijs and van der Kruit, 1996][18] and kinematical observations [van der Kruit and Freeman, 1984, 1986, Bottema, 1993, Martinsson et al., 2013], which all find constant scaleheights and exponentially decreasing velocity dispersions. Note that the strong flaring of Bird et al. [2013] is not a consequence of the evolution or interactions, but it is also already imprinted in the gas at all times.

Stinson et al. [2013] compare a cosmological simulation of a Milky Way-like galaxy including detailed chemical modeling with the results of Bovy et al. [2012b]. They also dissect their model galaxy into mono-abundance populations and find a anti-correlation between scaleheight and scalelength. They show that the mono-abundance populations are good approximations of mono-age populations (usually

---

[18]Note, that some galaxies in these papers do show a hint of an increase of scaleheight at the very edges of the disks. See also de Grijs and Peletier [1997] for a sample of flaring galaxies.

with 1σ age spreads of less than 1 Gyr) and that the anti-correlation is indeed caused by an increase of scaleheight and a decrease of scalelength with age. This is therefore in full agreement with our observations of NGC 4244 and NGC 5023. Stinson et al. [2013] have neither looked at the radial variations of scaleheights nor at the physical origins of these relations.

3.4.5. Thin and thick disk dichotomy?

Studies of the age evolution of galactic disks beyond the MW (or even the Local Group), similar to the theoretical work in Sect. 3.4.4 were very difficult until recently and only a few authors have tried it [e.g. Seth et al., 2005b, Tikhonov and Galazutdinova, 2012b,a]. Thus, most observational data on disk evolution comes form thin and thick disk decompositions[19].

Thick disks are usually found to be thicker by a factor of at least $z_T/z_t > 1.6$ [Yoachim and Dalcanton, 2006], in most cases it is even $z_T/z_t > 2.6$ [Comerón et al., 2011a, Pohlen et al., 2004, and references therein]. The scalelengths of the thick components are, with only a few exceptions, also larger than those of the thin disk [Pohlen et al., 2004, Yoachim and Dalcanton, 2006, Comerón et al., 2011a]. On average, no flaring was found, neither in the thin nor the thick disk [Comerón et al., 2011a].

So, how do would our disks fit into these samples? Are our old disks comparable to thick disks?

Figure 3.18 shows the scaleheights compared to thin and thick disk scaleheights by Comerón et al. [2011a] and Yoachim and Dalcanton [2006]. While all our measured disk scaleheights are consistent with thin disk scaleheights, the scaleheights of the faint extended components in IC 5053 and NGC 4244 are larger than typical thick disk scaleheights.

We found old-to-young scaleheight ratios of about 3, 1.5, and 2 (for IC 5052, NGC 4244 and NGC 5023, respectively). While for IC 5052 and NGC 5023 this agrees well with earlier thick disk studies, it would make the disk of NGC 4244 the "thinnest" thick disk (relative to the thin disk) seen so far. Those thickness ratios are also in good agreement with the velocity dispersion measurement within the thin disk of the Milky Way (see Sect. 3.4.3): The velocity dispersion of stars increases from less than 10 km/s at an age of 1 Gyr to more than 20 km/s at ages of about 6 Gyr. According to Equation 3.9, such a doubling of velocity dispersion would result in an increase of scaleheight by a factor of four, which is already more than we observe. Furthermore, in two of three galaxies (namely NGC 4244 and NGC 5023) the old and thicker component has a much shorter scalelength than the young populations, in contrast to earlier thick disk observations in external galaxies.

Therefore, we conclude that the old disks observed here are really the old thin disks of those galaxies. More extended components are much fainter and cannot contain more than 1% of the stellar mass (see Sect. 3.3.3.2).

---

[19]or from color gradients, but degeneracies between age, metallicity and extinction effects make an interpretation of these gradients ambiguous.
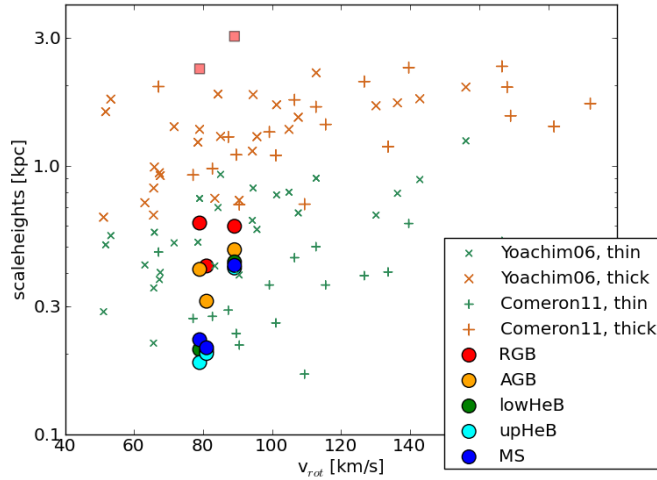
Figure 3.18.: Comparison of our measured scaleheights with data from Yoachim and Dalcanton [2006] and Comerón et al. [2011a]. The colored circles show our results for the different populations (color code as before); squares show the faint extended component (Sect. 3.3.3.2).

3.4.6. Breaks

In each galaxy we find the break radius to be the same for all populations. The breaks are sharper, i.e. the ratio $h_{r,i}/h_{r,o}$ is larger, for younger populations. This is in agreement with earlier observations by de Jong et al. [2007] and Radburn-Smith et al. [2012]. The conclusion that a constant break radius favors a dynamical origin of the break [de Jong et al., 2007] was already questioned by Roškar et al. [2008]. In their simulation, the break is caused by a decrease in the gas density and the break radius is moving outward with time while gas with higher angular momentum is accreted. Despite this change of break radius with time, at the end of the simulation the break radius is the same for populations of all ages. This is due to the radial migration of stars: The oldest stars, that have the most time to migrate, move furthest outwards, shifting their break to larger radii and weakening its strength.

A similar behavior is seen in the test particle simulations of Elmegreen and Struck [2013]. They start with a flat radial density profile of stars with a sharp cutoff at a given radius. This initial disk is perturbed by transient mass clumps in the disk, which leads to a double exponential profile with decreasing break strength, until at the end, after a couple of Gyr, the break has been erased and a single exponential has formed. During this process the break radius is also moving outwards.[20]

---

[20]The authors actually state that the break radius of the double exponential profile is comparable to the initial cutoff, but a detailed look at their Fig. 2 shows an increase of break radius with time.

Our findings are in contrast with Bakos et al. [2008], who argued that the break is only a change of stellar populations, but not a change in the mass density profile. While we also see a change in stellar populations, namely a change in the ratio of young to old stars, that has a maximum near the break, it is also clear from the existence of the break in all populations, that the mass profile is also broken.

3.5. Conclusions and Summary

In this paper we have mapped the stellar populations of three low mass, edge-on disk galaxies: IC 5052, NGC 4244 and NGC 5023. Through the analysis of their CMDs we could dissect the stellar content of the galaxies in five population of distinct ages. We have measured the structural parameters (scaleheights, inner and outer scalelengths, break radii, flaring) for each population and analyzed their dependence on stellar age.

Each component of each galaxy can be well fitted with a single disk model with constant scaleheight and a broken exponential radial profile. None of the populations shows a need for second (e.g. thick) disk component. Along the minor axes of IC 5052 and NGC 4244 we have detected very faint additional components in the old population, which contain at most 1% of the main disks mass and are thus much fainter than a typical thick disk. These extended components are probably the faint halos of their galaxies.

We have estimated the amount of flaring in all the populations. While the younger populations do not flare, the intermediate and old populations show a small increase of scaleheight by about 10 pc per kpc in radius. This adds up to a relative flaring of not more than 30% over the whole observed radial range, which reaches well beyond the break in the radial profiles. While such a low amount of flaring is consistent with most earlier observations, it poses severe constraints on simulations, where usually a stronger flaring is found due to interactions and merging processes.

All galaxies have an increase of scaleheight with age, but the disk heating efficiency, expressed through the index α in the power law of the form $\sigma_z \propto \sqrt{z_0} \propto t^\alpha$ is lower than in the Milky Way. This can be well understood through the weaker spiral structure (i.e. larger gravitational stability) and more diffuse interstellar medium of low mass galaxy disks.

The break in the radial profiles appear at the same radius for all ages in each galaxy. In two of the galaxies (NGC 4244 and NGC 5023), the break strength decreases with age, which supports break formation models that induce a sharp cutoff of star formation (either through star formation thresholds or limited gas supply), that are then softened by scattering and migration of stars over time.

In IC 5052 we detect an additional overdensity of old stars, which lies off the center of the disk, and a stream like feature in the residuals of the fit. These are interpreted as indication of a recent merger. The effects of this merger can be seen in the increasing scalelength with age, the larger amount of flaring and the higher heating efficiency in IC 5052 compared to the other two galaxies.

4. The age-resolved disk structure of nearby massive galaxies

4.1. Introduction

In the previous chapter we have demonstrated the capabilities of resolved stellar populations for the analysis of galactic disks. In this chapter we will expand this analysis to three, more massive galaxies, that have maximum rotational velocities similar to the Milky Way. These massive galaxies are more complex than the low mass ones. They show clear dust lanes, they have prominent bulge and halo components, and they are more strongly affected by crowding issues due to their higher star count densities.

This chapter is organized as follows: In section 4.2 we describe the changes and additions in our method compared to the chapter 3, in section 4.3 we present the results for the massive galaxies, followed by their discussion in section 4.4 and the conclusions in section 4.5.

4.2. Data and Methods

For the analysis of the massive galaxies we use the same methods as for the low mass galaxies in Chapter 3; data and methods are described in Section 3.2. Here we only describe changes and additions that are specific to the analysis of the massive galaxies.

4.2.1. Age Selection in the CMD

For the massive galaxies we define a new age group, called "allyoung", that was not introduced for the low mass galaxies in Section 3.2.2 and that replaces the three populations MS, upHeB and lowHeB. The reason for this is that most young stars in the massive galaxies are in regions of high crowding and large dust densities, where we cannot detect them. Therefore the number of young stars that we can detect is often too low for a structural analysis. Especially the MS and upHeB populations do not contain enough stars. By combining the three young populations into a single population, we increase the number of stars and the signal-to-noise of the data.

That is why we define a larger selection box that encompasses the MS, upHeB and lowHeB boxes. The selection box and the age distribution of stars in this box can be seen in Fig. 4.1 and its main parameters in Table 4.1.
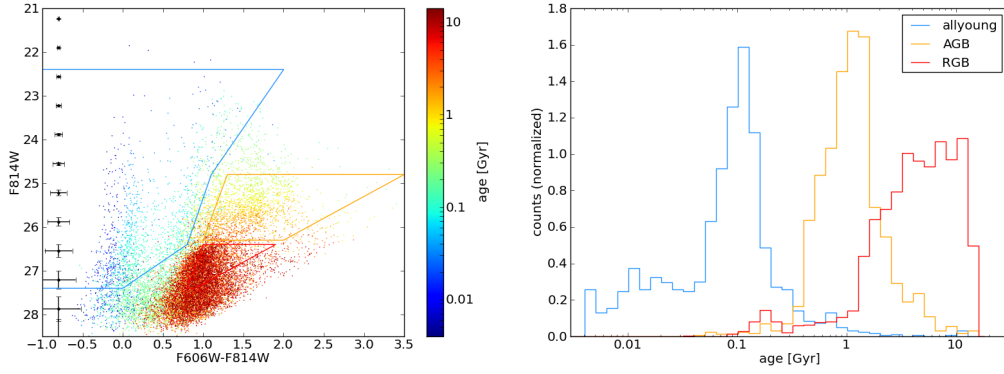
Figure 4.1.: *left*: An artificial CMD generated with a constant star formation rate and a flat metallicity distribution function ($-2.2 < [Z] < 0.2$). The colored boxes are the population boxes as described in the text. Stars are colored according to their age (see color-bar). The errorbars denote typical photometric uncertainties determined from artificial star tests. *right*: The age distribution of stars in the three population boxes in the left figure.

Table 4.1.: Properties of the age distribution of the defined stellar populations, derived from models assuming a constant SFR and a flat metallicity distribution.

	allyoung	AGB	RGB
mean(age) [Gyr]	0.15	1.36	5.07
std(age) [Gyr]	0.39	0.94	3.96
median(age) [Gyr]	0.12	1.15	4.41
10-percentile	0.011	0.49	1.36
90-percentile	0.25	2.50	11.2

4.2.2. Creating Stellar Density Maps

We use here the same method for creating stellar density maps as in Section 3.2.3. We create 2D-histograms of the star counts of each population, and correct them for incompleteness and masked regions. The bin size is again $(7.2'')^2$ and bins with a completeness below 50% are masked out.

Additionally we mask out regions that are heavily affected by dust. We use the nonstellar $8\,\mu$m images, which we obtained from the Spitzer data (see Section 3.2.5), to create dust masks. While polycyclic aromatic hydrocarbonates (PAH), which dominate the emission in Spitzer's $8\,\mu$m band, make up for only a small fraction of the total ISM, their emission correlates well with the emission of cold dust at longer wavelengths [Haas et al., 2002, Bendo et al., 2008, Calapa et al., 2014, Jones et al., 2015]. Thus we can use the $8\,\mu$m images to identify the regions that are most strongly affected by dust and extinction.

We mask out regions that have a nonstellar $8\,\mu$m emission of more than $1\,\mathrm{MJy/sr}^2$.[1] The dusk masks are shown in Fig. 4.2 as black contours.

4.2.3. Fitting Methods

In contrast to the low mass galaxies, where a single disk per population gives an acceptable fit to the data, the massive galaxies are clearly composed of more than one component. We use a combination of a broken edge-on disk and a Sérsic component for the description of each component. So the total model reads

$$n(x, z) = n_{bg} + n_{\mathrm{D}}(x, z) + n_{\mathrm{S}}(r), \qquad (4.1)$$

where n_{bg} is the surface density of contaminants and the model of the disk is given by

$$n_{\mathrm{D}}(x, z) = n_0 \mathrm{sech}^2 \left(\frac{z - z_c}{z_0} \right) n(x) \qquad (4.2)$$

with

$$n(x) = |x - x_c| \begin{cases} \mathrm{K}_1 \left(\frac{|x - x_c|}{h_{r,i}} \right) & \text{for } |x - x_c| < r_b \\ \frac{\mathrm{K}_1(r_b/h_{r,i})}{\mathrm{K}_1(r_b/h_{r,o})} \mathrm{K}_1 \left(\frac{|x - x_c|}{h_{r,o}} \right) & \text{for } |x - x_c| > r_b. \end{cases} \qquad (4.3)$$

The free parameter of the disk are its central coordinates x_c and z_c, the central density n_0, the inner and outer scalelength $h_{r,i}$ and $h_{r,o}$, the breakradius r_b and the scaleheight z_0. The Sérsic component is defined by

$$n_{\mathrm{S}}(r) = n_{\mathrm{eff}} \exp \left\{ -b_m \left[\left(\frac{r}{r_{\mathrm{eff}}} \right)^{1/m} - 1 \right] \right\} \qquad (4.4)$$

with

$$r = \sqrt{(x - x_c)^2 + \frac{(z - z_c)^2}{(1 - \epsilon)^2}}. \qquad (4.5)$$

The free parameters here are the effective radius r_{eff}, surface density at the effective radius n_{eff}, the Sérsic index m and the ellipticity ϵ. Using this model, we implicitly assume, that the central coordinates and the position angle of disk and spheroidal component are the same. Thus, the model has in total 11 free parameters.

The restriction to only two components is a priori not obvious, and it could be argued for more (e.g. thin and thick disk, bulge and halo), but we show in the following sections, that these two component give already acceptable fits and there is no need to introduce more components.

---

[1]except for NGC 891, where we raised this limit to $5\,\mathrm{MJy/sr}^2$, because the emission in NGC 891 is so bright, that the extended wings of the PSF of Spitzer's channel 4 raise the flux density in large parts of the image to values above $1\,\mathrm{MJy/sr}^2$.

When fitting our model to the Spitzer data, we convolve the model with the Point Spread Function (PSF) of the respective channel of the Spitzer telescope. Since the Spitzer PSFs are defined within a radius of $2.6'$, we restrict the Spitzer fits to a region within $|z| = \pm 2.6'$ in each galaxy. Note that with the truncated PSF we still underestimate the amount of scattered light, because the galaxies are radially more extended than $2.6'$. This means that we cannot account for light that is scattered from the other side of the galaxy; for this, a PSF with a diameter twice that of the galaxy would be needed. Unfortunately, such an extended PSF is not available. For star count data, no PSF convolution is needed.

4.3. Results

4.3.1. Two-dimensional fits

4.3.1.1. NGC 891

NGC 891 is an Sb galaxy of approximately the same mass as the Milky Way ($V_{rot} = 212\,\text{km/s}$). The star count maps (Fig. 4.2) show a clear disk in each population and an additional bulge/halo component for the RGB and AGB population. Its radial profile (right panel of Fig. 4.3) can be divided into the following regions:

$|x| < 5\,\text{kpc:}$ Bulge dominated region

$5\,\text{kpc} < |x| < 13\,\text{kpc:}$ Inner disk region; There is a disk break at $\approx 12\,\text{kpc}$.

$13\,\text{kpc} < |x| < 19\,\text{kpc:}$ Outer disk region

$19\,\text{kpc} < |x|:$ Halo region

The two-dimensional fits are done with two components, disk plus bulge, for the RGB and AGB populations. The residual maps do not show any large structures, that would hint to a third component (e.g. a thick disk or a separate halo). That means that a single Sérsic component can well fit the bulge in the central region and the halo beyond the end of the disk (out to $30\,\text{kpc}$); but note that the inner bulge is completely masked out due to crowding effects. This results in the situation that we actually measure the bulge only outside its effective radius. For the population of young stars we also use a two-component model consisting of an edge-on disk and a Sérsic spheroid. The Sérsic component is very weak, and it is consistent with being caused by the scattering of old stars into the "allyoung" selection box due to photometric errors. Using the model CMDs from Sec. 4.2.1 we estimate that, for a population of stars older than $1\,\text{Gyr}$, the ratio of allyoung-to-RGB stars is about 0.5% and for an population older than $0.5\,\text{Gyr}$ the ratio is 1.6%, while the measured ratio in the Sérsic component is 0.7%. Omitting this Sérsic component in the fit would result in a much larger scaleheight of the disk, which clearly fails to describe the outer parts of the disk.
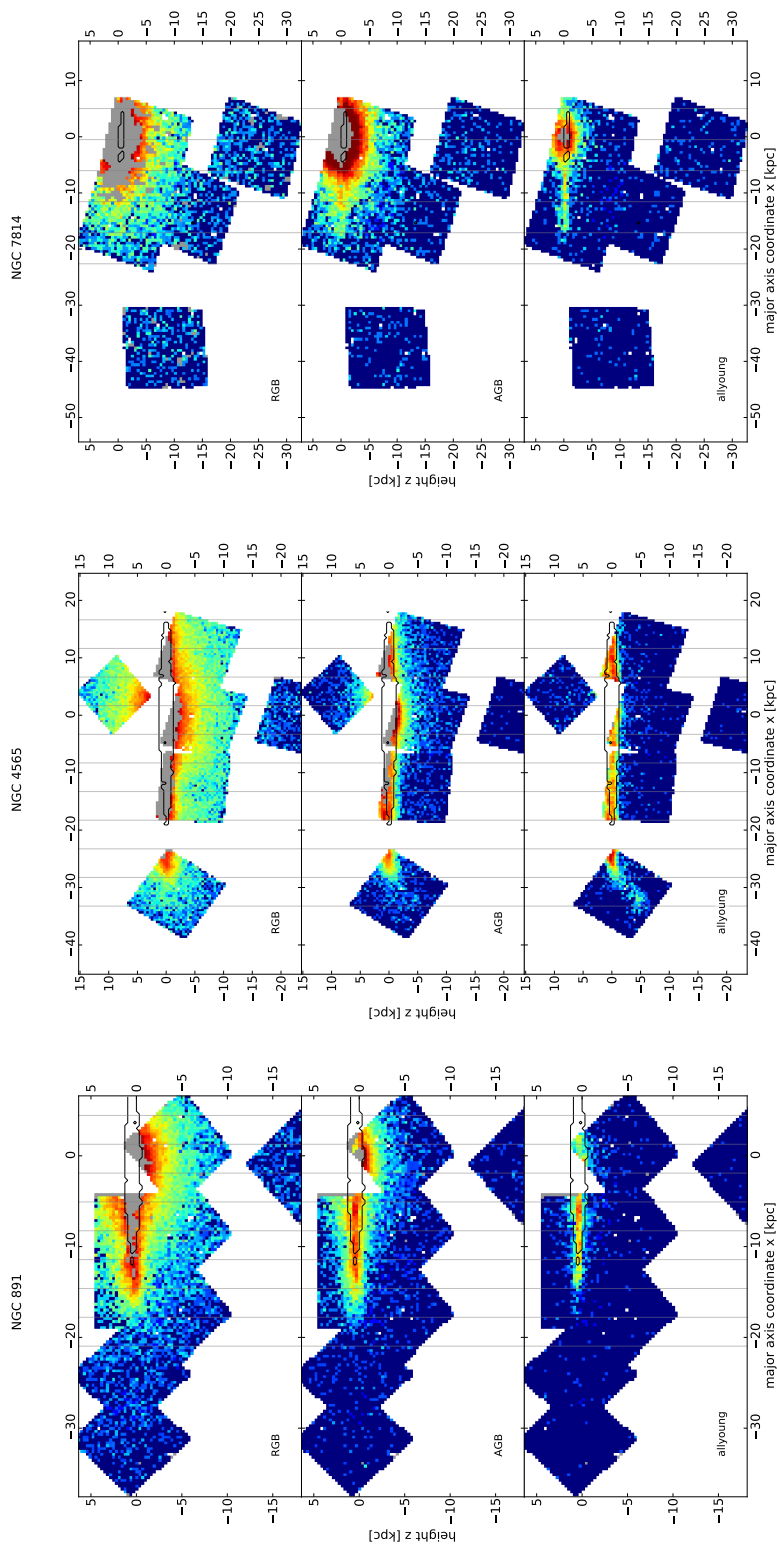
Figure 4.2.: Star count surface density maps (logarithmic scale) of stellar populations in three massive edge-on galaxies: NGC 891, NGC 4565, NGC 7814 (left to right). Central gray regions show the region that were masked due to our crowding limit, the black contour shows the dust mask. Vertical gray lines are the bin edges for the extraction of the vertical profiles in Figures 4.8–4.10.

61

Figure 4.3.: *left*: stellar surface density profile along the minor axis of NGC 891. *right*: stellar surface density profile along major axis. Data is shown as solid line, total model as dashed line, and the individual components of the model as dotted lines. Sudden jumps that appear in the data and model profiles, are due to masked pixels.

The scaleheights of the disk components increase from 320 pc for the young, over 640 pc for the AGB to 780 pc for the RGB population. The break radius is for all populations at about 13 kpc.

4.3.1.2. NGC 4565

NGC 4565 is an Sb galaxy that has a rotational velocity of $V_{rot} = 245$ km/s, the highest in our sample. Similarly to NGC 891 we fit all its populations with a two component model, containing a broken edge-on disk and a Sersic component. For the young population, the Sérsic component is again consistent with being solely due to RGB stars scattered into the "allyoung" selection box due to crowding and measurement errors. These fits describe well the structure of the populations, except for the warp that is seen at the north-western end of the disk in the AGB and young populations [Radburn-Smith et al., 2014]. This warp, which has no counterpart in our models, is masked out prior to the modeling.

As it can be seen from the slightly curved dustlane, NGC 4565 is not perfectly edge-on. We estimate the inclination of this galaxy from a ring like structure, that is seen near the center in the PAH maps. Assuming that this ring is circular and lies in the plane of the galaxy, we can infer an inclination $i = 85.5°$ from the axis ratio of this ring. This value is consistent with inclination values from the literature [$i \approx 85° - 87.5°$, i.e. Neininger et al., 1996, de Looze et al., 2012].

Assuming an edge-on configuration, the measured scaleheights increase from 640 pc for the young, to 900 pc for the AGB and to 1.2 kpc for the RGB stars; accounting for the inclination, the scaleheights are much lower: They increase from only 270 pc for the young stars to 500 pc for AGB , to 820 pc for RGB stars.[2] The break radii

---

[2]In the following sections we will always refer to the inclined measurement, if not stated otherwise.
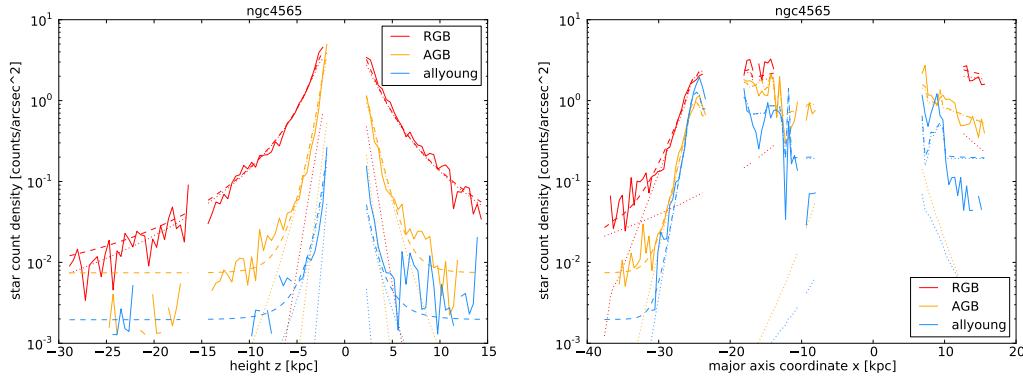
Figure 4.4.: *left*: stellar surface density profile along the minor axis of NGC 4565.
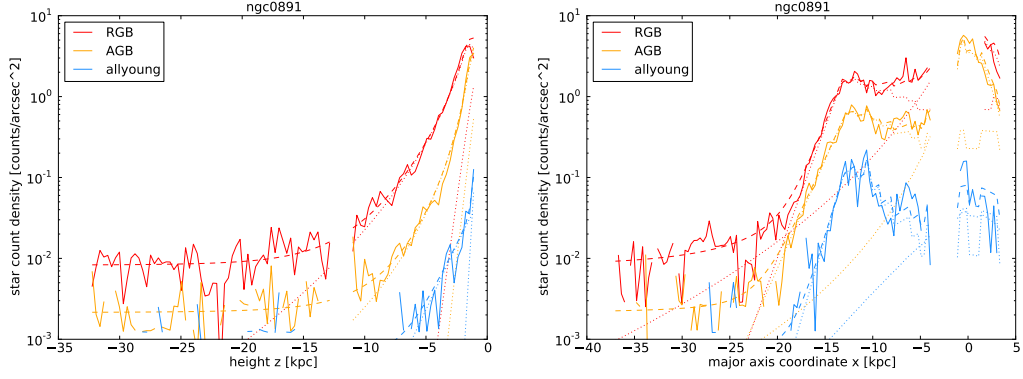   *right*: stellar surface density profile along major axis
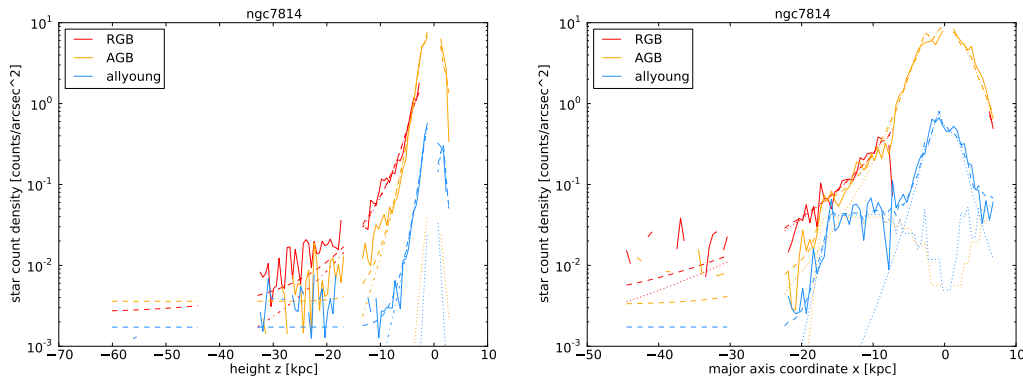
Figure 4.5.: *left*: stellar surface density profile along the minor axis of NGC 7814.
    right: stellar surface density profile along major axis

of all populations lie between 25 kpc and 27 kpc.

4.3.1.3. NGC 7814

In the Sa galaxy NGC 7814 the RGB population can be described by a single Sérsic component, while the AGB and the young population show clear signs of both a disk and a Sérsic component.

The scaleheight of the disk increases from 740 pc for the young to 950 pc for the AGB population. Both populations break around 16 kpc.

The Sérsic component of young stars is relatively stronger than in NGC 4565 or NGC 891, but it is probably still caused by scattered RGB and AGB stars. NGC 7814 has the shallowest photometry of all three galaxies (reaching only 0.5 mag below the TRGB) and the photometric uncertainty of the color of stars at the magnitude of the TRGB is about 0.3 mag. This uncertainty leads to a broad color spread of AGB and RGB stars and can scatter stars into the "allyoung" bin in the CMD. And indeed,
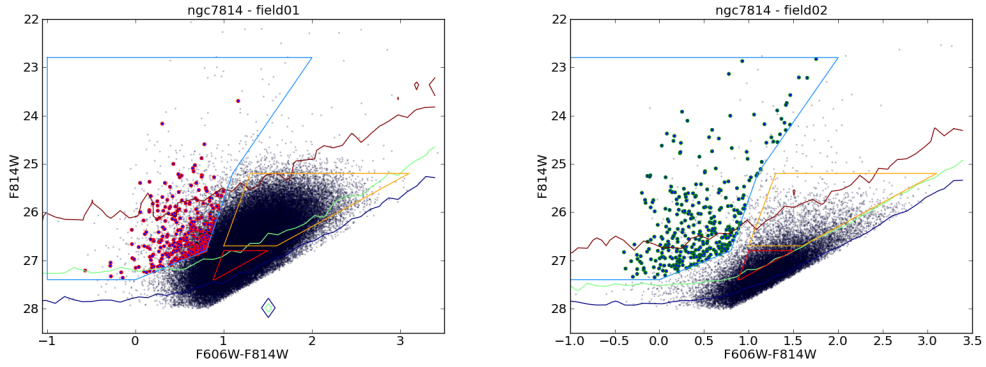
Figure 4.6.: CMDs of Field 1 and 2 in NGC 7814, with selection boxes for the three populations. The red, green and blue line shows the 80%, 50% and 20% completeness limit, respectively. Stars marked with red circles in the CMD of field 1 (left) are "allyoung" stars at large distances above the plane ($|z| > 2.5$ kpc), stars marked with green circles in the CMD of field 2 (right) are "allyoung" stars near the disk plane ($|z| < 1$ kpc).

examining the CMD of the extra-planar ($|z| > 2.5$ kpc) stars in the "allyoung" bin, we find that they cluster at the red and faint end of the allyoung selection box (see Fig. 4.6). In contrast the "allyoung" stars near the disk plane in field 2 are spread out to bluer colors and brighter magnitudes and, thus, are likely real young stars.

We can quantify the scattering of old stars into the the allyoung selection box using our model CMD (see Sec. 4.2.1): a star formation history that dropped from a constant value to zero 2 Gyr ago would result in a allyoung/RGB ratio of 2.8%. If star formation stopped 1 Gyr ago, the ratio would be 5.4%. In the offdisk region of NGC 7814 the ratio is 4.3%. This favors strongly an explanation of those stars as scattered RGB or AGB stars and against the interpretation of a really young spheroidal component.

The absence of a disk component in the RGB stars is also intriguing and can constrain the maximum age of the disk. Our RGB selection box contains mainly stars older than 2 Gyr (see Fig. 4.1) and the absence of RGB stars would indicate a maximum age smaller than this. We try to estimate the significance of the possible absence of the old disk by fitting the RGB map also with a combination of disk and Sérsic components. The resulting best fit has a disk with a scaleheight $z_0 = 1.93$ kpc and a break at $r_b = 17.3$ kpc. The disk surface density on the sky is below the density of the Sérsic component everywhere, and the disk to total mass ratio is $D/T = 0.22$. This is D/T ratio is low even compared to typical D/T values of S0 galaxies [e.g. Schulz et al., 2003].

Of course, a comparison to D/T values derived from the total light distribution is biased, because we have selected only old stars. Furthermore, due to the selection limit in color, we also impose a bias in metallicity. In NGC 7814 the lower limit of
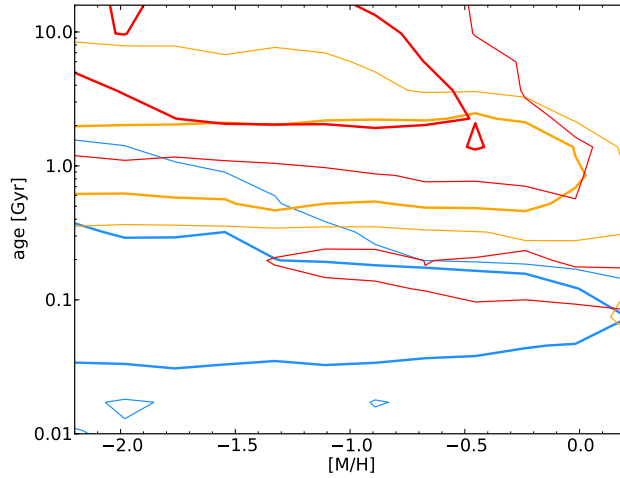
Figure 4.7.: Age-Metallicity distribution of stars in the population bins for NGC 7814, determined from the model CMDs with constant SFR and flat MDF (see Sec. 4.2.1. Colors are as in Fig. 4.1. The thin (thick) contours show the regions containing 95% (68%) of all stars in the selection boxes for RGB (red), AGB (yellow) and young (light blue) stars. Note that none of our populations contains old metalrich stars.

our selection in F606W ($m_{F606W} < 28.3$) limits the observation of the RGB to colors redder than F606W-F814W$\lesssim$ 1.2. We have shown in Chapter 2 that such a color corresponds to a metallicity of [M/H]≈ -0.7 for a globular-cluster-like population. For younger populations this limit is at higher metallicities.

In Figure 4.7 we show the age and metallicity distribution of the selected stars from our artificial CMD (generated with a constant SFR and a flat MDF, see Sec. 4.2.1). While the young and AGB selection covers the whole range of metallicities, the RGB selection is limited in metallicity. The maximum detectable metallicity evolves from [M/H]≈ -0.5 for an age of 10 Gyr to [M/H]≈ -0.1 for an age of 2 Gyr. This is a severe restriction of our observation. For comparison, the age metallicity relation of the Milky Way's thin disk evolves from [Fe/H]≈ -0.4 at an age of 10 Gyr to about solar metallicity at an age of 3 Gyr [e.g. Bergemann et al., 2014, Anguiano, 2012, Marsakov et al., 2011, Rocha-Pinto et al., 2000]. That means that the main part of a MW-like disk would not have been observed in our observational setting, which could be an explanation for the relative weakness of the observed RGB disk.

4.3.2. Scaleheights along the disk

We also examine the scaleheights as a function of the position along the galaxy disk. For the massive galaxies measuring the scaleheights is more complex than for the single component low mass galaxies of chapter 3. The bright Sérsic component
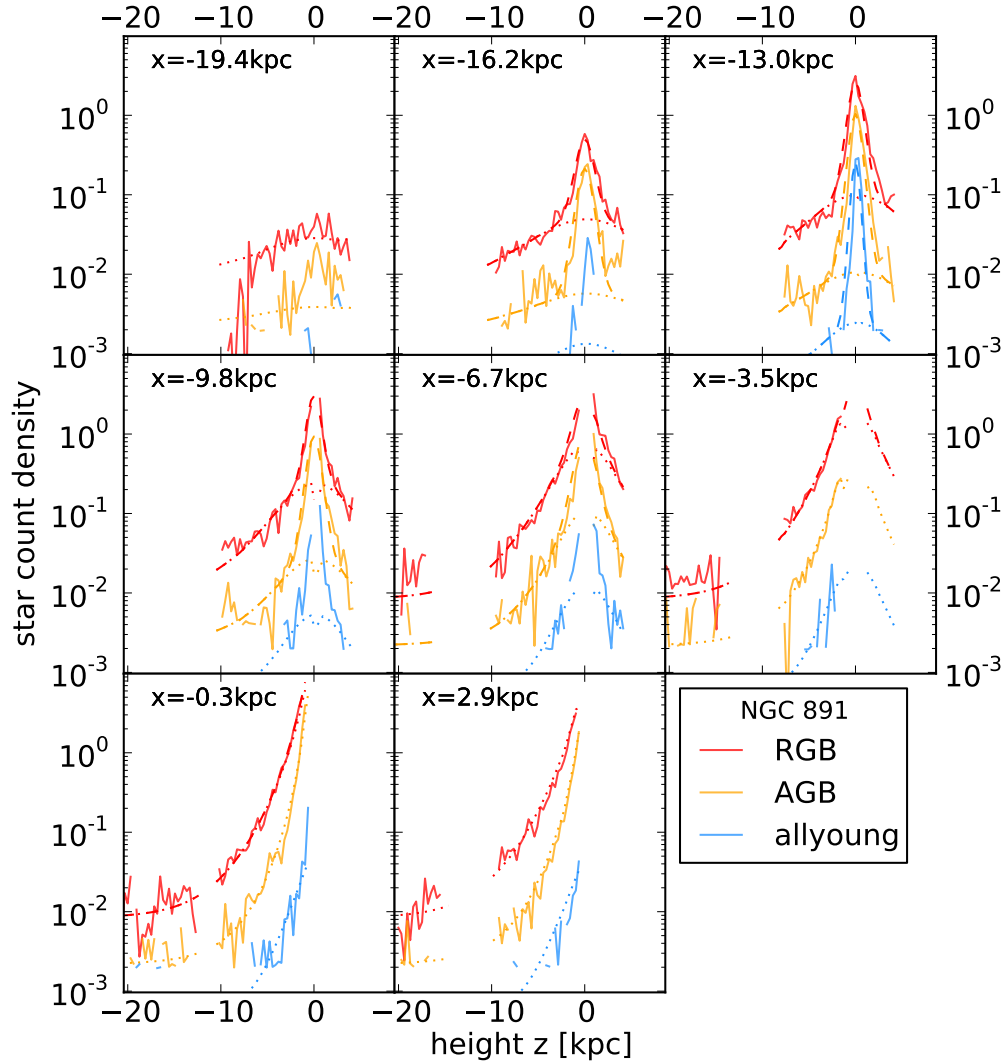
Figure 4.8.: Vertical density profiles of the three populations at different radii in NGC 891. Solid lines are the data, dotted lines are the background, i.e. contamination plus Sersic component, the dashed line the best model, consisting of background and sech^2 fits. The boundaries of the regions, where the profiles are extracted from, are shown in Fig. 4.2 as vertical gray lines.
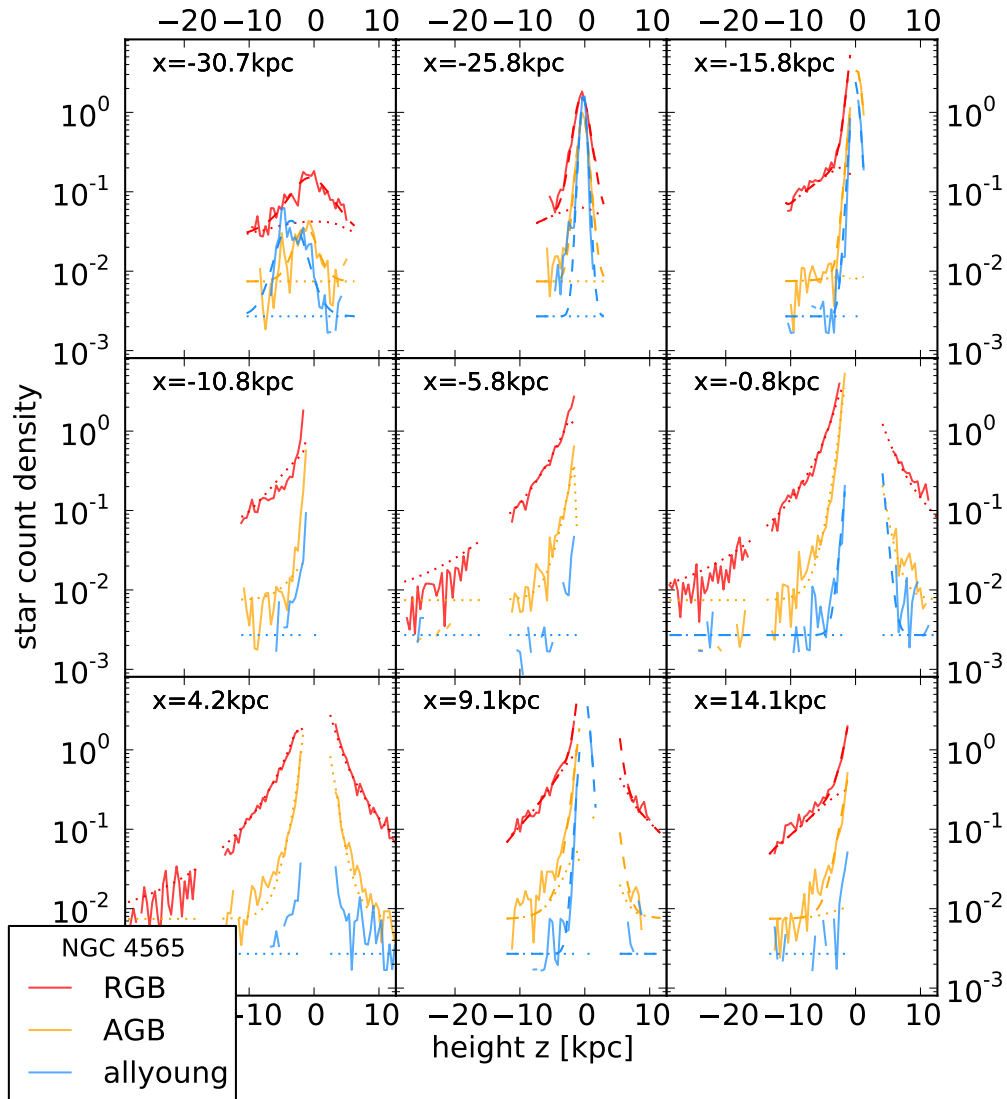
Figure 4.9.: Vertical density profiles of the three populations at different radii in NGC 4565. Line styles as in Fig. 4.8.
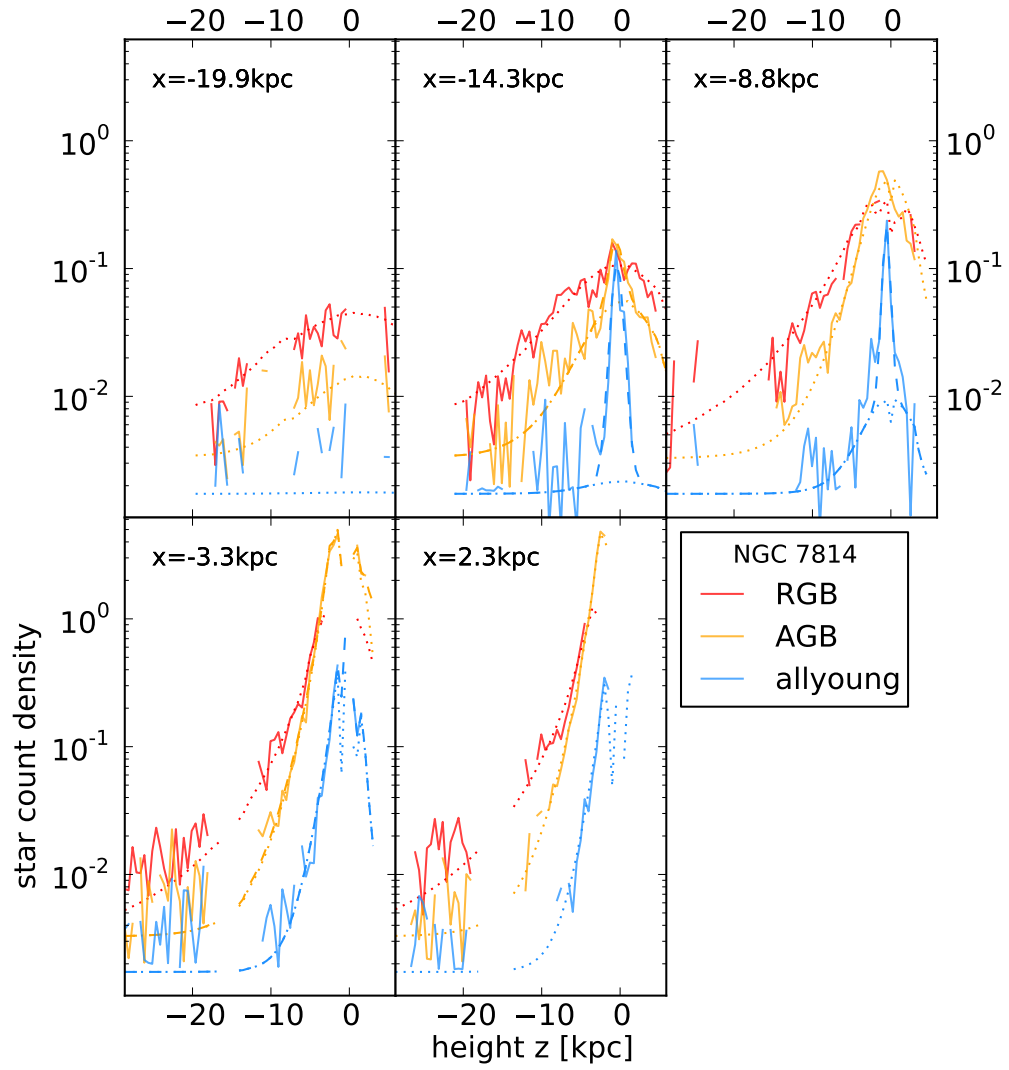
Figure 4.10.: Vertical density profiles of the three populations at different radii in NGC 7814. Line styles as in Fig. 4.8.
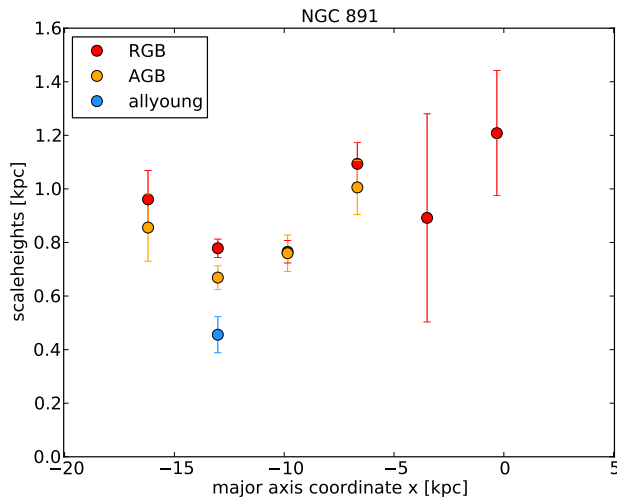
Figure 4.11.: Disk scaleheights at different radial positions along the disk of NGC 891. Near the center of the galaxy, where the bulge dominates and the masked out region is large, the scaleheight measurements are unreliable, as can be seen in the large errorbars. Values with formal errors above 60% are omitted from the plot.

affects the vertical profiles at all radii. To eliminate the influence of this bulge/halo component on our measurements, we use the Sersic component from the 2D fits as a background in our model.[3] The remaining light is then fitted with a single sech^2 profile.

Figures 4.8–4.10 show the vertical star count profiles, together with the adopted background and the best fit model. The resulting scaleheights can be seen in Figs. 4.11–4.13. Near the center of the galaxies, where the Sersic component dominates and large parts near the midplane are masked out due to crowding and/or dust, a robust measurement of the scaleheights is often impossible.

In NGC 891 we obtain reliable scaleheights for RGB and AGB stars in the galactocentric distance range of $\approx$ 10-17 kpc[4], which covers also the break radius. In this limited range the scaleheights do not change significantly, but some increase beyond the break radius is possible. The scaleheight of the young stars can only be measured near the break radius, because most of the young thin disk is covered by the dust mask.

In NGC 4565 only scaleheights beyond 10 kpc are reliable, inner regions are dom-

---

[3]We do not simply subtract the bulge/halo, because we have to keep the total number counts of stars as fit variable, in order to use the Poisson statistic for the fitting process. Would we have subtracted the Sérsic component, the remaining error distribution would have become too complex.

[4]The large scaleheight measured at $x \approx -7$ kpc is probably still strongly influenced by the Sérsic component, the peanut bulge, and the dust mask.
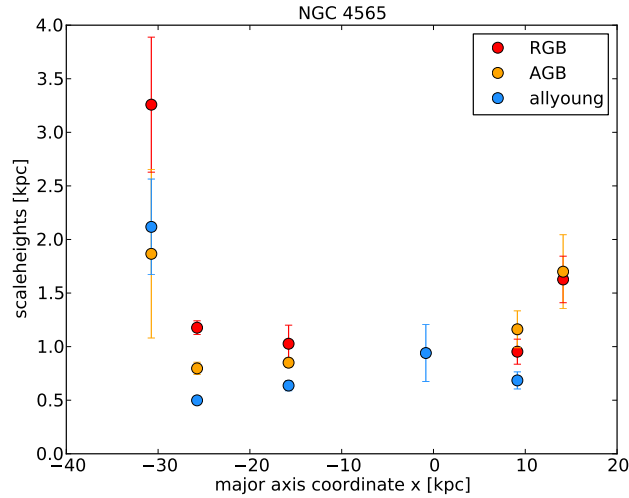
Figure 4.12.: Disk scaleheights at different radial positions along the disk of NGC 4565. Near the center of the galaxy, where the bulge dominates and the masked out region is large, the scaleheight measurements are unreliable, as can be seen in the large errorbars. Values with formal errors above 60% are omitted from the plot.

inated by a boxy bulge. At the north-western end of the disk, the two measurements inside the break radius give constant scaleheights, but beyond the break the scaleheights increase. The increase is seen both in the two strongly warped populations (young and AGB) and in the only slightly warped RGB population. At the south-eastern side, there is an increase of scaleheight in both the AGB and RGB population.

In NGC 7814 only the scaleheights of the young stars could be measured at different radii. The RGB and AGB disks are too weak. The scaleheight of young stars appears to be constant in the observed range of radii, but the uncertainties of these scaleheights are large.

4.3.3. Dependance of disk structure on age

In this section we will study the change of the structural parameters with age of the population.

All three galaxies show a clear increase of scaleheight with age (see Fig. 4.14), but the relative amount of the increase varies strongly. The increase from young to AGB populations are about 90%, 85% and 60% in NGC 891, NGC 4565 and NGC 6714, respectively. The increase for older populations also varies. In NGC 891 the scaleheight increase from AGB to RGB populations is only 20%, in NGC 4565 about 65%. In NGC 7814 the scaleheight increase from the AGB to the dubious RGB disk is about 60%.

70
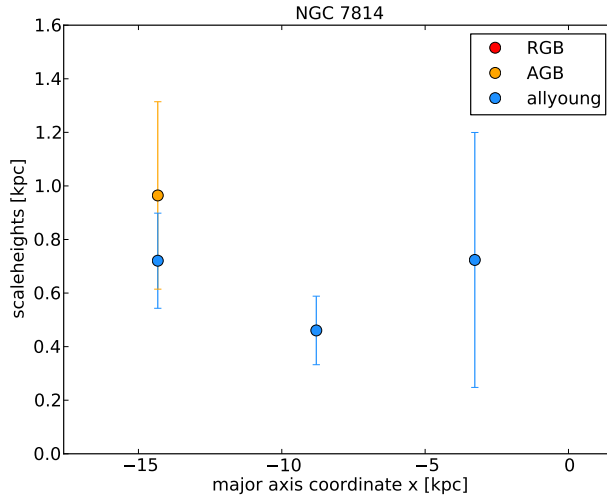
Figure 4.13.: Disk scaleheights at different radial positions along the disk of
NGC 7814. The possible disk of the RGB component of NGC 7814 could not be
measured due to its low density. Near the center of the galaxy, where the bulge
dominates and the masked out region is large, the scaleheight measurements are
often unreliable, as can be seen in the large errorbars. Values with formal errors
above 60% are omitted from the plot.

We have quantified these disk thickenings by fitting a power law $z_0 \propto t^\beta$ to our
data, Here t denotes the median age of each population (see Table 4.1). The resulting
power law indices are 0.22, 0.32 and 0.21 for NGC 891, NGC 4565 and NGC 7818,
respectively. Including the faint old disk in NGC 7814 results in $\beta = 0.29$ for this
galaxy.

From the 2D fits we also obtain values for scalelengths of the different populations;
but as we have already seen in the previous section, the area masked out due to dust
is so large, that only a small radial range of the disk between the break radius and
the dust mask can be observed. This range is too small for a reliable determination
of the scalelengths and the uncertainties are huge. Thus we do not report the
scalelengths here.

In all three galaxies the break radius is nearly independent of age: in NGC 891 it
is about 21 kpc, in NGC 4565 it is about 25 kpc and in NGC 7814 it is about 16 kpc.

4.4. Discussion

4.4.1. The effects of dust

In order to reduce the influence of dust, we have created maps of PAH emission (from
Spitzers channel 4 at 8 μm) and used them as masks for the star count data. Thus,
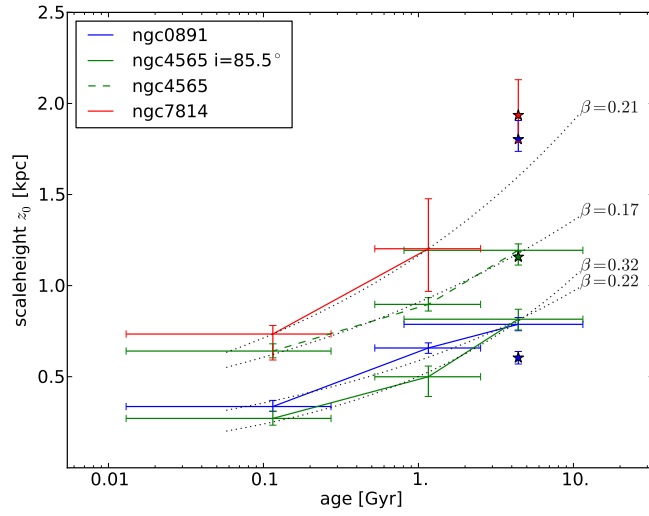
Figure 4.14.: Scaleheights as function of age; the gray dotted lines are power law fits $z_0 \propto t^\beta$ with the power law index β given in the plot. Asterisks show the scaleheights from a RGB fits with additional disk component, i.e. a thin/thick disk decomposition for NGC 891 and NGC 4565 (the possible thick disk of NGC 4565 is beyond the range of this plot: $z_0 = 8.3$ kpc), and a (possible, but weak) single old disk for NGC 7814.
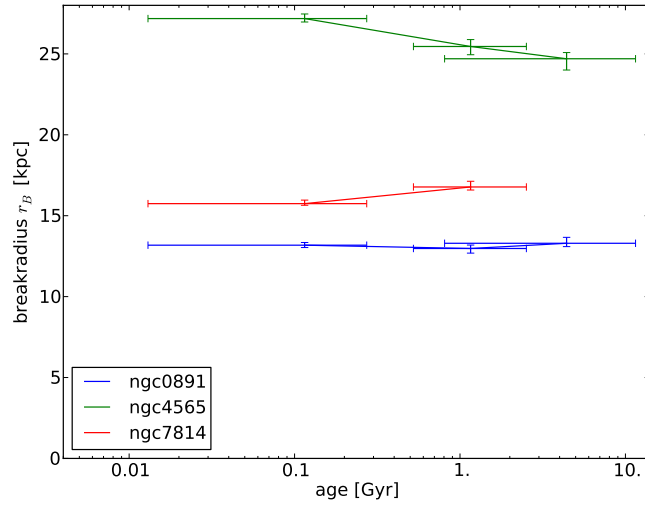
Figure 4.15.: Break radii as function of age.

the regions of highest dust extinction are excluded from the fit. We collect here information from the literature to independently check for the spatial distribution of dust and its possible effects on the star count profiles.

Table 4.2.: Scaleheights of the disks in all three galaxies.

population	NGC 891	NGC 4565 $(i = 90°)$	NGC 4565 $(i = 85.5°)$	NGC 7814
RGB	$0.788^{+0.037}_{-0.035}$	$1.194^{+0.035}_{-0.052}$	$0.816^{+0.055}_{-0.059}$	$1.936^{+0.147}_{-0.194}$
AGB	$0.658^{+0.028}_{-0.030}$	$0.897^{+0.037}_{-0.037}$	$0.500^{+0.059}_{-0.108}$	$1.202^{+0.274}_{-0.23}$
young	$0.336^{+0.034}_{-0.027}$	$0.641^{+0.040}_{-0.037}$	$0.271^{+0.040}_{-0.037}$	$0.734^{+0.047}_{-0.143}$
[3.6μm]	$0.633^{+0.002}_{-0.003}$	$0.910^{+0.002}_{-0.003}$	$0.174^{+0.014}_{-0.059}$	$0.513^{+0.017}_{-0.003}$
PAH	$0.309^{+0.001}_{-0.003}$	$0.438^{+0.001}_{-0.001}$	$0.163^{+0.001}_{-0.076}$	$0.282^{+0.012}_{-0.072}$

Notes. All values in kpc.

NGC 891: Bianchi and Xilouris [2011] have analyzed the dust content of NGC 891 using sub-mm observation with the Herschel Space Observatory. They report radial scalelengths between 4.4 kpc and 5.0 kpc, but could not resolve the vertical structure, because the disk is thinner than the beamwidth (FWHM= 18″.1); for their modeling they adopted a dust scaleheight of 0.2 kpc. Schechtman-Rook et al. [2012] determined structural parameters of the dust disk from an extinction modeling of optical HST data and find a scaleheight of $z_0 = 0.46$ kpc.

Seon et al. [2014] measured the dust structure from scattered UV-light. They need a two disk model to describe the UV light and find dust scaleheights of $z_0^{thin} \approx 0.43$ kpc and $z_0^{thick} \approx 3.1$ kpc.

NGC 4565: de Looze et al. [2012] have modeled the dust distribution in NGC 4565 using observations at multiple wavelengths and fitting the spectral energy distribution (SED). They find a dust disk with a scaleheight of $z_{0,dust} = 0.29$ kpc plus a inner dust ring with a thickness of $z_0 = 0.48$ kpc. Neininger et al. [1996] determined dust distribution with a vertical HWHM=0.43 kpc from mm observations[5], Rice et al. [1996] found $z_{0,dust} = 0.57$ kpc from an extinction analysis in the near infrared.

These scaleheights are all similar or smaller than the PAH scaleheight measured by us ($z_{0,PAH} = 0.53$ kpc); this affirms the idea that we can use the PAH images to mask out regions significantly affected by dust.

NGC 7814: The only measurement of dust thickness in NGC 7814 was done by Peletier and Knapen [1992], who determined the region of extinction from optical and NIR images. They measure for the vertical dust distribution a FWHM of 4″ (≈ 0.23 kpc), which is a little thinner than our PAH thickness (FWHM=5.5″).

---

[5]For a sech^2 distribution the half-width at half maximum (HWHM) relates to the scaleheight as HWHM= $0.88 z_0$. Thus, the equivalent scaleheight of Neininger et al. is $z_0 = 0.49$ kpc.

4.4.2. Comparison to literature values

There is a rich literature on structural measurement for the galaxies of our sample. We cannot give a full listing of all previous measurements, but we report some of them here for the comparison with our scaleheights of the resolved population. All literature measurements mentioned here are summarized in Table 4.3.

NGC 4565 and NGC 7814 are in the sample of the Spitzer Survey for Stellar Structure in Galaxies (S^4G) [Sheth et al., 2010]. For all their galaxies, the S^4G team provides structural parameters from simple 2D decompositions [Hinz et al., 2013]. A more detailed analysis of a subsample of some edge-on galaxies in the S^4G survey is presented by Comerón et al. [2011a], who performed a thin / thick disk decomposition.

All three galaxies were analyzed in a series of papers by van der Kruit and Searle [1981a,b, 1982b]. They model the disk with an $sech^2$ profile. After subtraction of the main disk, they find a thick disk like excess of light in NGC 891 and NGC 4565, which they attribute to a flattened halo that reacts to the gravitational field of the disk.

A decomposition in thin and thick disk, and halo for NGC 4565 can also be found in Wu et al. [2002], who also list a number of further older measurements, which are generally in good agreement with their results.

Morrison et al. [1997] give a thin/thick disk decomposition of NGC 891. They also describe the large degeneracies of the disk parameters when 1D vertical profiles are used for the fits. Hence they report only wide ranges of scaleheights, that give good fits to the data.

4.4.3. Age scaleheight relation

We can use the scaleheight measurements to study the heating of the galaxy disks.[6]

As it is shown in Figure 4.14, we have modeled the increase of scaleheights with age as a power law $z_0 \propto t^\beta$ with values of $\beta = 0.22$, $\beta = 0.32$ and $\beta = 0.21$ ($\beta = 0.29$) for NGC 891, NGC 4565 and NGC 7814, respectively (where the values in parentheses refer to the value obtained when including the faint old disk). Transforming these values to the corresponding power law index for an increase of the vertical velocity dispersion $\sigma_z \propto t^\alpha$ gives $\alpha = 0.11$, 0.16, 0.11 (0.15) for the three galaxies.

This puts the heating timescales of all three massive galaxies in the same regime as the low mass galaxies (see Section 3.4.3) and well below the canonical value of the Milky Way of $\alpha_{MW} \approx 0.3$ [e.g. Hänninen and Flynn, 2002]. We should note here, that the heating index α for the MW is not well constraint. Hänninen and Flynn [2002] have collected data from literature and found values between $\alpha = 0.26$ and $\alpha = 0.61$. More recent determinations by Nordström et al. [2004, $\alpha = 0.47$] and Koval' et al. [2009, $\alpha = 0.27$] fall also in this wide range. Other authors discard the

---

[6]It is possible that the increase of scaleheight (or equivalently increase of velocity dispersion) with age is caused by the decreasing thickness of gas with time (sometimes called "settling"). For the sake of simplicity, we will only write "heating", whenever we mean "heating or settling".

Table 4.3.: A (not complete) collection of scaleheight measurements from the literature.

	NGC 891	NGC 4565	NGC 7814	Ref.
counts z_0	- / 2.88			0
NIR z_0		0.77	0.50	1
		0.34 / 1.58		2
			1.2	3
optical z_0	0.95	0.94	1.9	4
		1.17 / 2.55		5
	0.8–1.3 / 3.0–5.0			6
	0.90			7
dust z_0	0.46	0.28	0.3	7, 8, 3
	0.43 / 3.1	0.49		9, 10

Notes. All values in kpc. All scaleheights are scaled to our assumed distances. If two values are given (divided by a "/"), they refer to a thin / thick disk decomposition.

References. (0) Ibata et al. [2009]; (1) Hinz et al. [2013]; (2) Comerón et al. [2011a]; (3) Peletier and Knapen [1992]; (4) van der Kruit and Searle [1981a,b, 1982b]; (5) Wu et al. [2002]; (6) Morrison et al. [1997]; (7) Schechtman-Rook et al. [2012]; (8) de Looze et al. [2012]; (9) Seon et al. [2014], (10) Neininger et al. [1996].

idea of a continuous heating, and find a saturation in velocity dispersion for stars older than a few Gyr [e.g. Carlberg et al., 1985, Edvardsson et al., 1993, Quillen and Garnett, 2001, Soubiran et al., 2008, Anguiano, 2012]. These authors usually do not determine heating indices, except for Anguiano [2012], who reports that his flattened age-velocity-relation could also be described with a power law with $\alpha = 0.12$.

Figure 4.16 illustrates the difficulties in reaching a consensus on the AVR of the MW. We show there the data from Nordström et al. [2004] and from Soubiran et al. [2008], which differ enormously, together with power law fits. For the Soubiran et al. data, we show two fits, using either all data or only data of young and intermediate age stars ($< 5\,\mathrm{Gyr}$). The fit for the full age range results in $\alpha = 0.12$, but the fit does not describe the data very well. The power law for the younger stars (before saturation sets in) fits the data well and results in $\alpha = 0.17$.

Even taking into account all the difficulties in the determination of the disk heating in the MW, we have to notice that the heating in the three external galaxies ($\alpha \lesssim 0.16$) is at the very lower end of the range of MW values ($\alpha_{\mathrm{MW}} \gtrsim 0.12$).

To better understand the discrepancy between the MW and the three galaxies, we may also compare the scaleheights directly. The thickness of the Milky Way's thin disk is usually found to range between exponential scaleheights of $h_z \approx 0.1\,\mathrm{kpc}$ for the young to $h_z \approx 0.3\,\mathrm{kpc}$ for old stars [e.g. Oort, 1932, Bok and Macrae, 1941, Schmidt, 1963, Bahcall and Soneira, 1980, Gilmore and Reid, 1983, Larsen and
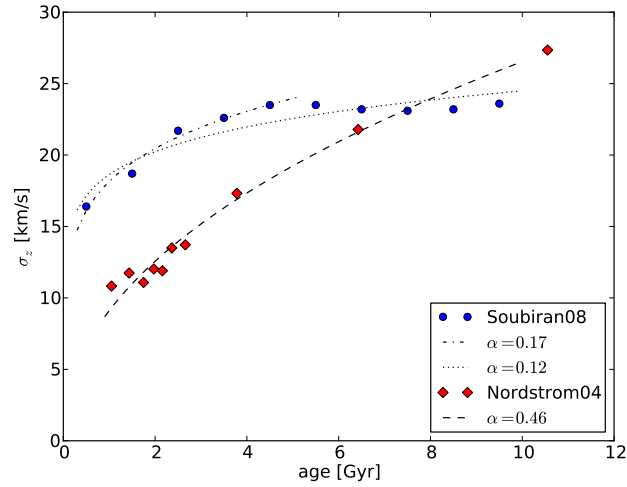
Figure 4.16.: Comparison of the AVR of Soubiran et al. [2008] and Nordström et al. [2004]. We also plot here our own power law fits to their data. For the data of Soubiran et al. we show two fits; one using the full range of ages, and one using only data up to 5 Gyr, where the saturation sets in.

Humphreys, 2003]. Transformed in the system of $sech^2$ scaleheights, this gives values between $z_0 \approx 0.2$ kpc and $z_0 \approx 0.6$ kpc. The MW's thick disk scaleheight is usually given in the range $h_z \in [0.75, 1.35]$ kpc [e.g. Gilmore and Reid, 1983, Larsen and Humphreys, 2003, Jurić et al., 2008, de Jong et al., 2010], which correspond to $z_0 \in [1.5, 2.7]$ kpc. Thus, the young disks of NGC 891 and NGC 4565 are slightly, and that of NGC 7814 is significantly thicker than the Milky Way's young thin disk and all three old disks are also thicker than the MW's old thin disk, but much thinner than the MW's thick disk.

These thicker stellar disks could be a consequence of the differences of ISM structure between the MW and our three external galaxies. The dust disk of the Milky Way has a typical scale height of $z_0 \lesssim 0.2$ kpc [e.g. Misiriotis et al., 2006, Drimmel and Spergel, 2001], with some possible flaring to $z_0 = 0.37$ kpc at $R = 15$ kpc [Drimmel and Spergel, 2001]. Similarly, the thickness of the distribution of molecular gas is very small in the MW: Misiriotis et al. [2006] find a value of $z_0 = 0.16$ kpc for H_2, Binney and Merrifield [1998] report HWHM thickness for CO of about 0.05 kpc (inside the solar circle), which flares to about 0.4 kpc in the outer disk. All these values show that the MW's cool ISM disk is thinner than both the PAH (see Table 4.2) and the dust (Sec. 4.4.1) distributions of the three external galaxies.

So we conclude here that the small heating efficiencies observed in the three galaxies of our sample might be connected to the large thickness of their original disks, which is caused by a thicker ISM distribution. In principle the finding

of a larger thickness of all galaxy components (stars and ISM) could be influenced by observational effects like a deviation from a perfect edge-on view of these galaxies. In NGC 4565 we have already accounted for the inclination, and NGC 891 and NGC 7814 have perfectly straight dust lanes, which make a smaller inclination unlikely.

4.4.4. Occurrence of thick disks

In Sec. 4.3 we report that we do not find thick disks in any of the three galaxies. This is surprising, because thick disks are now thought to be ubiquitous [Dalcanton and Bernstein, 2002] and are found in practically every galaxy, where they are looked for [e.g., Yoachim and Dalcanton, 2006, Comerón et al., 2011a]. Before we discuss the consequences of our findings, we will first check, whether our observations are actually consistent with having a thick disk.

For this purpose we have fitted the RGB density maps of NGC 891 and NGC 4565 (in NGC 7814 the possible RGB disk is too faint for including yet another disk, see Sec. 4.3.1.3) with a three component model containing a thin disk, a thick disk and a Sérsic component. The results of this can be see in Figs. C.1 to C.4 (for NGC 891) and Figs. C.7 to C.10 (for NGC 4565) in the appendix. Formally, the three component fits are much better[7], but from the residual map and the profile comparison their advantage over the two component fits is not obvious.

In NGC 891 the scaleheights from the two-disks fit are $z_{0,thin} = 0.60$ kpc and $z_{0,thick} = 1.80$ kpc, which would make the RGB thin disk scaleheight smaller than the AGB scaleheight. Such an decrease of scaleheight with age is also in contrast with earlier observations and simulations, and would complicate the interpretation of the low heating rates (see previous section) even more.

In NGC 4565 the two scaleheights are $z_{0,thin} = 1.16$ kpc and $z_{0,thick} = 8.3$ kpc[8]. Here the thin disk scaleheight is almost the same as in the single disk fit and the thick disk essentially fits, what was the extended Sérsic component in the single disk fit. This improves the fit mainly in the region beyond the break radius, where the disk is warped.

In Figure 4.17 we compare the scaleheight measurements with thin–thick disk decompositions of Yoachim and Dalcanton [2006] and Comerón et al. [2011a], together with the scaleheights of the low mass disks from Chapter 3. We see here that the main disk scaleheights of the different population all fall in the regime of typical thin disk scaleheights, similar to what we found for the low-mass galaxies. Only the dubious, but possible, measurement of a second disk scaleheight of NGC 891, and the very faint RGB disk of NGC 7814 could be interpreted as typical thick disks. But as mentioned before, this second disk does not improve the agreement of the

---

[7]The relative goodness of the fits with a different number of free parameters can be evaluated e.g. through the Bayesian information criterion (BIC). The BIC for the three component fits is lower by 500 in NGC 891, and by 600 in NGC 4565. In statistics, a decrease of the BIC by 10 already indicates a superior model.

[8]For the comparison in this section, we have used the edge-on configuration in the fit.
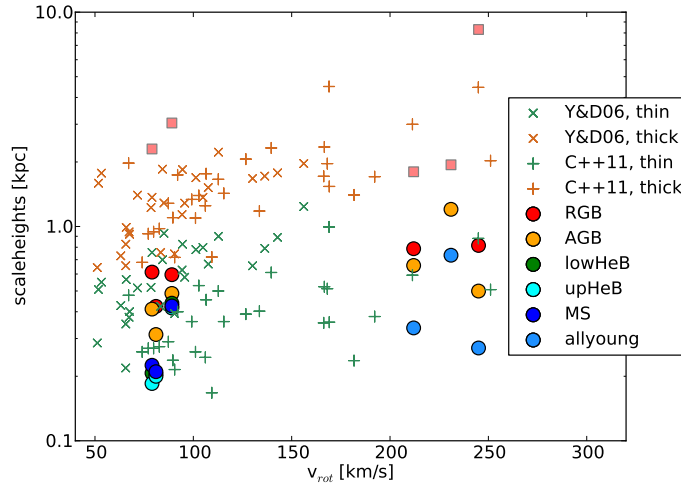
Figure 4.17.: Comparison of our measured scaleheights, now including the massive galaxies, with data from Yoachim and Dalcanton [2006] and Comerón et al. [2011a]. The colored circles show our results for the different populations; squares show the faint extended component for the low mass galaxies (Sect. 3.3.3.2) and possible, but not necessary measurements of additional disks for the massive galaxies.

model with the data.

In summary, we have presented here, including the results from chapter 3, the vertical star count profiles of six galaxies, of which all can be described without a separate thick disk. Even though we cannot rule out the presence of thick disks in the massive galaxies, our lack of their detection is astonishing, because lately thick disks were found to be ubiquitous [e.g. Dalcanton and Bernstein, 2002, Comerón et al., 2011a].

Why do other authors find thick disks, while we do not, notwithstanding that star count profiles allow us to reach fainter levels, where thick disks should dominate? Possible sources of errors, that could lead to a spurious detection or an overestimation of a thick disk, include: a) problems with flat fielding and sky subtraction; b) unaccounted effects of extended point spread functions (PSF); or c) insufficient halo/bulge modeling.

The importance of good sky subtraction: Thick disks are intrinsically faint objects. Their surface brightness usually lies below that of the sky, which makes a careful analysis and subtraction of the sky crucial for the detection and characterization of thick disk. A slightly underestimated or variable sky brightness can lead to misinterpretations of the data. Data from the Spitzer Space Telescope is
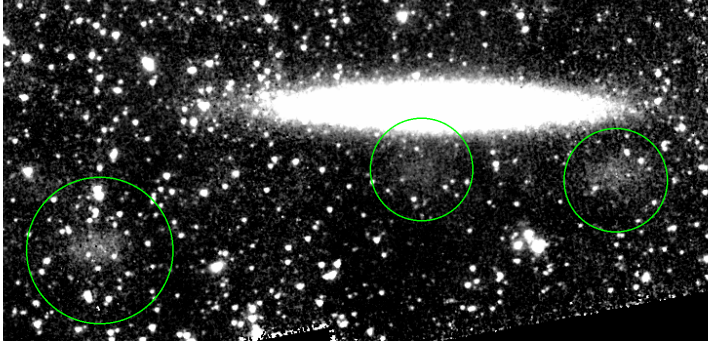
Figure 4.18.: Artifacts in an Spitzer IRAC (channel 1) image of NGC 5023. Regions of increased sky surface brightness are highlighted with green circles. The effect of the bright region near the center of NGC 5023 can also be seen in the vertical profile in Fig. 3.16: The bump at z=-2 kpc with $m_{3.6} \approx 24.5$ mag/arcsec^2 is caused by this artifact.

especially known to have problems with spatially varying sky brightness and image artifact as persistent images, scattered light or optical ghosts [see the Spitzer IRAC manual for details: Spitzer IRAC Instrument and Instrument Support Teams, 2013]. An example of such artifacts is shown in Fig. 4.18.

The effect of extended PSFs: Even more crucial for the characterization of faint galaxy components is the correct modeling of the PSF. As de Jong [2008] pointed out, extended tails of the PSF can account for most of the light that is observed in a faint galactic halo. More recently, Sandin [2014, 2015] showed that the treatment of extended PSFs is also crucial for observations of thick disks and "anti-truncated" radial profiles in edge-on galaxies. The important fact, that has often been underestimated, is that at any given point the extended PSF light from the whole disk is integrated. That means that for a vertical surface brightness profile at some distance from the center of the galaxy, one has to take into account also the light from the galaxy's center (and actually the whole disk), which gets scattered into the relevant radial bin.

We illustrate this effect in Fig. 4.19, where we show a vertical profile through a model galaxy image, which resembles NGC 4565 in size, brightness, and morphology. This model profile was taken at a distance of 8.5 kpc from the galaxy's center, where the bulge has an only small (but still significant) effect. The comparison between the model convolved with the PSF and the unconvolved model reveals a clear excess of light in the model with the PSF, which could be misclassified as a thick disk. This excess is significant, though the inner part of the PSF drops by more than 10 magnitudes within a few arcseconds.

Looking at the two papers with the largest samples of thick disk measurements, namely Comerón et al. [2011a] and Yoachim and Dalcanton [2006], we have to realize
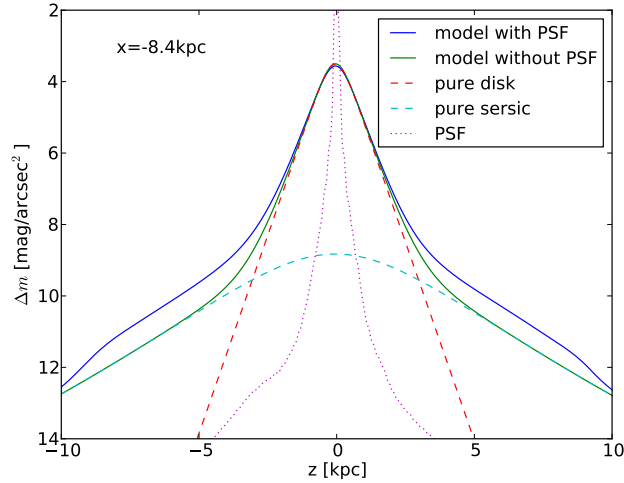
Figure 4.19.: Vertical surface brightness profile for a galaxy model resembling NGC 4565. The model consist of an sech^2 disk (red dashed line) and a Sérsic bulge (cyan dashed line). The green solid line shows the total model before convolving with the PSF of Spitzer's channel 1, the blue line the convolved model. The profile is extracted at a distance of 8.5 kpc from the center of the galaxy. Note: Spitzer's PSF is truncated at $r = 160''$, which scales to about 9.2 kpc here; this means that we still underestimate the effect of scattered light in this example (and it causes the steepening of the profile for $|z| > 9$ kpc).

that neither of them has included the (extended) PSF in their models. Comerón et al. [2011a] only convolve their vertical profiles with a Gaussian with a width of 2.2″, which is the FWHM of Spitzer's PSF; Yoachim and Dalcanton [2006] consider the PSF of no importance, because a convolution with a Gaussian PSF template does not change their results. Dalcanton and Bernstein [2002], who found thick disks through vertical color gradients (in the same data as Yoachim and Dalcanton [2006]), also consider PSF effects unimportant, because their PSF decreases faster than the light in their vertical profiles. This is exactly the kind of assumption that was proven wrong by Sandin [2015].

The effect of additional (spheroidal) components: While the integrated light data of thick disk discoveries might be hampered by PSF effects, star count data is not. Using ACS on HST, Ibata et al. [2009] find a thick disk in star count data of NGC 891 and measure its exponential scaleheight to be $h_z = 1.4$ kpc. Actually, they even use the same field that is also part of our data. How could it happen, that they measure a thick disk, while we do not detect it? The main difference between their analysis and ours is the way we model thin disk and spheroid. Ibata et al. measure the scaleheight by fitting an exponential function to some part of

their 1D vertical profile. For this measurement, they mask out the inner regions of the disk (mainly because of incompleteness and crowding) and ignore the halo[9]. With the same method, we can also find a region in our vertical profile of NGC 891 that can be approximated with an exponential of scaleheight similar to a thick disk; but the more advanced 2D analysis shows, that this apparent thick disk slope can also be reproduced by the transition between the steeper slope of the thin disk and the shallower slope of the Sérsic, when these two components are added together. This renders a separate thick disk unnecessary and shows the importance of a (preferentially two dimensional) multi-component fit.

Note that also Comerón et al. [2011a] and Yoachim and Dalcanton [2006] have not included a bulge or halo component in their fits. In their case of using a sample of low-mass and almost bulge-less galaxies that might be justified. In principle, one has to carefully check, whether such an assumption is justified, because the outer regions of a Sérsic component can also mimic an additional disk component in one dimensional vertical profiles (see Fig. 4.19).

While we have here described some of the problems that most thick disk studies in external galaxies might have encountered, it is still possible that all galaxies have thick disks. Our finding that our star count maps can be well described without thick disks only means, that they are fainter than expected. Between the massive thin disks and the extended bulge/halo component there is just no region, where a thick disk would clearly dominate the star count numbers. This makes the detection of thick disks ambiguous and any small density variation could mimic a thick disk.

4.5. Conclusions and Summary

In this chapter we have analyzed the star count maps of three massive edge-on galaxies. We have determined the structures of their different stellar populations and measured their scaleheights as a function of stellar age.

For all three galaxies we find very low heating rates, which resemble more the heating of low-mass galaxies, and are lower than the heating rate of the Milky Way. Especially their young disks are much thicker than the Milky Way young disk, which can be explained as a consequence of their different structure of the ISM.

In none of the galaxies we can detect a clear separate thick disk in their old population. While the early type galaxy NGC 7814 does only have a very subtle old disk at all, the old populations of the other two galaxies, NGC 891 and NGC 4565, can be well described with a single disk plus Sérsic model. This finding, together with the single disk nature of the low mass galaxies from chapter 3, is in contrast to the ubiquitous finding of thick disks in external galaxies by integrated light studies. At the same time, these thick disk observations are also questioned by Sandin [2015],

---

[9]In their paper they actually do also analyze the halo, but for this measurement of the thick disk scaleheight, they simple cut the fit region at a height $|z| = 5$ to avoid the halo.

who found that the observed low surface brightness components could mainly be explained by scattered light.

Thus, thick disks might be either less ubiquitous or at least less massive than it was thought the last years, and their detection is more difficult and subtle than anticipated.

5. Concluding Remarks

5.1. Summary

In this thesis we have presented the analysis of resolved stellar populations for the study of galaxy formation and evolution.

In chapter 2 we presented a new calibration of the color metallicity relation of RGB stars in the Hubble filter system. This allows a metallicity determination of old populations that does not rely on stellar evolution models, and that directly compares to the globular cluster metallicity scale, without the need of filter transformations, that usually introduce additional uncertainties.

In chapters 3 and 4 we have analyzed the structure of stellar populations as a function of their age in six edge-on disk galaxies. Our two main results in these chapters are:

1.) All galaxies have a slow increase of scaleheight with age. When expressed as a power law $z_0 \propto t^\alpha$, the power law index α of all galaxies is lower than that of the Milky Way. For the low mass galaxies, a lower heating rate can be explained by their more diffuse interstellar medium and the higher stability of their disk, which leads to fewer and weaker scattering entities (e.g. GMC or spiral arms). For the massive galaxies such a slow vertical heating of the stars (or equivalent slow settling of the gas) is more difficult to explain. But we notice that already the scaleheights of their young populations and of their dust are larger than those in the Milky Way.

2.) None of the galaxies shows a clear signature of a separate thick disk. In the low mass galaxies the vertical star count profiles of old stars can be described with a single disk over a range of more than three orders of magnitudes in star count density, which is equivalent to about eight magnitudes in surface brightness. At even lower densities, a faint halo with a mass below 1% of the disk's mass is detected in two of the low mass galaxies. In the massive galaxies, the star count density of each population can be modeled with a disk plus Sérsic model. The Sérsic component contributes significantly to the vertical profiles even at large distances from the galactic center, and could hide a fainter thick disk. Thus, we cannot exclude the presence of thick disks in the massive galaxies.

5.2. Outlook

Our findings of low heating rates and weak thick disks are interesting and surprising, and it would be helpful to verify these results either through a study of a larger sample of galaxies, a deeper analysis of these galaxies, or some other methods.

5. Concluding Remarks

Studies of resolved stellar population in galaxy disk beyond the local group can only be done with HST at the moment. No other telescope has the spatial resolution to resolve individual stars in the crowded regions of galaxy disks at these distances. And even HST comes to its limits in the current study; large parts of the inner disk and the bulge could not be resolved due to a high crowding. Furthermore, observations of galaxies with distances larger than 10 Mpc are very expensive: NGC 4565 and NGC 7814 needed 6 and 7 orbits per pointing, respectively, to get the relatively shallow CMDs used in this study. This means, that extending the survey to other galaxies in that distance or beyond is practically unfeasible. On the other hand, all massive edge-on galaxies within that distance range have been observed already. Table 5.1 list all spiral galaxies with $D < 10$ Mpc and inclination $i > 70°$ from the HyperLEDA database, together with our assessment of their edge-on status[1] and a note on available HST data. It is evident that all massive ($V_{rot} > 150$ km/s) edge-on galaxies have been included in this study, and we could only extend this work to a small sample of intermediate mass galaxies (namely NGC 4437, NGC 4631, NGC 7090) or to low mass galaxies.

Future Observatories: The next big step for the study of extragalactic resolved stellar populations will be the launch of the James Webb Space Telescope (JWST), which is planned for fall 2018. JWST is a near infrared telescope with an aperture of about six meter. Its Near Infrared Camera (NIRCam) will be able to observe in wavelengths of 0.6 μm to 5 μm. At 2 μm, its spatial resolution will be similar to HST in the optical, for smaller wavelength the PSF will be even narrower, but highly undersampled. Its much larger mirror will enable it to map nearby galaxies much faster than HST and to resolve RGB stars to a much larger distance (up to 40 Mpc), which includes e.g. the Virgo cluster and enlarges the number of resolvable galaxies. Furthermore, its wavelength range in the near infrared will decrease the effects of dust extinction. This will make it the ideal tool for the study of resolved stars in galaxies [for more details see Brown et al., 2008, or the JWST webpages `http://www.stsci.edu/jwst/`]. A comparison of relevant parameters of both telescopes is given in Table 5.2.

With the improvement of adaptive optics (AO) systems and larger telescopes, the spatial resolution of ground based telescopes will also increase, which will make studies of resolved stars possible from the ground. Deep et al. [2011] and Greggio et al. [2012] studied the expected possibilities of the Multi-AO Imaging Camera for Deep Observations (MICADO) at the European Extremely Large Telescope (E-ELT) for the study of resolved populations. They find that E-ELT/MICADO is well suited for resolving stars in very crowded regions (e.g. elliptical galaxies in the Virgo cluster). For very crowded regions ($\mu_V < 22$ mag/arcsec^2) the E-ELT will be superior to JWST, because its large aperture will lead to a narrower PSF, when the telescope is used at the diffraction limit. On the hand JWST will be

---

[1]The inclination parameter of HyperLeda is not very reliable. In many galaxies with $i = 90°$ we can actually see clear signs of a lower inclination, e.g. spiral arms or a curved dust lane.

Table 5.1.: Overview of nearby ($D < 10\,\text{Mpc}$) possibly edge-on disk galaxies (plus the two galaxies from this study with $D > 10\,\text{Mpc}$ and NGC 4244).

name	type	incl	$(m-M)_0$	V_{rot}	HST data	comment
NGC 4565	Sb	90.0	30.41	244.29	GHOSTS	this work
NGC 7814	Sab	70.6	30.80	230.27	GHOSTS	this work
NGC 0891	Sb	90.0	29.96	212.09	GHOSTS	this work
NGC 2683	Sb	82.8	29.88	202.57	TRGB	not edge-on
NGC 0253	SABc	90.0	27.84	189.80	GHOSTS	not edge-on
NGC 4945	SBc	90.0	27.70	166.96	GHOSTS	not edge-on
NGC 4437	Sc	90.0	29.69	139.57	TRGB	
NGC 4631	SBcd	90.0	29.33	138.37	GHOSTS	interacting
NGC 7640	Sc	85.7	29.97	107.91	TRGB	not edge-on
NGC 7090	Sc	90.0	28.99	101.96	TRGB	
NGC 4244	Sc	65.4	28.20	97.83	GHOSTS	this work
ESO 373-008	Sc	78.6	29.93	96.52	-	
NGC 4312	Sab	90.0	29.84	94.63	-	
NGC 4490	SBcd	79.0	29.82	89.75	-	interacting
NGC 0247	SABc	76.4	27.85	84.53	GHOSTS	not edge-on
NGC 5023	Sc	90.0	29.09	80.29	GHOSTS	this work
IC 5052	SBcd	90.0	28.90	80.16	GHOSTS	this work
NGC 7462	SBbc	90.0	29.95	79.69	-	
ESO 274-001	Scd	90.0	27.23	73.99	TRGB	

Notes. Morphological type, inclination, distance modulus, and rotational velocity are taken from HyperLeda. Since the inclination parameter provided by HyperLeda is rather uncertain, we set a low limit ($i > 70°$) in the preselection for this table. Galaxies, that show up as less inclined in an optical inspection, are marked in the comment column. The column "HST data" gives information about available HST data, that could be used for a resolved stellar population study; the entry "TRGB" means that there is (at least) one field that resolves the tip of the red giant branch, "GHOSTS" galaxies have multiple fields that usually reach $2\,\text{mag}$ below the tip.

superior in mapping less crowded regions, due to its larger field of view and lower sky background. So E-ELT and JWST will be highly complimentary, with JWST having the advantage of being on sky about six years earlier than the E-ELT.

Table 5.2.: Comparison of spatial resolution and Field-of-View (FOV) of different observatories

	HST/ACS	JWST/NIRCAM	E-ELT/MICADO
pixel scale [$''$]	0.05	0.034	0.003
$R_{0.5}$ [$''$]	0.07	0.05	0.013
$R_{0.9}$ [$''$]	0.4	0.4	0.29
FOV [$''$]	202x202	130x130	53x53
aperture [m]	2.4	6	39

Notes. $R_{0.5}$ and $R_{0.9}$ are the radii that include 50% and 90% of the total energy of the PSF.

Bibliography

M. G. Abadi, J. F. Navarro, M. Steinmetz, and V. R. Eke. Simulations of Galaxy Formation in a Λ Cold Dark Matter Universe. II. The Fine Structure of Simulated Galactic Disks. *ApJ*, 597:21–34, November 2003. doi: 10.1086/378316.

J. Anderson, A. Sarajedini, L. R. Bedin, I. R. King, G. Piotto, I. N. Reid, M. Siegel, S. R. Majewski, N. E. Q. Paust, A. Aparicio, A. P. Milone, B. Chaboyer, and A. Rosenberg. The Acs Survey of Globular Clusters. V. Generating a Comprehensive Star Catalog for each Cluster. *AJ*, 135:2055–2073, June 2008. doi: 10.1088/0004-6256/135/6/2055.

B. Anguiano, K. Freeman, M. Steinmetz, and E. W. de Boer. The kinematical evolution of the Galactic disk. In *European Physical Journal Web of Conferences*, volume 19 of *European Physical Journal Web of Conferences*, page 5009, February 2012. doi: 10.1051/epjconf/20121905009.

Borja Anguiano. *The Age-Metallicity-Velocity relation in the nearby disk.* PhD thesis, Universität Postdam, Potsdam, Germany, March 2012.

R. Azzollini, I. Trujillo, and J. E. Beckman. Color Profiles of Disk Galaxies since $z \approx 1$: Probing Outer Disk Formation Scenarios. *ApJ*, 679:L69–L72, June 2008a. doi: 10.1086/589283.

R. Azzollini, I. Trujillo, and J. E. Beckman. Cosmic Evolution of Stellar Disk Truncations: From $z \approx 1$ to the Local Universe. *ApJ*, 684:1026–1047, September 2008b. doi: 10.1086/590142.

C. Babusiaux, G. Gilmore, and M. Irwin. A near-infrared and optical photometric study of the Sculptor dwarf spheroidal galaxy: implications for the metallicity spread. *MNRAS*, 359:985–992, May 2005. doi: 10.1111/j.1365-2966.2005.08959.x.

J. N. Bahcall and R. M. Soneira. The universe at faint magnitudes. I - Models for the galaxy and the predicted star counts. *ApJS*, 44:73–110, September 1980. doi: 10.1086/190685.

J. Bakos, I. Trujillo, and M. Pohlen. Color Profiles of Spiral Galaxies: Clues on Outer-Disk Formation Scenarios. *ApJ*, 683:L103–L106, August 2008. doi: 10.1086/591671.

B. Barbanis and L. Woltjer. Orbits in Spiral Galaxies and the Velocity Dispersion of Population i Stars. *ApJ*, 150:461, November 1967. doi: 10.1086/149349.

A. Bellini, G. Piotto, A. P. Milone, I. R. King, A. Renzini, S. Cassisi, J. Anderson, L. R. Bedin, D. Nardiello, A. Pietrinferni, and A. Sarajedini. The Intriguing Stellar Populations in the Globular Clusters NGC 6388 and NGC 6441. *ApJ*, 765:32, March 2013. doi: 10.1088/0004-637X/765/1/32.

G. J. Bendo, B. T. Draine, C. W. Engelbracht, G. Helou, M. D. Thornley, C. Bot, B. A. Buckalew, D. Calzetti, D. A. Dale, D. J. Hollenbach, A. Li, and J. Moustakas. The relations among 8, 24 and 160 μm dust emission within nearby spiral galaxies. *MNRAS*, 389:629–650, September 2008. doi: 10.1111/j.1365-2966.2008.13567.x.

Bibliography

T. Bensby, A. Alves-Brito, M. S. Oey, D. Yong, and J. Meléndez. A First Constraint on the Thick Disk Scale Length: Differential Radial Abundances in K Giants at Galactocentric Radii 4, 8, and 12 kpc. *ApJ*, 735:L46, July 2011. doi: 10.1088/2041-8205/735/2/L46.

M. Bergemann, G. R. Ruchti, A. Serenelli, S. Feltzing, A. Alves-Brito, M. Asplund, T. Bensby, P. Gruyters, U. Heiter, A. Hourihane, A. Korn, K. Lind, A. Marino, P. Jofre, T. Nordlander, N. Ryde, C. C. Worley, G. Gilmore, S. Randich, A. M. N. Ferguson, R. D. Jeffries, G. Micela, I. Negueruela, T. Prusti, H.-W. Rix, A. Vallenari, E. J. Alfaro, C. Allende Prieto, A. Bragaglia, S. E. Koposov, A. C. Lanzafame, E. Pancino, A. Recio-Blanco, R. Smiljanic, N. Walton, M. T. Costado, E. Franciosini, V. Hill, C. Lardo, P. de Laverny, L. Magrini, E. Maiorca, T. Masseron, L. Morbidelli, G. Sacco, G. Kordopatis, and G. Tautvaišienė. The Gaia-ESO Survey: radial metallicity gradients and age-metallicity relation of stars in the Milky Way disk. *A&A*, 565:A89, May 2014. doi: 10.1051/0004-6361/201423456.

E. Bertin and S. Arnouts. SExtractor: Software for source extraction. *A&AS*, 117:393–404, June 1996.

S. Bianchi and E. M. Xilouris. The extent of dust in NGC 891 from Herschel/SPIRE images. *A&A*, 531:L11, July 2011. doi: 10.1051/0004-6361/201116772.

James Binney and Michael Merrifield. *Galactic astronomy*. Princeton series in astrophysics. Princeton Univ. Press, Princeton, NJ, 1998. ISBN 0-691-00402-1 ; 0-691-02565-7 ; 978-0-691-02565-0 pbk.

James Binney and Scott Tremaine. *Galactic dynamics*. Princeton series in astrophysics. Princeton University Press, Princeton, NJ, 2. ed. edition, 2008. ISBN 978-0-691-13027-9 ; 978-0-691-13026-2.

J. C. Bird, S. Kazantzidis, D. H. Weinberg, J. Guedes, S. Callegari, L. Mayer, and P. Madau. Inside out and Upside down: Tracing the Assembly of a Simulated Disk Galaxy Using Mono-age Stellar Populations. *ApJ*, 773:43, August 2013. doi: 10.1088/0004-637X/773/1/43.

Paul T. Boggs, Richard H. Byrd, and Robert B. Schnabel. A stable and efficient algorithm for nonlinear orthogonal distance regression. *SIAM Journal on Scientific and Statistical Computing*, 8(6):1052–1078, 1987. doi: 10.1137/0908085. URL http://link.aip.org/link/?SCE/8/1052/1.

Paul T. Boggs, Richard H. Byrd, Janet E. Rogers, and Robert B. Schnabel. *User's Reference Guide for ODRPACK Version 2.01 Software for Weighted Orthogonal Distance Regression*. U.S. Department of Commerce, Technology Administration, National Institute of Standards and Technology, June 1992. URL http://www.netlib.org/odrpack/guide.ps.

S. Boissier and N. Prantzos. Chemo-spectrophotometric evolution of spiral galaxies - I. The model and the Milky Way. *MNRAS*, 307:857–876, August 1999. doi: 10.1046/j.1365-8711.1999.02699.x.

B. J. Bok and D. A. Macrae. The Stellar Distribution in High and Intermediate Latitudes. *Annals of the New York Academy of Sciences*, 42:219, October 1941. doi: 10.1111/j.1749-6632.1941.tb55394.x.

R. Bottema. The Stellar Kinematics of Galactic Disks. *A&A*, 275:16, August 1993.

F. Bournaud, B. G. Elmegreen, and M. Martig. The Thick Disks of Spiral Galaxies as Relics from Gas-rich, Turbulent, Clumpy Disks at High Redshift. *ApJ*, 707:L1–L5, December 2009. doi: 10.1088/0004-637X/707/1/L1.

J. Bovy, H.-W. Rix, and D. W. Hogg. The Milky Way Has No Distinct Thick Disk. *ApJ*, 751:131, June 2012a. doi: 10.1088/0004-637X/751/2/131.

J. Bovy, H.-W. Rix, C. Liu, D. W. Hogg, T. C. Beers, and Y. S. Lee. The Spatial Structure of Mono-abundance Sub-populations of the Milky Way Disk. *ApJ*, 753:148, July 2012b. doi: 10.1088/0004-637X/753/2/148.

A. Bressan, P. Marigo, L. Girardi, B. Salasnich, C. Dal Cero, S. Rubele, and A. Nanni. PARSEC: stellar tracks and isochrones with the PAdova and TRieste Stellar Evolution Code. *MNRAS*, 427:127–145, November 2012. doi: 10.1111/j.1365-2966.2012.21948.x.

C. B. Brook, D. Kawata, B. K. Gibson, and K. C. Freeman. The Emergence of the Thick Disk in a Cold Dark Matter Universe. *ApJ*, 612:894–899, September 2004. doi: 10.1086/422709.

C. B. Brook, D. Kawata, H. Martel, B. K. Gibson, and J. Bailin. Disk Evolution since z~1 in a CDM Universe. *ApJ*, 639:126–135, March 2006. doi: 10.1086/499154.

T. Brown, H. Ferguson, J. Gardner, L. Greggio, H. B. Hammel, A Renzini, M. Rich, Richer, H. M. Stiavell, and R. Wyse. Studying resolved stellar populations with the james webb space telescope. Technical report, Space Telescope Science Institute, 2008. URL `http://www.stsci.edu/jwst/doc-archive/white-papers/stellarPops_v4d.pdf`.

A. Burkert, J. W. Truran, and G. Hensler. The collapse of our Galaxy and the formation of the Galactic disk. *ApJ*, 391:651–658, June 1992. doi: 10.1086/171378.

D. Burstein. Structure and origin of S0 galaxies. III - The luminosity distribution perpendicular to the plane of the disks in S0's. *ApJ*, 234:829–836, December 1979. doi: 10.1086/157563.

M. D. Calapa, D. Calzetti, B. T. Draine, M. Boquien, C. Kramer, M. Xilouris, S. Verley, J. Braine, M. Relaño, P. van der Werf, F. Israel, I. Hermelo, and M. Albrecht. The Heating of Mid-infrared Dust in the Nearby Galaxy M33: A Testbed for Tracing Galaxy Evolution. *ApJ*, 784:130, April 2014. doi: 10.1088/0004-637X/784/2/130.

R. G. Carlberg, P. C. Dawson, T. Hsu, and D. A. Vandenberg. The age-velocity-dispersion relation in the solar neighborhood. *ApJ*, 294:674–681, July 1985. doi: 10.1086/163337.

E. Carretta and R. G. Gratton. Abundances for globular cluster giants. I. Homogeneous metallicities for 24 clusters. *A&AS*, 121:95–112, January 1997. doi: 10.1051/aas:1997116.

E. Carretta, A. Bragaglia, R. Gratton, V. D'Orazi, and S. Lucatello. Intrinsic iron spread and a new metallicity scale for globular clusters. *A&A*, 508:695–706, December 2009. doi: 10.1051/0004-6361/200913003.

E. Carretta, A. Bragaglia, R. G. Gratton, A. Recio-Blanco, S. Lucatello, V. D'Orazi, and S. Cassisi. Properties of stellar generations in globular clusters and relations with global parameters. *A&A*, 516:A55, June 2010. doi: 10.1051/0004-6361/200913451.

Bibliography

W. Cash. Parameter estimation in astronomy through application of the likelihood ratio. *ApJ*, 228:939–947, March 1979. doi: 10.1086/156922.

C. Chiappini, F. Matteucci, and R. Gratton. The Chemical Evolution of the Galaxy: The Two-Infall Model. *ApJ*, 477:765–+, March 1997. doi: 10.1086/303726.

S. Comerón, B. G. Elmegreen, J. H. Knapen, K. Sheth, J. L. Hinz, M. W. Regan, A. Gil de Paz, J.-C. Muñoz-Mateos, K. Menéndez-Delmestre, M. Seibert, T. Kim, T. Mizusawa, E. Laurikainen, H. Salo, J. Laine, E. Athanassoula, A. Bosma, R. J. Buta, D. A. Gadotti, L. C. Ho, B. Holwerda, E. Schinnerer, and D. Zaritsky. The Unusual Vertical Mass Distribution of NGC 4013 Seen through the Spitzer Survey of Stellar Structure in Galaxies (S^{4}G). *ApJ*, 738:L17, September 2011a. doi: 10.1088/2041-8205/738/2/L17.

S. Comerón, J. H. Knapen, K. Sheth, M. W. Regan, J. L. Hinz, A. Gil de Paz, K. Menéndez-Delmestre, J.-C. Muñoz-Mateos, M. Seibert, T. Kim, E. Athanassoula, A. Bosma, R. J. Buta, B. G. Elmegreen, L. C. Ho, B. W. Holwerda, E. Laurikainen, H. Salo, and E. Schinnerer. The Thick Disk in the Galaxy NGC 4244 from S^{4}G Imaging. *ApJ*, 729:18, March 2011b. doi: 10.1088/0004-637X/729/1/18.

G. S. Da Costa and T. E. Armandroff. Standard globular cluster giant branches in the $(M_I,(V-I)_0)$ plane. *AJ*, 100:162–181, July 1990. doi: 10.1086/115500.

J. J. Dalcanton and R. A. Bernstein. A Structural and Dynamical Study of Late-Type, Edge-on Galaxies. II. Vertical Color Gradients and the Detection of Ubiquitous Thick Disks. *AJ*, 124:1328–1359, September 2002. doi: 10.1086/342286.

J. J. Dalcanton, P. Yoachim, and R. A. Bernstein. The Formation of Dust Lanes: Implications for Galaxy Evolution. *ApJ*, 608:189–207, June 2004. doi: 10.1086/386358.

J. J. Dalcanton, B. F. Williams, A. C. Seth, A. Dolphin, J. Holtzman, K. Rosema, E. D. Skillman, A. Cole, L. Girardi, S. M. Gogarten, I. D. Karachentsev, K. Olsen, D. Weisz, C. Christensen, K. Freeman, K. Gilbert, C. Gallart, J. Harris, P. Hodge, R. S. de Jong, V. Karachentseva, M. Mateo, P. B. Stetson, M. Tavarez, D. Zaritsky, F. Governato, and T. Quinn. The ACS Nearby Galaxy Survey Treasury. *ApJS*, 183:67–108, July 2009. doi: 10.1088/0067-0049/183/1/67.

R. de Grijs and R. F. Peletier. The shape of galaxy disks: how the scale height increases with galactocentric distance. *A&A*, 320:L21–L24, April 1997.

R. de Grijs and P. C. van der Kruit. Structure analysis of edge-on spiral galaxies. *A&AS*, 117:19–37, May 1996.

R. de Grijs, R. F. Peletier, and P. C. van der Kruit. The z-structure of disk galaxies towards the galaxy planes. *A&A*, 327:966–982, November 1997.

J. T. A. de Jong, B. Yanny, H.-W. Rix, A. E. Dolphin, N. F. Martin, and T. C. Beers. Mapping the Stellar Structure of the Milky Way Thick Disk and Halo Using SEGUE Photometry. *ApJ*, 714:663–674, May 2010. doi: 10.1088/0004-637X/714/1/663.

R. S. de Jong. Near-infrared and optical broadband surface photometry of 86 face-on disk dominated galaxies. IV. Using color profiles to study stellar and dust content of galaxies. *A&A*, 313:377–395, September 1996.

R. S. de Jong. Point spread function tails and the measurements of diffuse stellar halo light around edge-on disc galaxies. *MNRAS*, 388:1521–1527, August 2008. doi: 10.1111/j.1365-2966.2008.13505.x.

R. S. de Jong, A. C. Seth, D. J. Radburn-Smith, E. F. Bell, T. M. Brown, J. S. Bullock, S. Courteau, J. J. Dalcanton, H. C. Ferguson, P. Goudfrooij, S. Holfeltz, B. W. Holwerda, C. Purcell, J. Sick, and D. B. Zucker. Stellar Populations across the NGC 4244 Truncated Galactic Disk. *ApJ*, 667:L49–L52, September 2007. doi: 10.1086/522035.

I. de Looze, M. Baes, G. J. Bendo, L. Ciesla, L. Cortese, G. de Geyter, B. Groves, M. Boquien, A. Boselli, L. Brondeel, A. Cooray, S. Eales, J. Fritz, F. Galliano, G. Gentile, K. D. Gordon, S. Hony, K.-H. Law, S. C. Madden, M. Sauvage, M. W. L. Smith, L. Spinoglio, and J. Verstappen. The dust energy balance in the edge-on spiral galaxy NGC 4565. *MNRAS*, 427:2797–2811, December 2012. doi: 10.1111/j.1365-2966.2012.22045.x.

G. de Vaucouleurs. General Physical Properties of External Galaxies. *Handbuch der Physik*, 53:311–+, 1959.

V. P. Debattista, L. Mayer, C. M. Carollo, B. Moore, J. Wadsley, and T. Quinn. The Secular Evolution of Disk Structural Parameters. *ApJ*, 645:209–227, July 2006. doi: 10.1086/504147.

A. Deep, G. Fiorentino, E. Tolstoy, E. Diolaiti, M. Bellazzini, P. Ciliegi, R. I. Davies, and J.-M. Conan. An E-ELT case study: colour-magnitude diagrams of an old galaxy in the Virgo cluster. *A&A*, 531:A151, July 2011. doi: 10.1051/0004-6361/201116603.

P. Demarque, C. R. King, and A. Diaz. The globular cluster metallicity scale - Evidence from stellar models. *ApJ*, 259:154–158, August 1982. doi: 10.1086/160155.

A. Dolphin. A new method to determine star formation histories of nearby galaxies. *New Astronomy*, 2:397–409, November 1997. doi: 10.1016/S1384-1076(97)00029-8.

A. E. Dolphin. WFPC2 Stellar Photometry with HSTPHOT. *PASP*, 112:1383–1396, October 2000. doi: 10.1086/316630.

A. E. Dolphin. Numerical methods of star formation history measurement and applications to seven dwarf spheroidals. *MNRAS*, 332:91–108, May 2002. doi: 10.1046/j.1365-8711.2002.05271.x.

M. A. Dopita and S. D. Ryder. On the law of star formation in disk galaxies. *ApJ*, 430:163–178, July 1994. doi: 10.1086/174390.

A. Dotter, B. Chaboyer, D. Jevremović, E. Baron, J. W. Ferguson, A. Sarajedini, and J. Anderson. The ACS Survey of Galactic Globular Clusters. II. Stellar Evolution Tracks, Isochrones, Luminosity Functions, and Synthetic Horizontal-Branch Models. *AJ*, 134:376–390, July 2007. doi: 10.1086/517915.

A. Dotter, A. Sarajedini, and J. Anderson. Globular Clusters in the Outer Galactic Halo: New Hubble Space Telescope/Advanced Camera for Surveys Imaging of Six Globular Clusters and the Galactic Globular Cluster Age-metallicity Relation. *ApJ*, 738:74, September 2011. doi: 10.1088/0004-637X/738/1/74.

Bibliography

R. Drimmel and D. N. Spergel. Three-dimensional Structure of the Milky Way Disk: The Distribution of Stars and Dust beyond 0.35 R$_{solar}$. *ApJ*, 556:181–202, July 2001. doi: 10.1086/321556.

B. Edvardsson, J. Andersen, B. Gustafsson, D. L. Lambert, P. E. Nissen, and J. Tomkin. The Chemical Evolution of the Galactic Disk - Part One - Analysis and Results. *A&A*, 275:101, August 1993.

O. J. Eggen, D. Lynden-Bell, and A. R. Sandage. Evidence from the motions of old stars that the Galaxy collapsed. *ApJ*, 136:748–+, November 1962. doi: 10.1086/147433.

B. G. Elmegreen and D. A. Hunter. Radial Profiles of Star Formation in the Far Outer Regions of Galaxy Disks. *ApJ*, 636:712–720, January 2006. doi: 10.1086/498082.

B. G. Elmegreen and C. Struck. Exponential Galaxy Disks from Stellar Scattering. *ApJ*, 775:L35, October 2013. doi: 10.1088/2041-8205/775/2/L35.

P. Erwin. Imfit: A Fast, Flexible New Program for Astronomical Image Fitting. *ArXiv e-prints*, August 2014.

S. M. Fall and G. Efstathiou. Formation and rotation of disc galaxies with haloes. *MNRAS*, 193:189–206, October 1980.

G. G. Fazio, J. L. Hora, L. E. Allen, M. L. N. Ashby, P. Barmby, L. K. Deutsch, J.-S. Huang, S. Kleiner, M. Marengo, S. T. Megeath, G. J. Melnick, M. A. Pahre, B. M. Patten, J. Polizotti, H. A. Smith, R. S. Taylor, Z. Wang, S. P. Willner, W. F. Hoffmann, J. L. Pipher, W. J. Forrest, C. W. McMurty, C. R. McCreight, M. E. McKelvey, R. E. McMurray, D. G. Koch, S. H. Moseley, R. G. Arendt, J. E. Mentzell, C. T. Marx, P. Losch, P. Mayman, W. Eichhorn, D. Krebs, M. Jhabvala, D. Y. Gezari, D. J. Fixsen, J. Flores, K. Shakoorzadeh, R. Jungo, C. Hakun, L. Workman, G. Karpati, R. Kichak, R. Whitley, S. Mann, E. V. Tollestrup, P. Eisenhardt, D. Stern, V. Gorjian, B. Bhattacharya, S. Carey, B. O. Nelson, W. J. Glaccum, M. Lacy, P. J. Lowrance, S. Laine, W. T. Reach, J. A. Stauffer, J. A. Surace, G. Wilson, E. L. Wright, A. Hoffman, G. Domingo, and M. Cohen. The Infrared Array Camera (IRAC) for the Spitzer Space Telescope. *ApJS*, 154:10–17, September 2004. doi: 10.1086/422843.

K. Foyle, S. Courteau, and R. J. Thacker. An N-body/SPH study of isolated galaxy mass density profiles. *MNRAS*, 386:1821–1844, June 2008. doi: 10.1111/j.1365-2966.2008. 13201.x.

K. C. Freeman. On the Disks of Spiral and S0 Galaxies. *ApJ*, 160:811–+, June 1970. doi: 10.1086/150474.

K. Fuhrmann. Nearby stars of the Galactic disc and halo - IV. *MNRAS*, 384:173–224, February 2008. doi: 10.1111/j.1365-2966.2007.12671.x.

G. Gilmore and N. Reid. New light on faint stars. III - Galactic structure towards the South Pole and the Galactic thick disc. *MNRAS*, 202:1025–1047, March 1983.

T. M. Girard, V. I. Korchagin, D. I. Casetti-Dinescu, W. F. van Altena, C. E. López, and D. G. Monet. Velocity Shear of the Thick Disk from SPM3 Proper Motions at the South Galactic Pole. *AJ*, 132:1768–1782, November 2006. doi: 10.1086/507331.

L. Girardi, B. F. Williams, K. M. Gilbert, P. Rosenfield, J. J. Dalcanton, P. Marigo, M. L. Boyer, A. Dolphin, D. R. Weisz, J. Melbourne, K. A. G. Olsen, A. C. Seth, and E. Skillman. The ACS Nearby Galaxy Survey Treasury. IX. Constraining Asymptotic Giant Branch Evolution with Old Metal-poor Galaxies. *ApJ*, 724:1030–1043, December 2010. doi: 10.1088/0004-637X/724/2/1030.

O. Y. Gnedin. Dynamical Evolution of Galaxies in Clusters. *ApJ*, 589:752–769, June 2003. doi: 10.1086/374774.

L. Greggio, R. Falomo, S. Zaggia, D. Fantinel, and M. Uslenghi. Resolved Stellar Population of Distant Galaxies in the ELT Era. *PASP*, 124:653–667, July 2012. doi: 10.1086/667195.

M. Gullieuszik, E. V. Held, L. Rizzi, I. Saviane, Y. Momany, and S. Ortolani. Near-infrared observations of the Fornax dwarf galaxy. I. The red giant branch. *A&A*, 467:1025–1036, June 2007. doi: 10.1051/0004-6361:20066788.

M. Haas, U. Klaas, and S. Bianchi. The relation of PAH strength with cold dust in galaxies. *A&A*, 385:L23–L26, April 2002. doi: 10.1051/0004-6361:20020222.

J. Hänninen and C. Flynn. Simulations of the heating of the Galactic stellar disc. *MNRAS*, 337:731–742, December 2002. doi: 10.1046/j.1365-8711.2002.05956.x.

W. E. Harris. A Catalog of Parameters for Globular Clusters in the Milky Way. *AJ*, 112: 1487–+, October 1996. doi: 10.1086/118116.

W. E. Harris. A New Catalog of Globular Clusters in the Milky Way. *ArXiv e-prints*, 1012: 3224–+, December 2010.

F. D. A. Hartwick. A Two-Dimensional Classification for Galactic Globular Clusters. *ApJ*, 154:475, November 1968. doi: 10.1086/149775.

E. V. Held, M. Gullieuszik, L. Rizzi, L. Girardi, P. Marigo, and I. Saviane. A near-infrared study of AGB and red giant stars in the Leo I dSph galaxy. *MNRAS*, 404:1475–1489, May 2010. doi: 10.1111/j.1365-2966.2010.16358.x.

E. Hertzsprung. Zur Stralung Der Strerne. *Zeitschrift Fur Wissenschaftliche Photographie, Vol 3, p. 442-449*, 3:442–449, July 1905.

J. L. Hinz, C. Y. Peng, and S4G Team. MultiGALFIT: Automated Decomposition of Galaxy Images for S4G. In *American Astronomical Society Meeting Abstracts #221*, volume 221 of *American Astronomical Society Meeting Abstracts*, page 230.05, January 2013.

B. W. Holwerda, R. S. de Jong, M. Regan, A. Seth, J. D. Dalcanton, E. Bell, and S. Bianchi. Spitzer's View on Edge-On Spiral Disks. In *American Astronomical Society Meeting Abstracts*, volume 38 of *Bulletin of the American Astronomical Society*, page 924, December 2006.

B. W. Holwerda, S. Bianchi, T. Böker, D. Radburn-Smith, R. S. de Jong, M. Baes, P. C. van der Kruit, M. Xilouris, K. D. Gordon, and J. J. Dalcanton. Herschel/SPIRE observations of the dusty disk of NGC 4244. *A&A*, 541:L5, May 2012. doi: 10.1051/0004-6361/201118615.

F. Hoyle and M. Schwarzschild. On the Evolution of Type II Stars. *ApJS*, 2:1–+, June 1955. doi: 10.1086/190015.

Bibliography

R. Ibata, M. Mouhcine, and M. Rejkuba. An HST/ACS investigation of the spatial and chemical structure and sub-structure of NGC 891, a Milky Way analogue. *MNRAS*, 395: 126–143, May 2009. doi: 10.1111/j.1365-2966.2009.14536.x.

A. G. Jones, G. J. Bendo, M. Baes, M. Boquien, A. Boselli, I. De Looze, J. Fritz, F. Galliano, T. M. Hughes, V. Lebouteiller, N. Lu, S. C. Madden, A. Rémy-Ruyer, M. W. L. Smith, L. Spinoglio, and A. A. Zijlstra. The relationship between polycyclic aromatic hydrocarbon emission and far-infrared dust emission from NGC 2403 and M83. *MNRAS*, 448:168–187, March 2015. doi: 10.1093/mnras/stu2715.

M. Jurić, Ž. Ivezić, A. Brooks, R. H. Lupton, D. Schlegel, D. Finkbeiner, N. Padmanabhan, N. Bond, B. Sesar, C. M. Rockosi, G. R. Knapp, J. E. Gunn, T. Sumi, D. P. Schneider, J. C. Barentine, H. J. Brewington, J. Brinkmann, M. Fukugita, M. Harvanek, S. J. Kleinman, J. Krzesinski, D. Long, E. H. Neilsen, Jr., A. Nitta, S. A. Snedden, and D. G. York. The Milky Way Tomography with SDSS. I. Stellar Number Density Distribution. *ApJ*, 673:864–914, February 2008. doi: 10.1086/523619.

A. J. Kalnajs. Pattern Speeds of Density Waves. In B. Sundelius, editor, *Dynamics of Disc Galaxies*, page 323, 1991.

S. A. Kassin, B. J. Weiner, S. M. Faber, J. P. Gardner, C. N. A. Willmer, A. L. Coil, M. C. Cooper, J. Devriendt, A. A. Dutton, P. Guhathakurta, D. C. Koo, A. J. Metevier, K. G. Noeske, and J. R. Primack. The Epoch of Disk Settling: z ~ 1 to Now. *ApJ*, 758:106, October 2012. doi: 10.1088/0004-637X/758/2/106.

S. Kazantzidis, J. S. Bullock, A. R. Zentner, A. V. Kravtsov, and L. A. Moustakas. Cold Dark Matter Substructure and Galactic Disks. I. Morphological Signatures of Hierarchical Satellite Accretion. *ApJ*, 688:254–276, November 2008. doi: 10.1086/591958.

R. C. Kennicutt, Jr. The star formation law in galactic disks. *ApJ*, 344:685–703, September 1989. doi: 10.1086/167834.

R. C. Kennicutt, Jr., L. Armus, G. Bendo, D. Calzetti, D. A. Dale, B. T. Draine, C. W. Engelbracht, K. D. Gordon, A. D. Grauer, G. Helou, D. J. Hollenbach, T. H. Jarrett, L. J. Kewley, C. Leitherer, A. Li, S. Malhotra, M. W. Regan, G. H. Rieke, M. J. Rieke, H. Roussel, J.-D. T. Smith, M. D. Thornley, and F. Walter. SINGS: The SIRTF Nearby Galaxies Survey. *PASP*, 115:928–952, August 2003. doi: 10.1086/376941.

V. V. Koval', V. A. Marsakov, and T. V. Borkova. Relationship between the velocity ellipsoids of galactic-disk stars and their ages and metallicities. *Astronomy Reports*, 53: 785–800, September 2009. doi: 10.1134/S1063772909090029.

M. Kregel, P. C. van der Kruit, and K. C. Freeman. Structure and kinematics of edge-on galaxy discs - I. Observations of the stellar kinematics. *MNRAS*, 351:1247–1265, July 2004. doi: 10.1111/j.1365-2966.2004.07864.x.

P. Kroupa. Thickening of galactic discs through clustered star formation. *MNRAS*, 330: 707–718, March 2002. doi: 10.1046/j.1365-8711.2002.05128.x.

R.-P. Kudritzki, M. A. Urbaneja, Z. Gazak, F. Bresolin, N. Przybilla, W. Gieren, and G. Pietrzyński. Quantitative Spectroscopy of Blue Supergiant Stars in the Disk of M81: Metallicity, Metallicity Gradient, and Distance. *ApJ*, 747:15, March 2012. doi: 10.1088/0004-637X/747/1/15.

C. G. Lacey and J. P. Ostriker. Massive black holes in galactic halos? *ApJ*, 299:633–652, December 1985. doi: 10.1086/163729.

J. A. Larsen and R. M. Humphreys. Fitting a Galactic Model to an All-Sky Survey. *AJ*, 125:1958–1979, April 2003. doi: 10.1086/368364.

R. B. Larson. Models for the formation of disc galaxies. *MNRAS*, 176:31–52, July 1976.

M. G. Lee, W. L. Freedman, and B. F. Madore. The Tip of the Red Giant Branch as a Distance Indicator for Resolved Galaxies. *ApJ*, 417:553–+, November 1993. doi: 10.1086/173334.

T. Lejeune and R. Buser. Modeling age and metallicity in globular clusters: a comparison of theoretical giant branch isochrones. In I. Hubeny, S. Heap, and R. Cornett, editors, *Spectrophotometric Dating of Stars and Galaxies*, volume 192 of *Astronomical Society of the Pacific Conference Series*, page 211, 1999.

D. N. C. Lin and J. E. Pringle. The formation of the exponential disk in spiral galaxies. *ApJ*, 320:L87–L91, September 1987. doi: 10.1086/184981.

S. R. Loebman, R. Roškar, V. P. Debattista, Ž. Ivezić, T. R. Quinn, and J. Wadsley. The Genesis of the Milky Way's Thick Disk Via Stellar Migration. *ApJ*, 737:8, August 2011. doi: 10.1088/0004-637X/737/1/8.

L. A. MacArthur, J. J. González, and S. Courteau. Stellar population and kinematic profiles in spiral bulges and discs: population synthesis of integrated spectra. *MNRAS*, 395:28–63, May 2009. doi: 10.1111/j.1365-2966.2009.14519.x.

P. Marigo, L. Girardi, A. Bressan, M. A. T. Groenewegen, L. Silva, and G. L. Granato. Evolution of asymptotic giant branch stars. II. Optical to far-infrared isochrones with improved TP-AGB models. *A&A*, 482:883–905, May 2008. doi: 10.1051/0004-6361:20078467.

A. Marín-Franch, A. Aparicio, G. Piotto, A. Rosenberg, B. Chaboyer, A. Sarajedini, M. Siegel, J. Anderson, L. R. Bedin, A. Dotter, M. Hempel, I. King, S. Majewski, A. P. Milone, N. Paust, and I. N. Reid. The ACS Survey of Galactic Globular Clusters. VII. Relative Ages. *ApJ*, 694:1498–1516, April 2009. doi: 10.1088/0004-637X/694/2/1498.

V. A. Marsakov, V. V. Koval', T. V. Borkova, and M. V. Shapovalov. The age-metallicity relation in the thin disk of the galaxy. *Astronomy Reports*, 55:667–682, August 2011. doi: 10.1134/S1063772911080063.

M. Martig, I. Minchev, and C. Flynn. Dissecting simulated disc galaxies - I. The structure of mono-age populations. *MNRAS*, 442:2474–2486, August 2014a. doi: 10.1093/mnras/stu1003.

M. Martig, I. Minchev, and C. Flynn. Dissecting simulated disc galaxies - II. The age-velocity relation. *MNRAS*, 443:2452–2462, September 2014b. doi: 10.1093/mnras/stu1322.

T. P. K. Martinsson, M. A. W. Verheijen, K. B. Westfall, M. A. Bershady, A. Schechtman-Rook, D. R. Andersen, and R. A. Swaters. The DiskMass Survey. VI. Gas and stellar kinematics in spiral galaxies from PPak integral-field spectroscopy. *A&A*, 557:A130, September 2013. doi: 10.1051/0004-6361/201220515.

Bibliography

F. Matteucci and P. Francois. Galactic chemical evolution - Abundance gradients of individual elements. *MNRAS*, 239:885–904, August 1989.

S. E. Meidt, E. Schinnerer, J. H. Knapen, A. Bosma, E. Athanassoula, K. Sheth, R. J. Buta, D. Zaritsky, E. Laurikainen, D. Elmegreen, B. G. Elmegreen, D. A. Gadotti, H. Salo, M. Regan, L. C. Ho, B. F. Madore, J. L. Hinz, R. A. Skibba, A. Gil de Paz, J.-C. Muñoz-Mateos, K. Menéndez-Delmestre, M. Seibert, T. Kim, T. Mizusawa, J. Laine, and S. Comerón. Reconstructing the Stellar Mass Distributions of Galaxies Using S^{4}G IRAC 3.6 and 4.5 μm Images. I. Correcting for Contamination by Polycyclic Aromatic Hydrocarbons, Hot Dust, and Intermediate-age Stars. *ApJ*, 744:17, January 2012. doi: 10.1088/0004-637X/744/1/17.

G. R. Meurer, D. J. Hanish, H. C. Ferguson, P. M. Knezek, V. A. Kilborn, M. E. Putman, R. C. Smith, B. Koribalski, M. Meyer, M. S. Oey, E. V. Ryan-Weber, M. A. Zwaan, T. M. Heckman, R. C. Kennicutt, Jr., J. C. Lee, R. L. Webster, J. Bland-Hawthorn, M. A. Dopita, K. C. Freeman, M. T. Doyle, M. J. Drinkwater, L. Staveley-Smith, and J. Werk. The Survey for Ionization in Neutral Gas Galaxies. I. Description and Initial Results. *ApJS*, 165:307–337, July 2006. doi: 10.1086/504685.

I. Minchev, B. Famaey, A. C. Quillen, W. Dehnen, M. Martig, and A. Siebert. Radial migration does little for Galactic disc thickening. *A&A*, 548:A127, December 2012a. doi: 10.1051/0004-6361/201219714.

I. Minchev, B. Famaey, A. C. Quillen, P. Di Matteo, F. Combes, M. Vlajić, P. Erwin, and J. Bland-Hawthorn. Evolution of galactic discs: multiple patterns, radial migration, and disc outskirts. *A&A*, 548:A126, December 2012b. doi: 10.1051/0004-6361/201219198.

I. Minchev, C. Chiappini, and M. Martig. Chemodynamical evolution of the Milky Way disk. II. Variations with Galactic radius and height above the disk plane. *A&A*, 572:A92, December 2014. doi: 10.1051/0004-6361/201423487.

A. Misiriotis, E. M. Xilouris, J. Papamastorakis, P. Boumis, and C. D. Goudis. The distribution of the ISM in the Milky Way. A three-dimensional large-scale model. *A&A*, 459: 113–123, November 2006. doi: 10.1051/0004-6361:20054618.

H. J. Mo, S. Mao, and S. D. M. White. The formation of galactic discs. *MNRAS*, 295: 319–336, April 1998. doi: 10.1046/j.1365-8711.1998.01227.x.

Y. Momany, E. V. Held, I. Saviane, L. R. Bedin, M. Gullieuszik, M. Clemens, L. Rizzi, M. R. Rich, and K. Kuijken. HST/ACS observations of the old and metal-poor Sagittarius dwarf irregular galaxy. *A&A*, 439:111–127, August 2005. doi: 10.1051/0004-6361:20052747.

H. L. Morrison, E. D. Miller, P. Harding, D. R. Stinebring, and T. A. Boroson. Stellar Populations in Edge-On Galaxies From Deep CCD Surface Photometry.II. One-Dimensional FITS of NGC 891. *AJ*, 113:2061–2074, June 1997. doi: 10.1086/118418.

J. C. Muñoz-Mateos, A. Gil de Paz, S. Boissier, J. Zamorano, T. Jarrett, J. Gallego, and B. F. Madore. Specific Star Formation Rate Profiles in Nearby Spiral Galaxies: Quantifying the Inside-Out Formation of Disks. *ApJ*, 658:1006–1026, April 2007. doi: 10.1086/511812.

T. Naab and J. P. Ostriker. A simple model for the evolution of disc galaxies: the Milky Way. *MNRAS*, 366:899–917, March 2006. doi: 10.1111/j.1365-2966.2005.09807.x.

N. Neininger, M. Guelin, S. Garcia-Burillo, R. Zylka, and R. Wielebinski. Cold dust and molecular line emission in NGC4565. *A&A*, 310:725–736, June 1996.

P. E. Nissen. Age and Metallicity Distributions among Galactic Disk Stars. In P. C. van der Kruit & G. Gilmore, editor, *Stellar Populations*, volume 164 of *IAU Symposium*, pages 109–+, 1995.

B. Nordström, M. Mayor, J. Andersen, J. Holmberg, F. Pont, B. R. Jørgensen, E. H. Olsen, S. Udry, and N. Mowlavi. The Geneva-Copenhagen survey of the Solar neighbourhood. Ages, metallicities, and kinematic properties of $\approx$14 000 F and G dwarfs. *A&A*, 418: 989–1019, May 2004. doi: 10.1051/0004-6361:20035959.

P. Ocvirk, R. Peletier, and A. Lançon. Extragalactic archeology in integrated light: A test case with NGC 4030. *Astronomische Nachrichten*, 329:980, December 2008. doi: 10.1002/asna.200811075.

J. H. Oort. The force exerted by the stellar system in the direction perpendicular to the galactic plane and some related problems. *Bull. Astron. Inst. Netherlands*, 6:249, August 1932.

M. A. Pahre, M. L. N. Ashby, G. G. Fazio, and S. P. Willner. Spatial Distribution of Warm Dust in Early-Type Galaxies. *ApJS*, 154:229–234, September 2004. doi: 10.1086/423320.

S. G. Patel, P. G. van Dokkum, M. Franx, R. F. Quadri, A. Muzzin, D. Marchesini, R. J. Williams, B. P. Holden, and M. Stefanon. HST/WFC3 Confirmation of the Inside-out Growth of Massive Galaxies at $0 < z < 2$ and Identification of Their Star-forming Progenitors at $z \approx 3$. *ApJ*, 766:15, March 2013. doi: 10.1088/0004-637X/766/1/15.

F. S. Patterson. The Luminosity Gradient of Messier 33. *Harvard College Observatory Bulletin*, 914:9–10, December 1940.

G. Paturel, C. Petit, P. Prugniel, G. Theureau, J. Rousseau, M. Brouty, P. Dubois, and L. Cambrésy. HYPERLEDA. I. Identification and designation of galaxies. *A&A*, 412: 45–55, December 2003. doi: 10.1051/0004-6361:20031411.

R. F. Peletier and J. H. Knapen. Looking through the dust - the edge-on galaxy NGC 7814 in the near-infrared. *The Messenger*, 70:57–61, December 1992.

I. Pérez. Truncation of stellar disks in galaxies at $z \approx 1$. *A&A*, 427:L17–L20, December 2004. doi: 10.1051/0004-6361:200400090.

S. P. C. Peters, P. C. van der Kruit, R. J. Allen, and K. C. Freeman. The Shape of Dark Matter Halos in Edge-on Galaxies: I. Overview of HI observations. *ArXiv e-prints*, March 2013.

A. Pietrinferni, S. Cassisi, M. Salaris, and F. Castelli. A Large Stellar Evolution Database for Population Synthesis Studies. I. Scaled Solar Models and Isochrones. *ApJ*, 612:168–190, September 2004. doi: 10.1086/422498.

A. Pietrinferni, S. Cassisi, M. Salaris, and F. Castelli. A Large Stellar Evolution Database for Population Synthesis Studies. II. Stellar Models and Isochrones for an α-enhanced Metal Distribution. *ApJ*, 642:797–812, May 2006. doi: 10.1086/501344.

Bibliography

M. Pohlen and I. Trujillo. The structure of galactic disks. Studying late-type spiral galaxies using SDSS. *A&A*, 454:759–772, August 2006. doi: 10.1051/0004-6361:20064883.

M. Pohlen, M. Balcells, R. Lütticke, and R.-J. Dettmar. Thick disks of lenticular galaxies. 3D-photometric thin/thick disk decomposition of eight edge-on s0 galaxies. *A&A*, 422: 465–475, August 2004. doi: 10.1051/0004-6361:20035932.

M. Pohlen, S. Zaroubi, R. F. Peletier, and R.-J. Dettmar. On the three-dimensional structure of edge-on disc galaxies. *MNRAS*, 378:594–616, June 2007. doi: 10.1111/j.1365-2966.2007. 11790.x.

N. Prantzos and S. Boissier. Chemo-spectrophotometric evolution of spiral galaxies - III. Abundance and colour gradients in discs. *MNRAS*, 313:338–346, April 2000. doi: 10. 1046/j.1365-8711.2000.03228.x.

W. H. Press and P. Schechter. Formation of Galaxies and Clusters of Galaxies by Self-Similar Gravitational Condensation. *ApJ*, 187:425–438, February 1974. doi: 10.1086/152650.

A. C. Quillen and D. R. Garnett. The Saturation of Disk Heating in the Solar Neighborhood and Evidence for a Merger 9 Gyr Ago. In J. G. Funes and E. M. Corsini, editors, *Galaxy Disks and Disk Galaxies*, volume 230 of *Astronomical Society of the Pacific Conference Series*, pages 87–88, 2001.

P. J. Quinn, L. Hernquist, and D. P. Fullagar. Heating of galactic disks by mergers. *ApJ*, 403:74–93, January 1993. doi: 10.1086/172184.

D. J. Radburn-Smith, R. S. de Jong, A. C. Seth, J. Bailin, E. F. Bell, T. M. Brown, J. S. Bullock, S. Courteau, J. J. Dalcanton, H. C. Ferguson, P. Goudfrooij, S. Holfeltz, B. W. Holwerda, C. Purcell, J. Sick, D. Streich, M. Vlajic, and D. B. Zucker. The GHOSTS Survey. I. Hubble Space Telescope Advanced Camera for Surveys Data. *ApJS*, 195:18, August 2011. doi: 10.1088/0067-0049/195/2/18.

D. J. Radburn-Smith, R. Roškar, V. P. Debattista, J. J. Dalcanton, D. Streich, R. S. de Jong, M. Vlajić, B. W. Holwerda, C. W. Purcell, A. E. Dolphin, and D. B. Zucker. Outer-disk Populations in NGC 7793: Evidence for Stellar Radial Migration. *ApJ*, 753:138, July 2012. doi: 10.1088/0004-637X/753/2/138.

D. J. Radburn-Smith, R. S. de Jong, D. Streich, E. F. Bell, J. J. Dalcanton, A. E. Dolphin, A. M. Stilp, A. Monachesi, B. W. Holwerda, and J. Bailin. Constraining the Age of the NGC 4565 H I Disk Warp: Determining the Origin of Gas Warps. *ApJ*, 780:105, January 2014. doi: 10.1088/0004-637X/780/1/105.

M. W. Regan. Pipeline 1 of S4G. In *American Astronomical Society Meeting Abstracts #221*, volume 221 of *American Astronomical Society Meeting Abstracts*, page 230.02, January 2013.

W. Rice, K. M. Merrill, I. Gatley, and F. C. Gillett. Near-Infrared Structure of the Edge-on Spiral NGC 4565. *AJ*, 112:114, July 1996. doi: 10.1086/117993.

J. C. Richardson, A. M. N. Ferguson, A. D. Mackey, M. J. Irwin, S. C. Chapman, A. Huxor, R. A. Ibata, G. F. Lewis, and N. R. Tanvir. An HST/ACS view of the inhomogeneous outer halo of M31. *MNRAS*, 396:1842–1850, July 2009. doi: 10.1111/j.1365-2966.2009.14788.x.

A. C. Robin, M. Haywood, M. Creze, D. K. Ojha, and O. Bienayme. The thick disc of the Galaxy: sequel of a merging event. *A&A*, 305:125–+, January 1996.

H. J. Rocha-Pinto, W. J. Maciel, J. Scalo, and C. Flynn. Chemical enrichment and star formation in the Milky Way disk. I. Sample description and chromospheric age-metallicity relation. *A&A*, 358:850–868, June 2000.

R. Roškar, V. P. Debattista, G. S. Stinson, T. R. Quinn, T. Kaufmann, and J. Wadsley. Beyond Inside-Out Growth: Formation and Evolution of Disk Outskirts. *ApJ*, 675:L65–L68, March 2008. doi: 10.1086/586734.

H. N. Russell. Relations Between the Spectra and Other Characteristics of the Stars. *Popular Astronomy*, 22:275–294, May 1914.

G. A. Rutledge, J. E. Hesser, and P. B. Stetson. Galactic Globular Cluster Metallicity Scale from the Ca II Triplet II. Rankings, Comparisons, and Puzzles. *PASP*, 109:907–919, August 1997. doi: 10.1086/133959.

M. Salaris, A. Chieffi, and O. Straniero. The alpha-enhanced isochrones and their impact on the FITS to the Galactic globular cluster system. *ApJ*, 414:580–600, September 1993. doi: 10.1086/173105.

H. Salo, E. Laurikainen, J. Laine, S. Comerón, D. Gadotti, K. Sheth, and S4G Team. Multi-Component Decompositions for S4G Galaxies. In *American Astronomical Society Meeting Abstracts #221*, volume 221 of *American Astronomical Society Meeting Abstracts*, page 230.04, January 2013.

P. Sánchez-Blázquez, S. Courty, B. K. Gibson, and C. B. Brook. The origin of the light distribution in spiral galaxies. *MNRAS*, 398:591–606, September 2009. doi: 10.1111/j. 1365-2966.2009.15133.x.

A. Sandage and L. L. Smith. The color-magnitude diagram of the metal-rich globular cluster NGC 6712. *ApJ*, 144:886–+, June 1966. doi: 10.1086/148686.

C. Sandin. The influence of diffuse scattered light. I. The PSF and its role in observations of the edge-on galaxy NGC 5907. *A&A*, 567:A97, July 2014. doi: 10.1051/0004-6361/ 201423429.

C. Sandin. The influence of diffuse scattered light II. Observations of galaxy haloes and thick discs and hosts of BCGs. *ArXiv e-prints*, February 2015.

A. Sarajedini, L. R. Bedin, B. Chaboyer, A. Dotter, M. Siegel, J. Anderson, A. Aparicio, I. King, S. Majewski, A. Marín-Franch, G. Piotto, I. N. Reid, and A. Rosenberg. The ACS Survey of Galactic Globular Clusters. I. Overview and Clusters without Previous Hubble Space Telescope Photometry. *AJ*, 133:1658–1672, April 2007. doi: 10.1086/511979.

I. Saviane, A. Rosenberg, G. Piotto, and A. Aparicio. The red giant branches of Galactic globular clusters in the $[(V-I)_0, M_V]$ plane: metallicity indices and morphology. *A&A*, 355:966–978, March 2000.

J. Schaye. Star Formation Thresholds and Galaxy Edges: Why and Where. *ApJ*, 609: 667–682, July 2004. doi: 10.1086/421232.

Bibliography

A. Schechtman-Rook, M. A. Bershady, and K. Wood. The Three-dimensional Distribution of Dust in NGC 891. *ApJ*, 746:70, February 2012. doi: 10.1088/0004-637X/746/1/70.

M. Schmidt. The Rate of Star Formation. II. The Rate of Formation of Stars of Different Mass. *ApJ*, 137:758, April 1963. doi: 10.1086/147553.

R. Schönrich and J. Binney. Chemical evolution with radial mixing. *MNRAS*, 396:203–222, June 2009. doi: 10.1111/j.1365-2966.2009.14750.x.

J. Schulz, U. Fritze-v. Alvensleben, and K. J. Fricke. Wavelength and redshift dependence of bulge/total light ratios in galaxies. *A&A*, 398:89–100, January 2003. doi: 10.1051/0004-6361:20021631.

G. M. Seabroke and G. Gilmore. Revisiting the relations: Galactic thin disc age-velocity dispersion relation. *MNRAS*, 380:1348–1368, October 2007. doi: 10.1111/j.1365-2966.2007.12210.x.

L. Searle and R. Zinn. Compositions of halo clusters and the formation of the galactic halo. *ApJ*, 225:357–379, October 1978. doi: 10.1086/156499.

J. A. Sellwood and J. J. Binney. Radial mixing in galactic discs. *MNRAS*, 336:785–796, November 2002. doi: 10.1046/j.1365-8711.2002.05806.x.

K.-i. Seon, A. N. Witt, J.-h. Shinn, and I.-j. Kim. Diffuse Extraplanar Dust in NGC 891. *ApJ*, 785:L18, April 2014. doi: 10.1088/2041-8205/785/1/L18.

A. C. Seth, J. J. Dalcanton, and R. S. de Jong. A Study of Edge-On Galaxies with the Hubble Space Telescope Advanced Camera for Surveys. I. Initial Results. *AJ*, 129:1331–1349, March 2005a. doi: 10.1086/427859.

A. C. Seth, J. J. Dalcanton, and R. S. de Jong. A Study of Edge-On Galaxies with the Hubble Space Telescope Advanced Camera for Surveys. II. Vertical Distribution of the Resolved Stellar Population. *AJ*, 130:1574–1592, October 2005b. doi: 10.1086/444620.

H. Shapley and H. D. Curtis. The Scale of the Universe. *Bulletin of the National Research Council, Vol. 2, Part 3, No. 11, p. 171-217*, 2:171–217, May 1921.

M. A. Shaw and G. Gilmore. The luminosity distributions of edge-on spiral and lenticular galaxies. II - Modelling the non-thin disc light in a sample of ten galaxies. *MNRAS*, 242: 59–73, January 1990.

K. Sheth, M. Regan, J. L. Hinz, A. Gil de Paz, K. Menéndez-Delmestre, J.-C. Muñoz-Mateos, M. Seibert, T. Kim, E. Laurikainen, H. Salo, D. A. Gadotti, J. Laine, T. Mizusawa, L. Armus, E. Athanassoula, A. Bosma, R. J. Buta, P. Capak, T. H. Jarrett, D. M. Elmegreen, B. G. Elmegreen, J. H. Knapen, J. Koda, G. Helou, L. C. Ho, B. F. Madore, K. L. Masters, B. Mobasher, P. Ogle, C. Y. Peng, E. Schinnerer, J. A. Surace, D. Zaritsky, S. Comerón, B. de Swardt, S. E. Meidt, M. Kasliwal, and M. Aravena. The Spitzer Survey of Stellar Structure in Galaxies (S^{4}G). *PASP*, 122:1397–1414, December 2010. doi: 10.1086/657638.

M. Sirianni, M. J. Jee, N. Benítez, J. P. Blakeslee, A. R. Martel, G. Meurer, M. Clampin, G. De Marchi, H. C. Ford, R. Gilliland, G. F. Hartig, G. D. Illingworth, J. Mack, and W. J. McCann. The Photometric Performance and Calibration of the Hubble Space

Telescope Advanced Camera for Surveys. *PASP*, 117:1049–1112, October 2005. doi: 10.1086/444553.

C. Soubiran, O. Bienaymé, T. V. Mishenina, and V. V. Kovtyukh. Vertical distribution of Galactic disk stars. IV. AMR and AVR from clump giants. *A&A*, 480:91–101, March 2008. doi: 10.1051/0004-6361:20078788.

L. Spitzer, Jr. and M. Schwarzschild. The Possible Influence of Interstellar Clouds on Stellar Velocities. *ApJ*, 114:385, November 1951. doi: 10.1086/145478.

Spitzer IRAC Instrument and Instrument Support Teams. *IRAC Instrument Handbook.* Spitzer Science Center, California Institute of Technology, Pasadena, California USA, 2.0.3 edition, February 2013. URL `http://irsa.ipac.caltech.edu/data/SPITZER/docs/irac/iracinstrumenthandbook/`.

Spitzer Post-BCD Tools Team and Science User Support Team. *MOPEX User's Guide.* Spitzer Science Center, California Institute of Technology, Pasadena, California USA, 18.5.0 edition, March 2012. URL `http://ssc.spitzer.caltech.edu/`. March.

Spitzer Software Team. *Leopard User's Guide.* Spitzer Science Center, California Institute of Technology, Pasadena, California USA, version 9 edition, January 2008. URL `http://ssc.spitzer.caltech.edu/`.

T. S. Statler. Orbital decay in aspherical galaxies. I - Oblate systems. *ApJ*, 331:71–101, August 1988. doi: 10.1086/166539.

G. S. Stinson, J. Bovy, H.-W. Rix, C. Brook, R. Roškar, J. J. Dalcanton, A. V. Macciò, J. Wadsley, H. M. P. Couchman, and T. R. Quinn. MaGICC thick disc - I. Comparing a simulated disc formed with stellar feedback to the Milky Way. *MNRAS*, 436:625–634, November 2013. doi: 10.1093/mnras/stt1600.

D. Streich, R. S. de Jong, J. Bailin, P. Goudfrooij, D. Radburn-Smith, and M. Vlajic. On the relation between metallicity and RGB color in HST/ACS data. *A&A*, 563:A5, March 2014. doi: 10.1051/0004-6361/201220956.

M. Tanaka, M. Chiba, Y. Komiyama, P. Guhathakurta, J. S. Kalirai, and M. Iye. Structure and Population of the Andromeda Stellar Halo from a Subaru/Suprime-Cam Survey. *ApJ*, 708:1168–1203, January 2010. doi: 10.1088/0004-637X/708/2/1168.

G. P. Tiede, A. Sarajedini, and M. K. Barker. The Stellar Populations in the Outer Regions of M33. I. Metallicity Distribution Function. *AJ*, 128:224–236, July 2004. doi: 10.1086/421369.

N. A. Tikhonov and O. A. Galazutdinova. Stellar Disks and Halos of Edge-on Spiral Galaxies: NGC 891, NGC 4144, and NGC 4244. *Astrophysics*, 48:221–236, April 2005. doi: 10.1007/s10511-005-0021-8.

N. A. Tikhonov and O. A. Galazutdinova. Stellar subsystems of edge-on disk galaxies. *Astronomical and Astrophysical Transactions*, 27:227–232, 2012a.

N. A. Tikhonov and O. A. Galazutdinova. Stellar subsystems of different ages in spiral and irregular galaxies. *Astronomy Letters*, 38:147–156, March 2012b. doi: 10.1134/S1063773712030061.

Bibliography

N. A. Tikhonov, O. A. Galazutdinova, and I. O. Drozdovsky. Stellar halos and thick disks around edge-on spiral galaxies IC2233, IC5052, NGC4631 and NGC5023. *ArXiv Astrophysics e-prints*, March 2006.

G. Toth and J. P. Ostriker. Galactic disks, infall, and the global value of Omega. *ApJ*, 389: 5–26, April 1992. doi: 10.1086/171185.

I. Trujillo and M. Pohlen. Stellar Disk Truncations at High z: Probing Inside-Out Galaxy Formation. *ApJ*, 630:L17–L20, September 2005. doi: 10.1086/491472.

V. Tsikoudi. Photometry and structure of lenticular galaxies. I - NGC 3115. *ApJ*, 234: 842–853, December 1979. doi: 10.1086/157565.

E. Valenti, F. R. Ferraro, and L. Origlia. Red giant branch in near-infrared colour-magnitude diagrams - I. Calibration of photometric indices. *MNRAS*, 351:1204–1214, July 2004. doi: 10.1111/j.1365-2966.2004.07861.x.

P. C. van der Kruit. Optical surface photometry of eight spiral galaxies studied in Westerbork. *A&AS*, 38:15–38, October 1979.

P. C. van der Kruit. The radial distribution of surface brightness in galactic disks. *A&A*, 173:59–80, February 1987.

P. C. van der Kruit. The three-dimensional distribution of light and mass in disks of spiral galaxies. *A&A*, 192:117–127, March 1988.

P. C. van der Kruit and K. C. Freeman. The vertical velocity dispersion of the stars in the disks of two spiral galaxies. *ApJ*, 278:81–88, March 1984. doi: 10.1086/161769.

P. C. van der Kruit and K. C. Freeman. Stellar kinematics and the stability of disks in spiral galaxies. *ApJ*, 303:556–572, April 1986. doi: 10.1086/164102.

P. C. van der Kruit and L. Searle. Surface photometry of edge-on spiral galaxies. I - A model for the three-dimensional distribution of light in galactic disks. *A&A*, 95:105–115, February 1981a.

P. C. van der Kruit and L. Searle. Surface Photometry of Edge-On Spiral Galaxies. II - the Distribution of Light and Colour in the Disk and Spheroid of NGC891. *A&A*, 95:116–+, February 1981b.

P. C. van der Kruit and L. Searle. Surface photometry of edge-on spiral galaxies. III - Properties of the three-dimensional distribution of light and mass in disks of spiral galaxies. *A&A*, 110:61–78, June 1982a.

P. C. van der Kruit and L. Searle. Surface photometry of edge-on spiral galaxies. IV - The distribution of light, colour, and mass in the disk and spheroid of NGC 7814. *A&A*, 110: 79–94, June 1982b.

A. van der Wel, M. Franx, P. G. van Dokkum, R. E. Skelton, I. G. Momcheva, K. E. Whitaker, G. B. Brammer, E. F. Bell, H.-W. Rix, S. Wuyts, H. C. Ferguson, B. P. Holden, G. Barro, A. M. Koekemoer, Y.-Y. Chang, E. J. McGrath, B. Häussler, A. Dekel, P. Behroozi, M. Fumagalli, J. Leja, B. F. Lundgren, M. V. Maseda, E. J. Nelson, D. A. Wake, S. G. Patel, I. Labbé, S. M. Faber, N. A. Grogin, and D. D. Kocevski. 3D-HST+CANDELS: The Evolution of the Galaxy Size-Mass Distribution since z = 3. *ApJ*, 788:28, June 2014. doi: 10.1088/0004-637X/788/1/28.

H. Velazquez and S. D. M. White. Sinking satellites and the heating of galaxy discs. *MNRAS*, 304:254–270, April 1999. doi: 10.1046/j.1365-8711.1999.02354.x.

C. Vera-Ciro, E. D'Onghia, J. Navarro, and M. Abadi. The Effect of Radial Migration on Galactic Disks. *ApJ*, 794:173, October 2014. doi: 10.1088/0004-637X/794/2/173.

J. V. Villumsen. Evolution of the velocity distribution in galactic disks. *ApJ*, 290:75–85, March 1985. doi: 10.1086/162960.

S. D. M. White and C. S. Frenk. Galaxy formation through hierarchical clustering. *ApJ*, 379:52–79, September 1991. doi: 10.1086/170483.

R. Wielen. The diffusion of stellar orbits derived from the observed age-dependence of the velocity dispersion. *A&A*, 60:263–275, September 1977.

B. F. Williams, J. J. Dalcanton, A. E. Dolphin, J. Holtzman, and A. Sarajedini. The Detection of Inside-Out Disk Growth in M33. *ApJ*, 695:L15–L19, April 2009. doi: 10. 1088/0004-637X/695/1/L15.

H. Wu, D. Burstein, Z. Deng, X. Zhou, Z. Shang, Z. Zheng, J. Chen, H. Su, R. A. Windhorst, W.-p. Chen, Z. Zou, X. Xia, Z. Jiang, J. Ma, S. Xue, J. Zhu, F. Cheng, Y.-I. Byun, R. Chen, L. Deng, X. Fan, L.-Z. Fang, X. Kong, Y. Li, W. Lin, P. Lu, W.-h. Sun, W.-s. Tsay, W. Xu, H. Yan, B. Zhao, and Z. Zheng. Intermediate-Band Surface Photometry of the Edge-on Galaxy NGC 4565. *AJ*, 123:1364–1380, March 2002. doi: 10.1086/338849.

P. Yoachim and J. J. Dalcanton. Structural Parameters of Thin and Thick Disks in Edge-on Disk Galaxies. *AJ*, 131:226–249, January 2006. doi: 10.1086/497970.

R. Zinn and M. J. West. The globular cluster system of the galaxy. III - Measurements of radial velocity and metallicity for 60 clusters and a compilation of metallicities for 121 clusters. *ApJS*, 55:45–66, May 1984. doi: 10.1086/190947.

M. Zoccali, A. Renzini, S. Ortolani, L. Greggio, I. Saviane, S. Cassisi, M. Rejkuba, B. Barbuy, R. M. Rich, and E. Bica. Age and metallicity distribution of the Galactic bulge from extensive optical and near-IR stellar photometry. *A&A*, 399:931–956, March 2003. doi: 10.1051/0004-6361:20021604.

A. Additional Notes to the Color Metallicity relation

A.1. Description of the fit of the RGB

We parametrized the RGB with the function

$$M = a + b \cdot \text{color} + c/(\text{color} + d), \tag{A.1}$$

as given in Saviane et al. [2000]. Since the data do not only contain RGB stars, but also the horizontal branch, blue stragglers and foreground stars, we have defined a region to guarantee a high fraction of RGB stars in our fit sample. The extent of this region can be seen as the red frame in Fig. A.1. Note that this region excludes also the red clump.

In some clusters, there is a distinct asymptotic giant branch (AGB) visible, which lies on the blue side of the RGB (it is mostly seen at F814W magnitudes between -1 and -2). As in Saviane et al. [2000], we have removed these AGB stars by excluding all detections that lie blue wards of a reference line with the same slope for all clusters (denoted in Figures A.1 through A.9 by a dashed red line). The horizontal position of the reference line was set to be 0.05 mag blue wards (at F814W=-0.5) of a first fit of all stars in the RGB region and then excluding. The fit including all stars is shown in the CMDs as black dashed line, while the final fit after the AGB removal is shown as black solid line.

For the actual fit we used the python package scipy.odr. This routine performs an orthogonal distance regression, i.e. it minimizes the orthogonal distance between the curve and the data points. The distance of each data point is weighted with its measurement uncertainty. This method is a variation of the typical χ^2 minimization, now generalized for data with uncertainties on both variables.

The ACSGCS team reports photometric uncertainties for each individual star, which are typically quite small; the median uncertainty in F814W is only 0.003 mag. This is much smaller than both the observed scatter in the RGB and the errors that are found in the artificial star test at a level of F814W≈ 0. (There are no artificial star tests at brighter magnitudes.) The mean measurement error estimated from the difference of the input and recovered magnitudes in the artificial star test are 0.06 mag in F814W and 0.03 mag in color. These estimated are added in quadrature to the reported uncertainties of each star. The smaller error in color is due to the fact that errors in both bands are correlated. Thus the uncertainty of the difference of both bands is smaller than the uncertainty in each band.

Finally, we visually inspected each CMD with its fit, to check for any residual problems of our clusters. After this inspection we excluded four more clusters from the sample: NGC 6838 and NGC 6441, because their RGB fits do not reach the $M_I = -3.5$ level; NGC 6388 (and again NGC 6441), because their red clumps seem to be to faint [Bellini et al., 2013, also found problems with differential reddening and multiple populations in these two clusters]; and NGC 6715, because it has a clear and strong second RGB.

A.2. Properties of the Globular clusters

The properties of the globular clusters, from the literature and determined in this work, are summarized in Table A.1 and Table A.2 respectively.
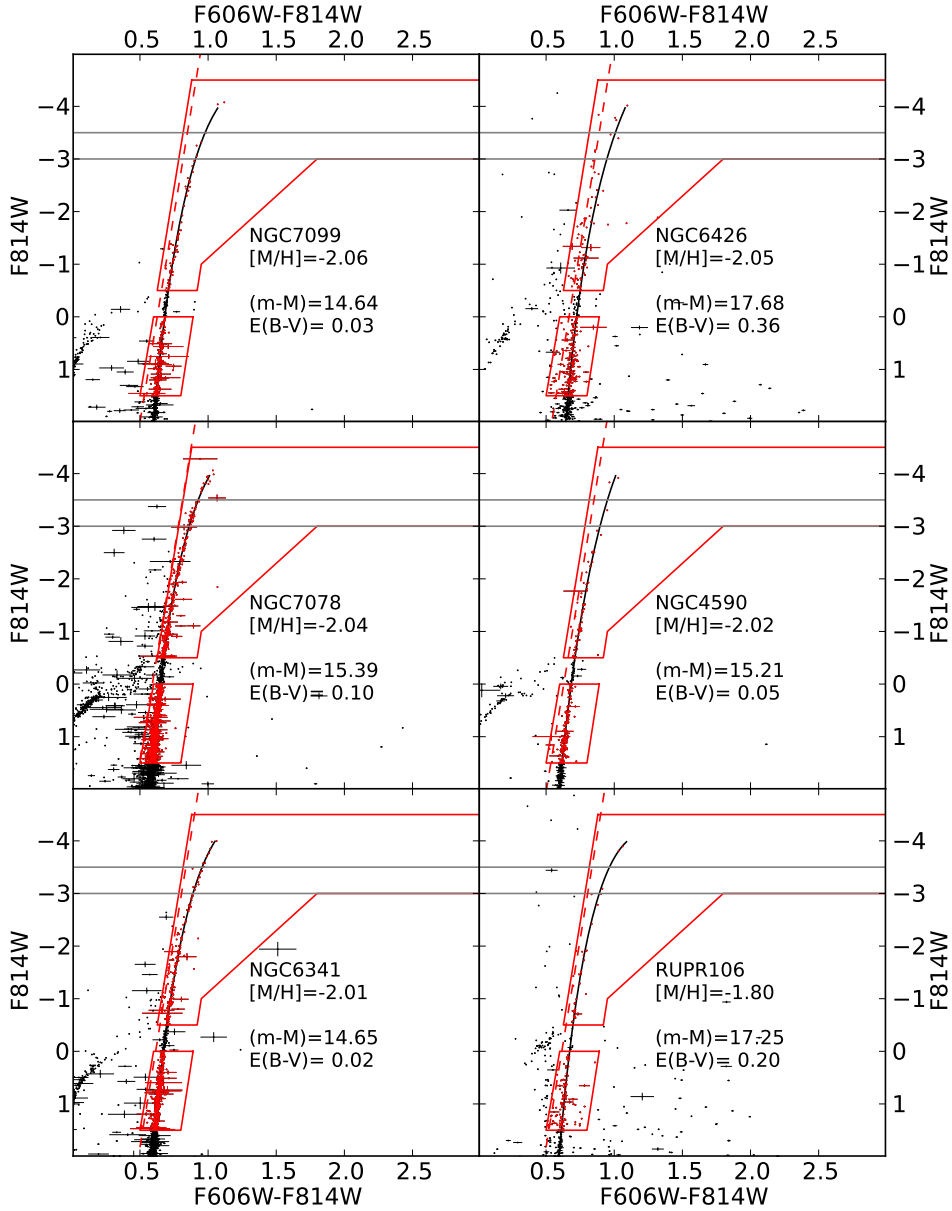
Figure A.1.: CMDs of the 53 clusters in our sample, with fitted RGB curves. The two horizontal gray lines indicate the magnitudes at which the colors are measured. The red frame gives the region where stars are used for the fit. The reference line to separate AGB from RGB stars is shown as red dashed line. The solid black line shows the best-fit RGB function after the rejection of the AGB. Note, that all stars in the CMD are actually drawn with errorbars, but for many stars the reported errors are too small to be visible in these plots.

Figure A.2.: as Fig. A.1.

Figure A.3.: as Fig. A.1.

Figure A.4.: as Fig. A.1.
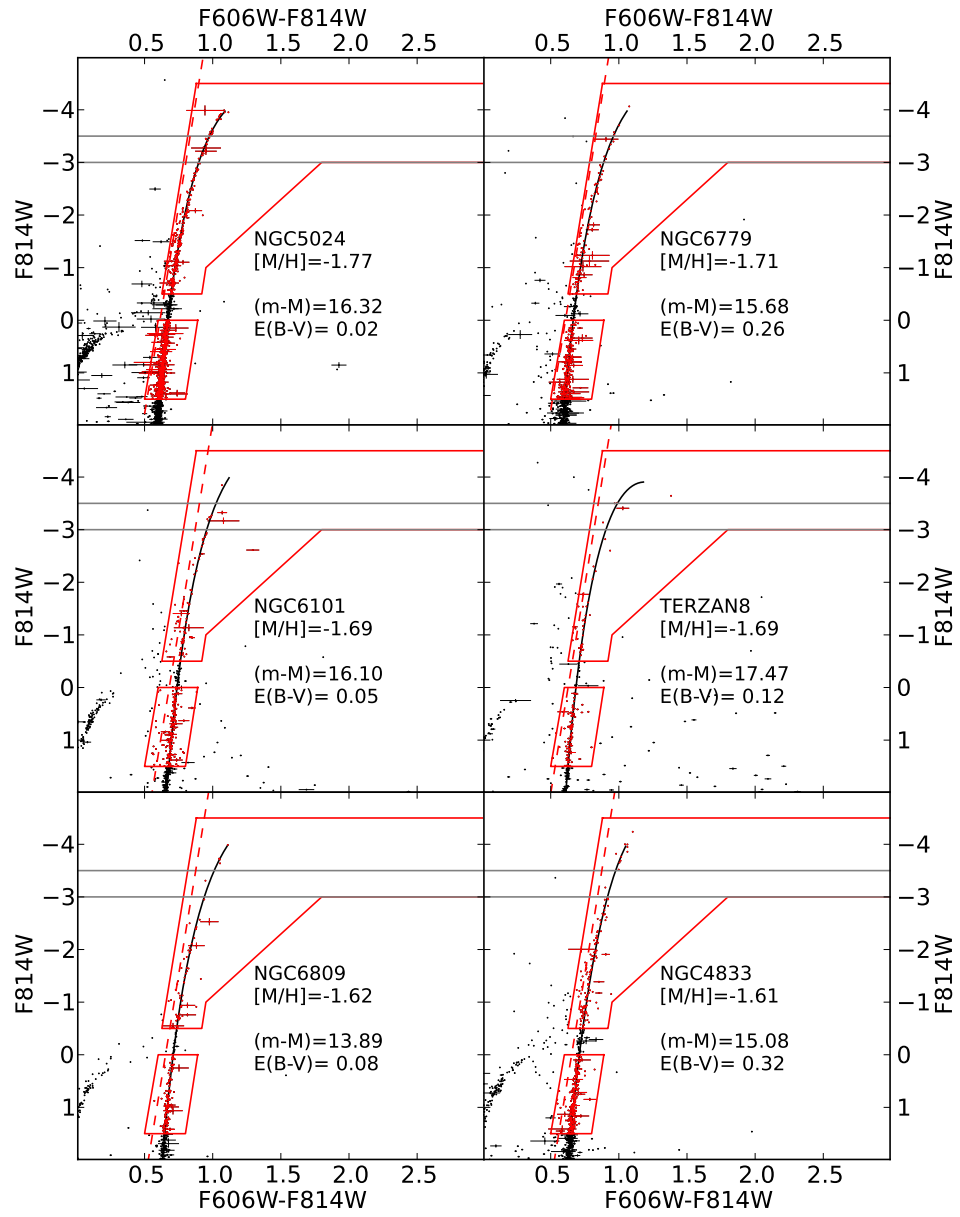
Figure A.5.: as Fig. A.1.

Figure A.6.: as Fig. A.1.

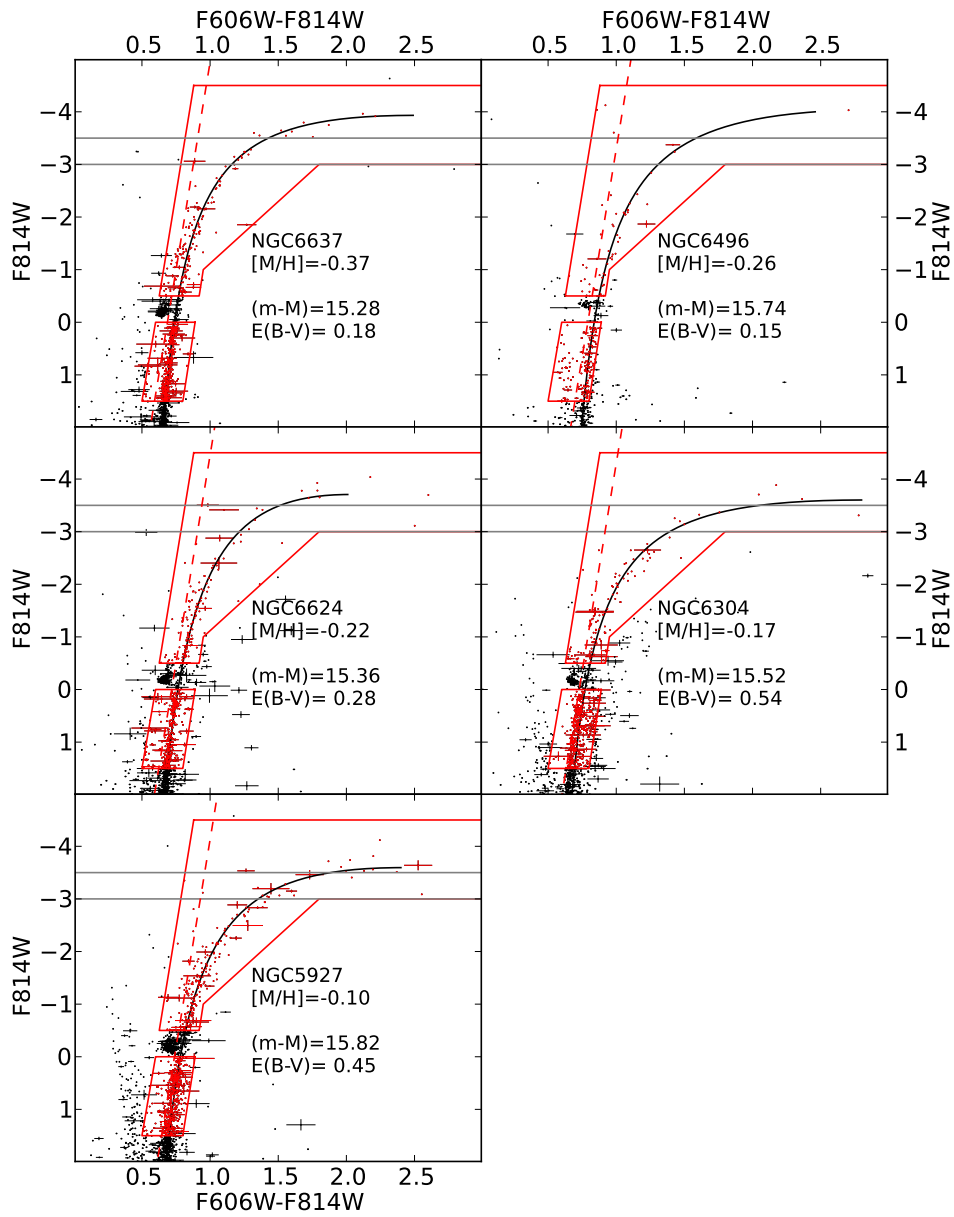Figure A.7.: as Fig. A.1.
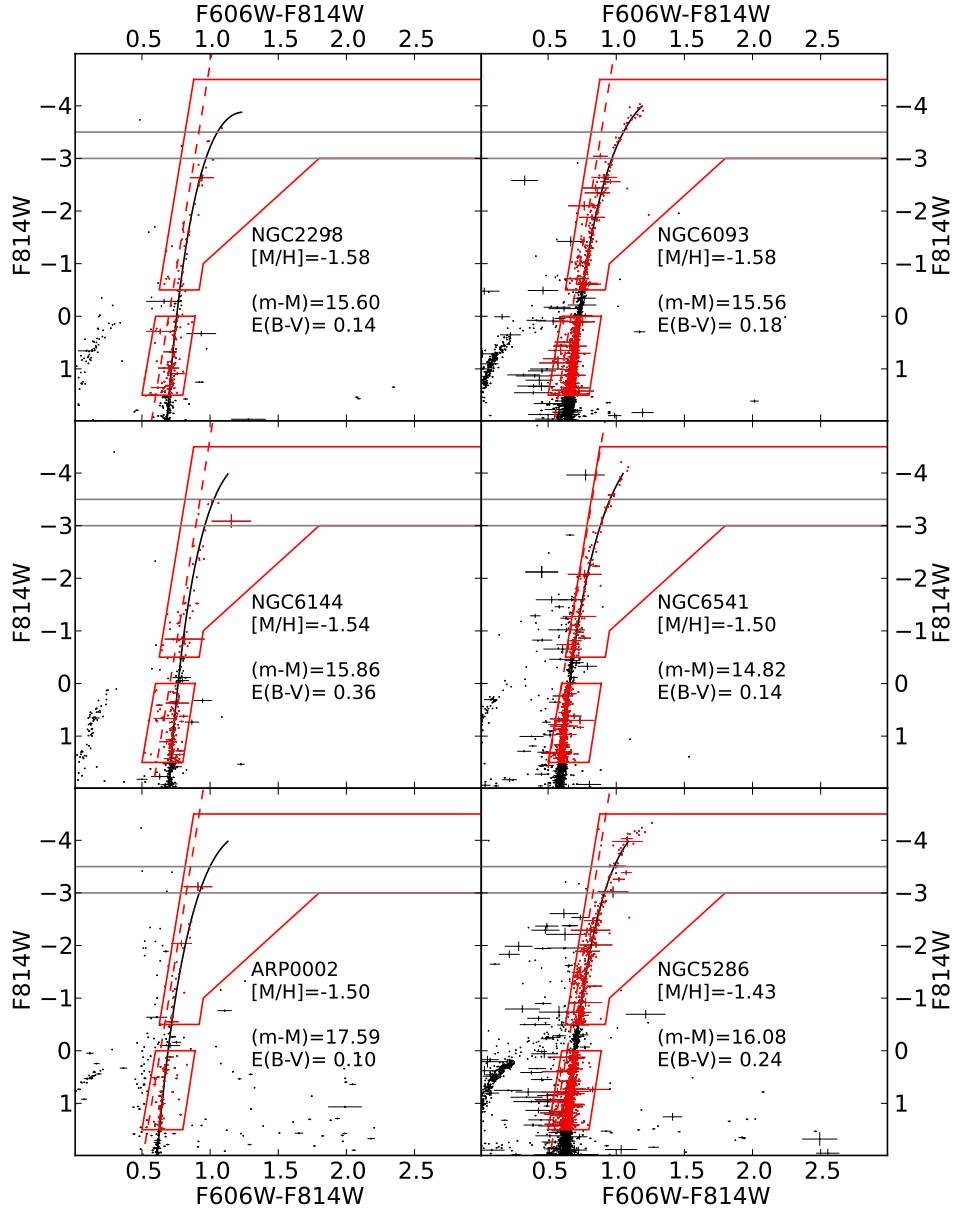
Figure A.8.: as Fig. A.1.

Figure A.9.: as Fig. A.1.

A. Additional Notes to the Color Metallicity relation

Table A.1.: Literature data for the clusters used in this work

name	RA [°]	DEC [°]	$(m-M)_V$ [mag]	$E(B-V)$ [mag]	[Fe/H]$_{H10}$ [dex]	[Fe/H]$_{C+10}$ [dex]	$\sigma_{[Fe/H]}$ [dex]	$[\alpha/Fe]$ [dex]	Age
(1)	(2)	(3)	(4)	(5)	(6)	(7)	(8)	(9)	(10)
Arp 2	292.1838	-29.6444	17.59	0.10	-1.75	-1.74	0.08	0.34	0.85
IC 4499	225.0769	-81.7863	17.08	0.23	-1.53	-1.62	0.09	...	...
Lynga 7	242.7652	-54.6822	16.78	0.73	-1.01	-0.68	0.06	...	1.13
NGC 104	6.0236	-71.9187	13.37	0.04	-0.72	-0.76	0.02	0.42	1.02
NGC 362	15.8094	-69.1512	14.83	0.05	-1.26	-1.30	0.04	0.30	0.81
NGC 1261	48.0675	-54.7838	16.09	0.01	-1.27	-1.27	0.08	...	0.80
NGC 1851	78.5282	-39.9534	15.47	0.02	-1.18	-1.18	0.08	0.38	0.78
NGC 2298	102.2475	-35.9947	15.60	0.14	-1.92	-1.96	0.04	0.50	0.99
NGC 2808	138.0129	-63.1365	15.59	0.22	-1.14	-1.18	0.04	0.33	0.85
NGC 3201	154.4034	-45.5875	14.20	0.24	-1.59	-1.51	0.02	0.33	0.80
NGC 4590	189.8666	-25.2559	15.21	0.05	-2.23	-2.27	0.04	0.35	0.90
NGC 4833	194.8913	-69.1235	15.08	0.32	-1.85	-1.89	0.05	...	0.98
NGC 5024	198.2302	18.1682	16.32	0.02	-2.10	-2.06	0.09	...	0.99
NGC 5139	201.6968	-46.5204	13.94	0.12	-1.53	-1.64	0.09	...	0.90
NGC 5272	205.5484	28.3773	15.07	0.01	-1.50	-1.50	0.05	0.34	0.89
NGC 5286	206.6117	-50.6257	16.08	0.24	-1.69	-1.70	0.07	...	0.98
NGC 5904	229.6384	2.0810	14.46	0.03	-1.29	-1.33	0.02	0.38	0.83
NGC 5927	232.0029	-49.3270	15.82	0.45	-0.49	-0.29	0.07	...	0.99
NGC 5986	236.5125	-36.2136	15.96	0.28	-1.59	-1.63	0.08	...	0.95
NGC 6093	244.2600	-21.0239	15.56	0.18	-1.75	-1.75	0.08	0.24	0.98
NGC 6101	246.4505	-71.7978	16.10	0.05	-1.98	-1.98	0.07	...	0.98
NGC 6121	245.8968	-25.4743	12.82	0.35	-1.16	-1.18	0.02	0.51	0.98
NGC 6144	246.8077	-25.9765	15.86	0.36	-1.76	-1.82	0.05	...	1.08
NGC 6171	248.1328	-12.9462	15.05	0.33	-1.02	-1.03	0.02	0.49	1.09
NGC 6205	250.4218	36.4599	14.33	0.02	-1.53	-1.58	0.04	0.31	0.91
NGC 6218	251.8091	-0.0515	14.01	0.19	-1.37	-1.43	0.02	0.41	0.99
NGC 6254	254.2877	-3.8997	14.08	0.28	-1.56	-1.57	0.02	0.37	0.89
NGC 6304	258.6344	-28.5380	15.52	0.54	-0.45	-0.37	0.07	...	1.06
NGC 6341	259.2808	43.1359	14.65	0.02	-2.31	-2.35	0.05	0.46	1.03
NGC 6362	262.9791	-66.9517	14.68	0.09	-0.99	-1.07	0.05	...	1.06
NGC 6426	266.2277	3.1701	17.68	0.36	-2.15	-2.36	0.06	...	...
NGC 6496	269.7653	-43.7341	15.74	0.15	-0.46	-0.46	0.07	...	0.97
NGC 6541	272.0098	-42.2851	14.82	0.14	-1.81	-1.82	0.08	0.43	1.01
NGC 6584	274.6567	-51.7842	15.96	0.10	-1.50	-1.50	0.09	...	0.88
NGC 6624	275.9188	-29.6390	15.36	0.28	-0.44	-0.42	0.07	...	0.98
NGC 6637	277.8462	-31.6519	15.28	0.18	-0.64	-0.59	0.07	0.31	1.02
NGC 6652	278.9401	-31.0093	15.28	0.09	-0.81	-0.76	0.14	...	1.01
NGC 6656	279.0998	-22.0953	13.60	0.34	-1.70	-1.70	0.08	0.38	0.99
NGC 6681	280.8032	-31.7079	14.99	0.07	-1.62	-1.62	0.08	...	1.00
NGC 6717	283.7752	-21.2985	14.94	0.22	-1.26	-1.26	0.07	...	1.03
NGC 6723	284.8881	-35.3678	14.84	0.05	-1.10	-1.10	0.07	0.50	1.02
NGC 6752	287.7171	-58.0154	13.13	0.04	-1.54	-1.55	0.01	0.43	0.92
NGC 6779	289.1482	30.1835	15.68	0.26	-1.98	-2.00	0.09	...	1.07
NGC 6809	294.9988	-29.0353	13.89	0.08	-1.94	-1.93	0.02	0.42	0.96
NGC 6934	308.5474	7.4045	16.28	0.10	-1.47	-1.56	0.09	...	0.87
NGC 6981	313.3654	-11.4627	16.31	0.05	-1.42	-1.48	0.07	...	0.85
NGC 7006	315.3724	16.1873	18.23	0.05	-1.52	-1.46	0.06	0.28	...
NGC 7078	322.4930	12.1670	15.39	0.10	-2.37	-2.33	0.02	0.40	1.01
NGC 7089	323.3626	0.8233	15.50	0.06	-1.65	-1.66	0.07	0.41	0.92
NGC 7099	325.0922	-22.8201	14.64	0.03	-2.27	-2.33	0.02	0.37	1.01
Pal 2	71.5246	31.3815	21.01	1.24	-1.42	-1.29	0.09	...	...
Rup 106	189.6675	-50.8497	17.25	0.20	-1.68	-1.78	0.08	-0.03	...
Terzan 8	295.4350	-32.0005	17.47	0.12	-2.16	-2.02	0.06	0.45	0.95

Notes. Keys to columns: (1)-(6) name, right ascension, declination, visual distance modulus, color excess and metallicity from Harris [2010]; (7-9) metallicity, its uncertainty and alpha enhancement from Carretta et al. [2010]; (10) relative age from Marín-Franch et al. [2009].

Table A.2.: Results for all clusters used in this work.

name	$(V-I)_{-3.5}$ [mag]	$\sigma_{-3.5}$ [mag]	$(V-I)_{-3.0}$ [mag]	$\sigma_{-3.0}$ [mag]	S	σ_S	$M_V(\text{HB})$ [mag]
(1)	(2)	(3)	(4)	(5)	(6)	(7)	(8)
Arp 2	0.999	0.027	0.920	0.011	13.415	0.826	0.45
IC 4499	0.976	0.016	0.902	0.007	13.460	0.620	0.30
Lynga 7	1.321	0.042	1.158	0.016	7.829	0.587	0.40
NGC 104	1.397	0.017	1.162	0.006	6.860	0.540	0.44
NGC 362	1.069	0.009	0.953	0.005	11.578	0.568	0.52
NGC 1261	1.092	0.024	0.977	0.007	11.190	0.622	0.53
NGC 1851	1.110	0.007	0.999	0.005	11.059	0.545	0.53
NGC 2298	1.054	0.019	0.969	0.010	13.736	0.762	0.35
NGC 2808	1.077	0.008	0.967	0.004	11.215	0.461	0.56
NGC 3201	1.048	0.012	0.973	0.005	11.307	0.512	0.30
NGC 4590	0.950	0.012	0.896	0.006	13.559	0.505	0.30
NGC 4833	0.976	0.004	0.916	0.003	13.888	0.476	0.30
NGC 5024	0.975	0.002	0.897	0.002	12.324	0.525	0.20
NGC 5139	1.044	0.011	0.960	0.006	11.553	0.521	0.40
NGC 5272	1.018	0.003	0.929	0.002	12.281	0.528	0.40
NGC 5286	0.985	0.005	0.913	0.003	14.017	0.554	0.40
NGC 5904	1.057	0.005	0.962	0.003	11.818	0.523	0.50
NGC 5927	1.883	0.091	1.353	0.025	4.849	0.680	0.51
NGC 5986	1.019	0.006	0.939	0.004	12.747	0.553	0.40
NGC 6093	1.053	0.006	0.968	0.006	12.131	0.589	0.40
NGC 6101	1.024	0.018	0.956	0.007	13.104	0.698	0.30
NGC 6121	1.179	0.028	1.068	0.015	10.401	0.849	0.30
NGC 6144	1.028	0.014	0.961	0.009	14.346	0.962	0.25
NGC 6171	1.231	0.017	1.108	0.017	9.498	0.622	0.42
NGC 6205	1.038	0.008	0.948	0.003	11.467	0.509	0.40
NGC 6218	1.119	0.015	1.003	0.007	9.887	0.583	0.30
NGC 6254	1.061	0.021	0.972	0.009	11.391	0.524	0.50
NGC 6304	2.051	0.176	1.392	0.043	4.257	0.848	0.49
NGC 6341	0.956	0.003	0.889	0.003	13.381	0.491	0.30
NGC 6362	1.186	0.023	1.034	0.009	9.554	0.571	0.54
NGC 6426	1.008	0.027	0.946	0.026	13.152	1.967	0.40
NGC 6496	1.587	0.078	1.308	0.036	5.976	0.772	0.53
NGC 6541	0.954	0.004	0.883	0.003	12.937	0.523	0.30
NGC 6584	1.015	0.005	0.925	0.003	12.120	0.557	0.40
NGC 6624	1.514	0.096	1.215	0.040	6.412	0.742	0.47
NGC 6637	1.427	0.023	1.159	0.009	7.243	0.675	0.46
NGC 6652	1.321	0.021	1.147	0.014	7.829	0.564	0.47
NGC 6656	1.014	0.012	0.949	0.005	13.284	0.523	0.50
NGC 6681	1.087	0.010	0.983	0.005	12.476	0.579	0.60
NGC 6717	1.091	0.062	0.995	0.041	11.462	1.647	0.60
NGC 6723	1.149	0.022	1.033	0.010	10.487	0.574	0.49
NGC 6752	1.075	0.025	0.980	0.010	10.063	0.564	0.25
NGC 6779	0.960	0.005	0.888	0.002	13.579	0.519	0.40
NGC 6809	1.011	0.007	0.938	0.006	13.041	0.638	0.40
NGC 6934	1.050	0.018	0.962	0.015	10.874	1.048	0.40
NGC 6981	1.015	0.009	0.933	0.004	12.173	0.559	0.40
NGC 7006	1.035	0.014	0.955	0.006	12.705	0.575	0.40
NGC 7078	0.927	0.002	0.861	0.002	13.877	0.520	0.30
NGC 7089	0.996	0.005	0.909	0.006	12.324	0.615	0.30
NGC 7099	0.978	0.005	0.908	0.003	13.211	0.475	0.40
Pal 2	1.019	0.015	0.962	0.010	11.582	0.558	0.30
Rup 106	0.965	0.014	0.890	0.009	13.509	0.873	0.30
Terzan 8	0.990	0.023	0.905	0.011	13.440	0.872	0.30

Notes. Keys to columns: (1) name; (2)-(3) RGB color at M_I=-3.5 and its uncertainty; (4)-(5) RGB color at M_I=-3.0 and its uncertainty; (6)-(7) S-index and its uncertainty (8) absolute magnitude of the horizontal branch used for the determination of the S-index. Note that we use V and I as shorthand for F606W and F814W respectively here.

B. Additional Notes to the Structure of Low Mass Galaxies

B.1. Scaleheights in Spitzer's [3.6μm]

We show here the measurements of scaleheights along the major axis of the galaxies for the Spitzer data. We have fitted both a simple sech^2 and generalized sech$^{2/n}$. The Spitzer profiles are usually more peaked than a sech^2 (see also Sect. 3.3.3.3) and we find $n > 1$. The scaleheights of the sech$^{2/n}$ fits are in good agreement with the RGB scaleheights and there is no or very little flaring.

The parameter n of the sech$^{2/n}$ increases towards the center of the galaxies, i.e. the profiles in the inner disks are more peaked than in the outer disks.
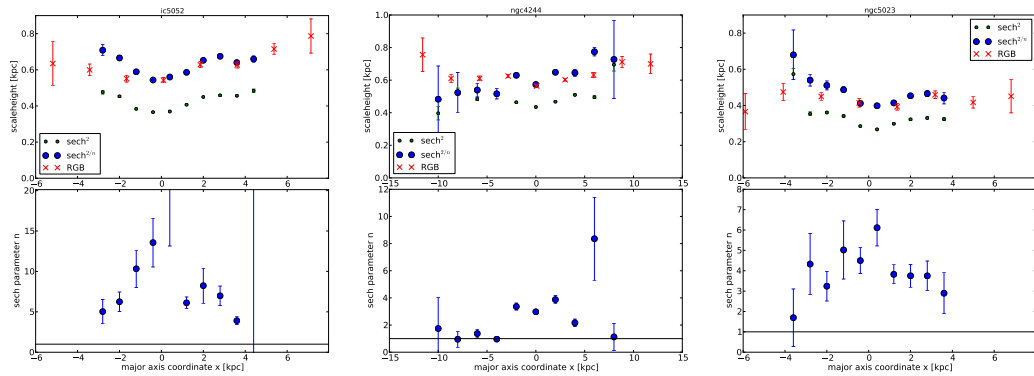
Figure B.1.: *upper panels*: Scaleheights in Spitzer IRAC channel 1 as a function of position along the major axis (from left to right: IC 5052, NGC 4244, NGC 5023). *lower panels*: parameter n of the generalized sech$^{2/n}$ fits.

B.2. 2D Fits

We present here the details of the two-dimensional fits to the star count maps. For each galaxy we show for each population the data and the model image. We also show the weighted residuals. We have defined the residual $wdev_i$ of each pixel in the context of Poisson noise dominated data to be

$$wdev_i = \text{sign}(n_i - m_i)\sqrt{-2(n_i \ln m_i - m_i + n_i(1 - \ln n_i))} \qquad \text{(B.1)}$$

with n_i the pixel value of the data and m_i the pixel value of the model. It is analogue to the normal weighted residual $(n_i - m_i)/\sigma_i$ in the sense that it is positive for $n_i > m_i$ and negative for $n_i < m_i$, and it is $PLR = \sum_i (wdev_i^2)$.
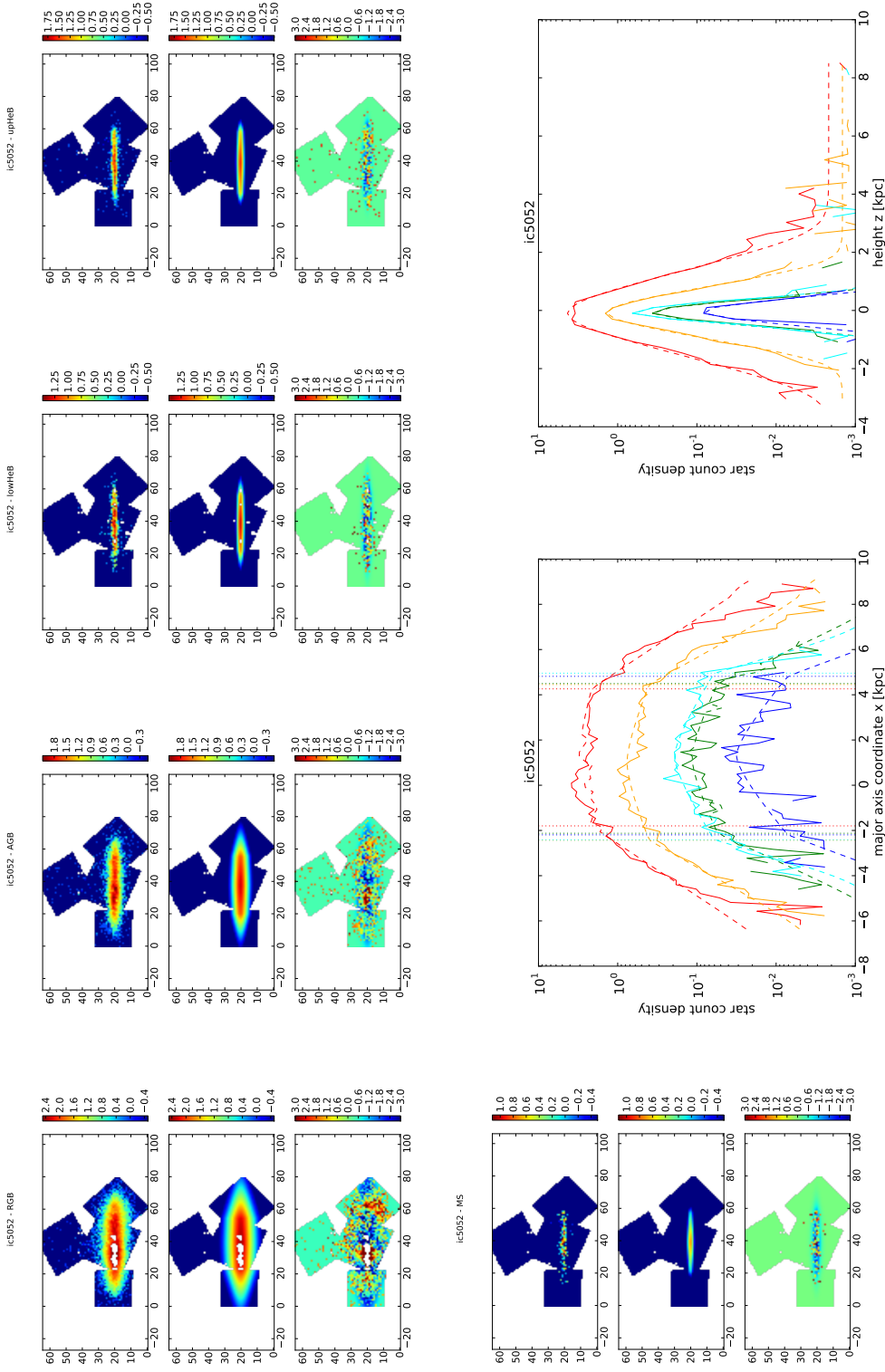
Figure B.2.: *top row:* 2D fit maps of the five populations in IC 5052 (from left to right: RGB, AGB, lowHeB, upHeB, MS. Each panel contains three maps: *top:* stellar density maps; *middle:* best fit model, *bottom:* weighted deviation between model and data). Note the two overdensities in the residual map of the fit to the RGB data (left panel); *bottom row (middle and right):* major and minor axis profiles of the data (solid lines) and the 2D models (dashed lines). Note that the model lines may show irregularities (as the real data does) due to masked out regions.
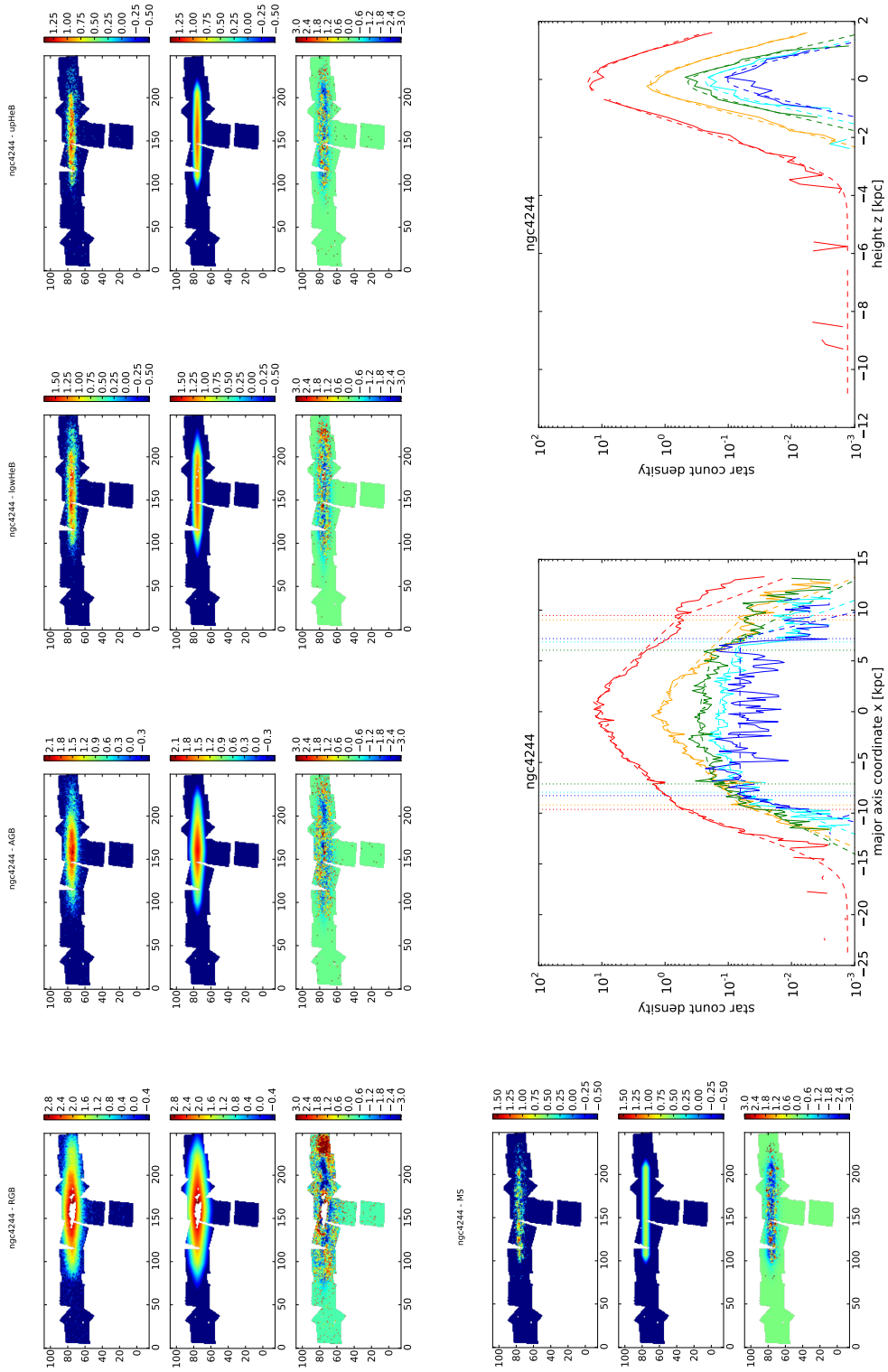
Figure B.3.: as Fig. B.2, but for NGC 4244. Note that we have restricted the fits to the left side of the galaxies, due to irregularities at the right end.
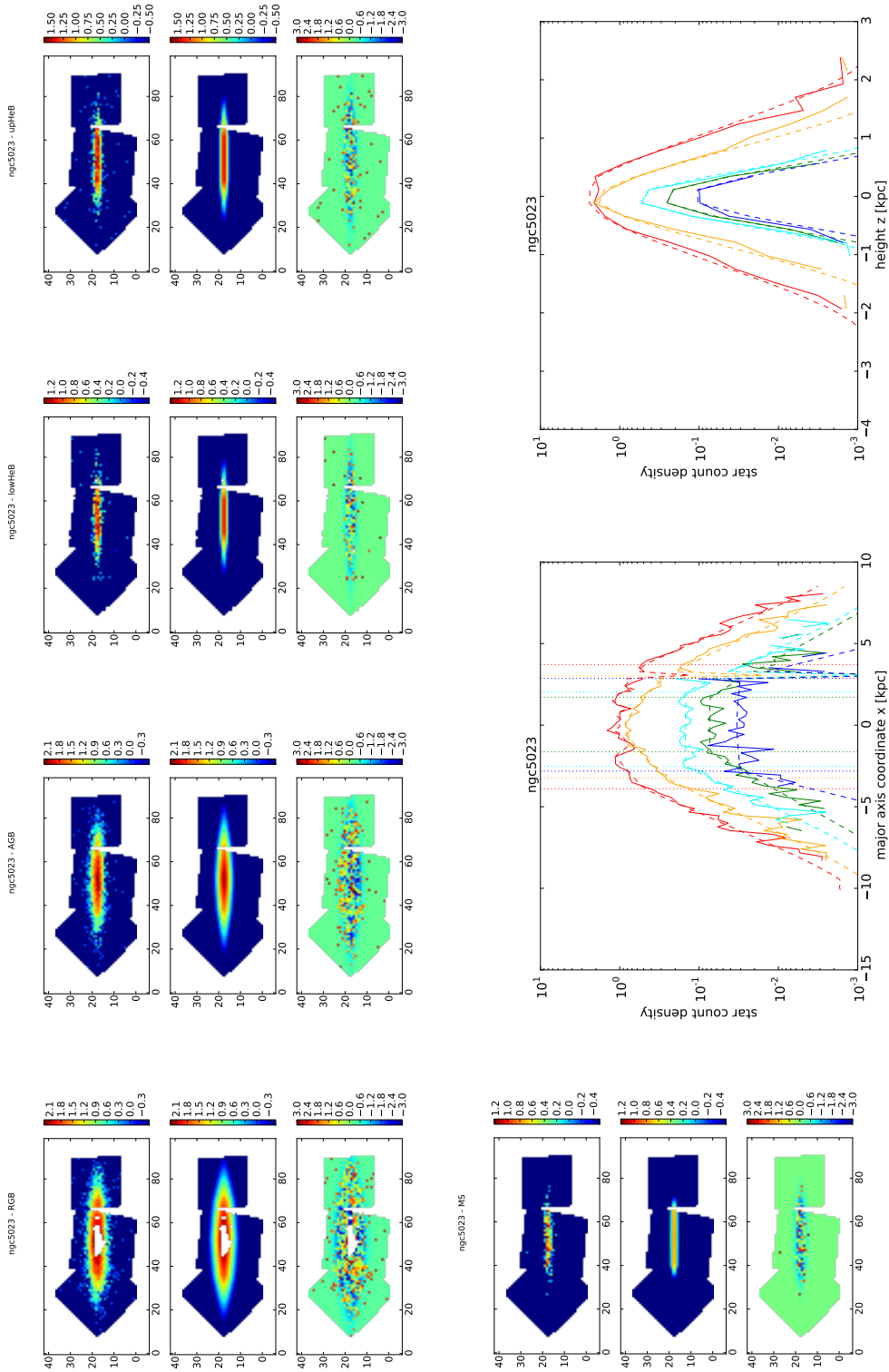
Figure B.4.: as Fig. B.2, but for NGC 5023.

C. Additional Notes to the Structure of Massive Galaxies

C.1. Details of 2D fits

Table C.1.: Overview of all best fit parameters

| population | disk parameters | | | | | | Sersic parameters | | | |
	I_{sky} arcsec^{-2}	n_0 arcsec^{-2}	h_{in} kpc	h_{out} kpc	r_b kpc	z_0 kpc	ϵ	n	I_e arcsec^{-2}	r_e kpc
NGC 891										
RGB	0.0083	3.27	32.34	1.30	13.29	0.79	0.47	2.53	4.47	2.78
RGB – thin	0.0067	3.21	63.53	1.13	13.19	0.60	0.30	8.00	29.79	0.76
RGB – thick		33.13	4.60	1.64	15.08	1.80				
AGB	0.0021	1.97	14.04	1.55	12.97	0.66	0.44	6.62	1543.2	0.15
allyoung	0.0006	2.70	4.87	1.04	13.17	0.33	0.60	1.00	0.01	5.65
NGC 4565										
RGB	0.0047	7.11	21.33	1.82	24.70	1.18	0.47	8.00	23.24	1.97
RGB – thin	0.0063	1.65	11.41	1.14	25.99	1.16	0.37	4.41	225.06	0.75
RGB – thick		0.25	14.74	4.23	32.63	8.30				
AGB	0.0074	9.27	9.57	1.11	25.45	0.88	0.39	2.84	1929.0	0.39
allyoung	0.0020	2.47	166.15	0.83	27.18	0.64	0.60	5.87	1543.2	0.14
NGC 7814										
RGB	0.0021	-	-	-	-	-	0.40	10.20	192.90	0.53
RGB-disk	0.0007	7.04	1.88	0.05	17.33	0.97	0.34	10.00	10.03	1.58
AGB	0.0033	0.08	201.06	0.49	16.96	0.92	0.44	3.79	925.97	0.53
allyoung	0.0017	0.12	54.33	1.05	15.74	0.72	0.23	1.91	1.66	1.32

NGC 891
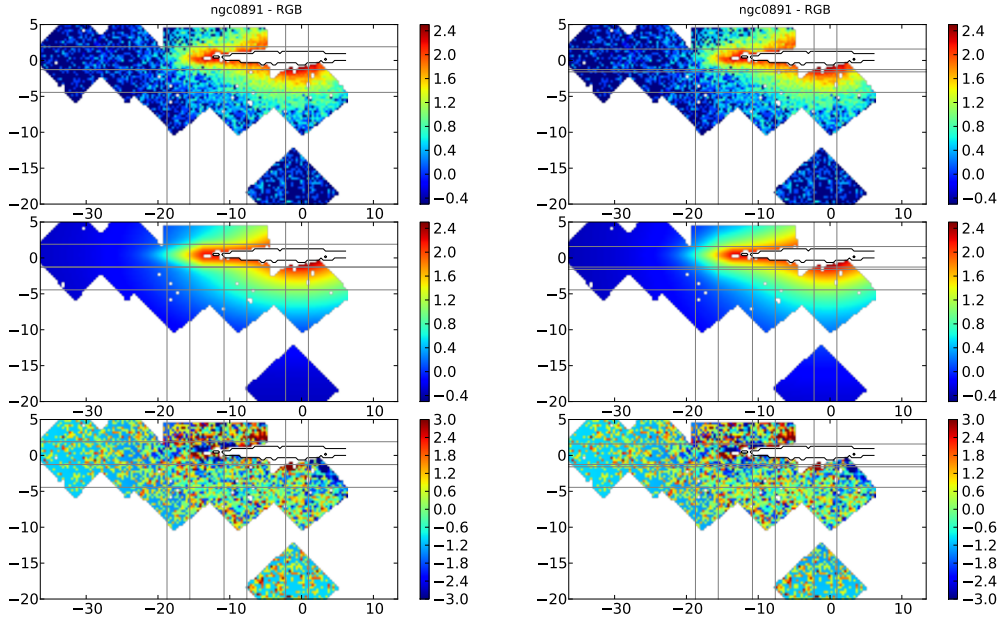
Figure C.1.: stellar density map (in logarithmic scale) of RGB stars in NGC 891: upper panel - data; middle panel - model; lower panel - residuals. Grey lines show the edges of the bins from where the radial and vertical profiles are extracted. *Left*: model with a single disk; *right*: model with two (thin and thick) disks.
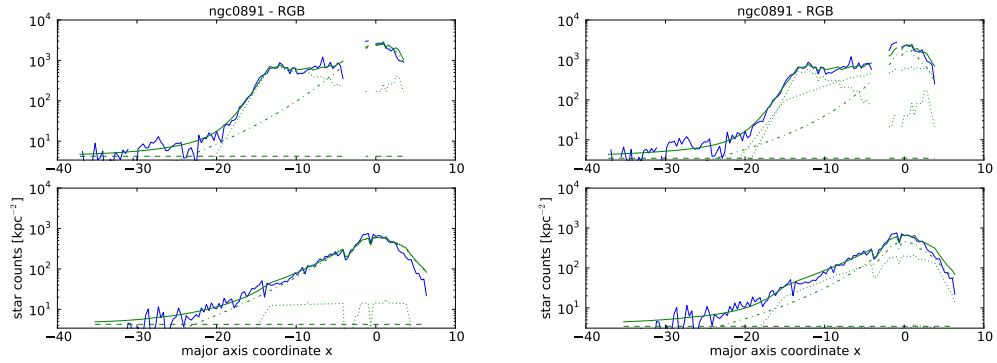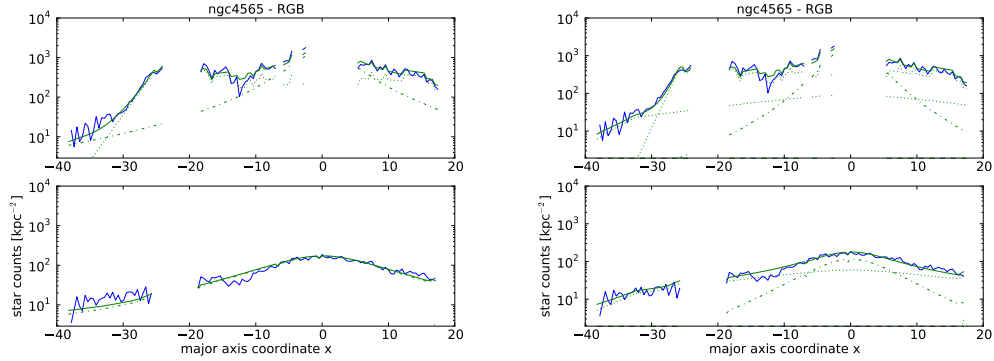

Figure C.2.: Radial profiles at two different heights. Blue shows is the data, green the model: solid – total model, dotted – disk component(s), dash-dotted – Sersic component, dashed – background. *Left*: model with a single disk; *right*:model with two (thin and thick) disks.
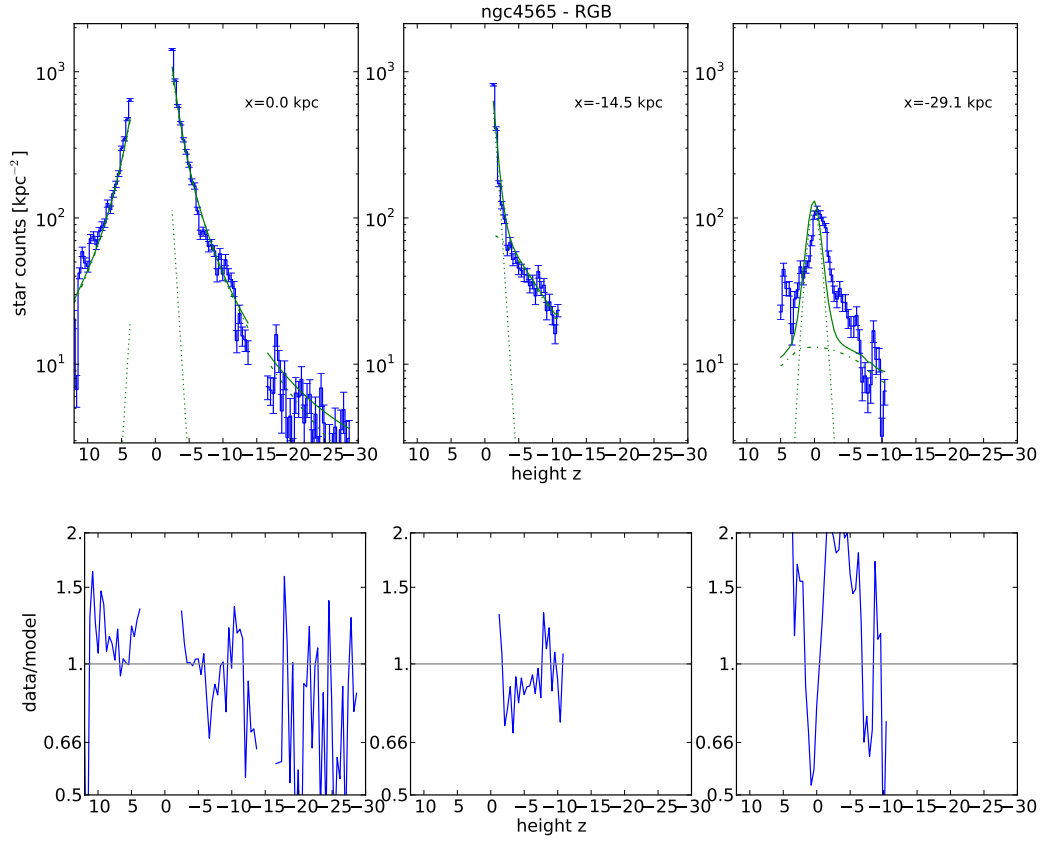
Figure C.3.: Vertical profiles of RGB density at three different positions in the galaxy, with the single disk 2D-models. Blue lines show the data, green the model: solid – total model, dotted – disk component(s), dash-dotted – Sersic component, dashed – background. The small panels below the profiles show the data to model ratios.
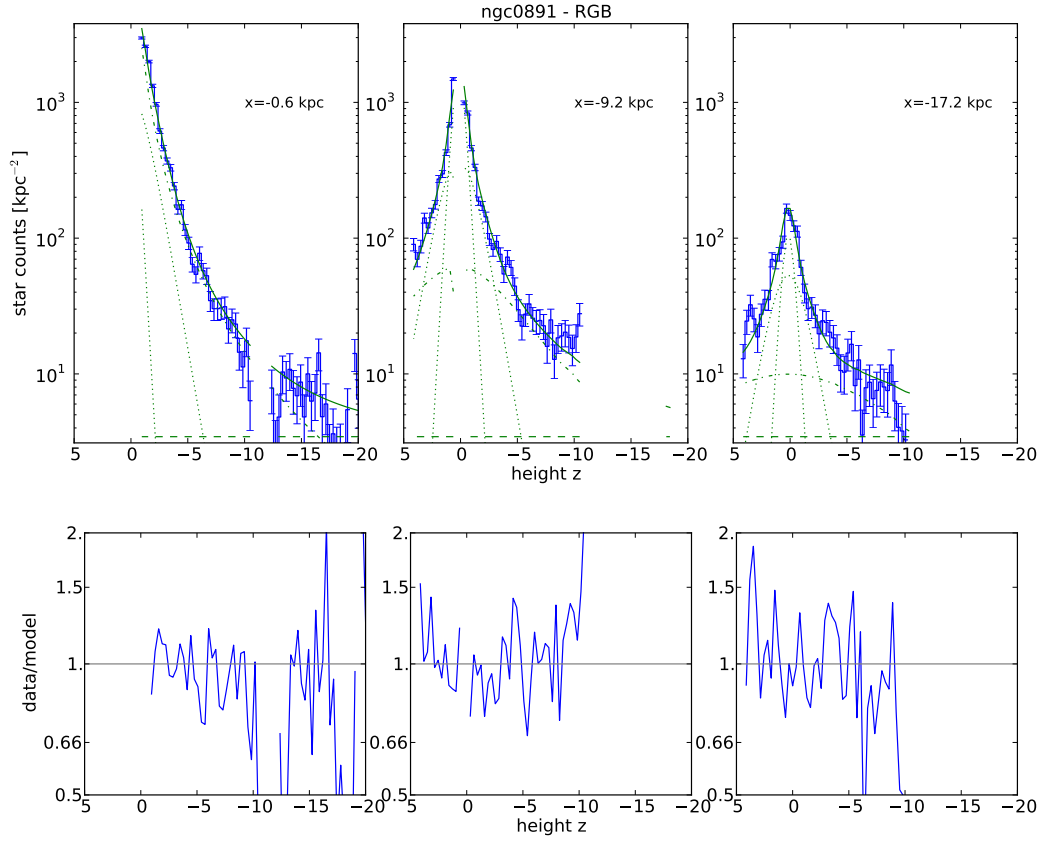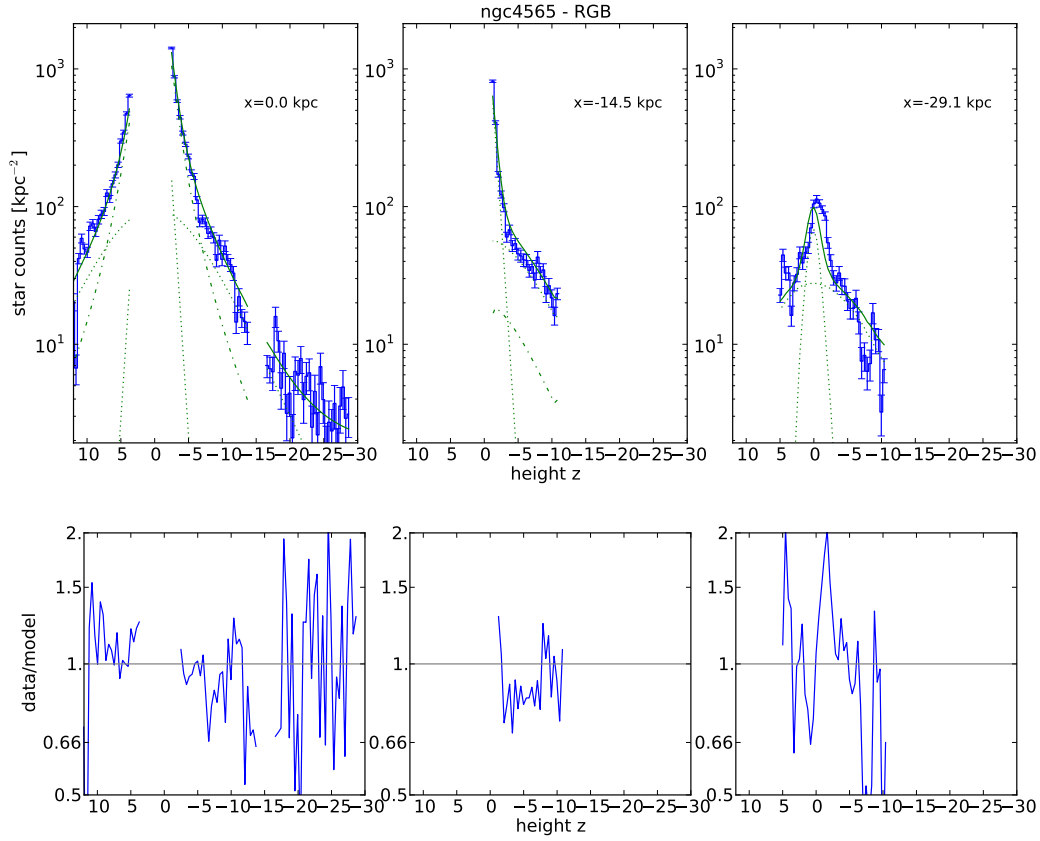
Figure C.4.: Vertical profiles of RGB density at three different positions in the galaxy, with the two disks 2D-models. Blue lines show the data, green the model: solid – total model, dotted – disk component(s), dash-dotted – Sersic component, dashed – background. The small panels below the profiles show the data to model ratios.
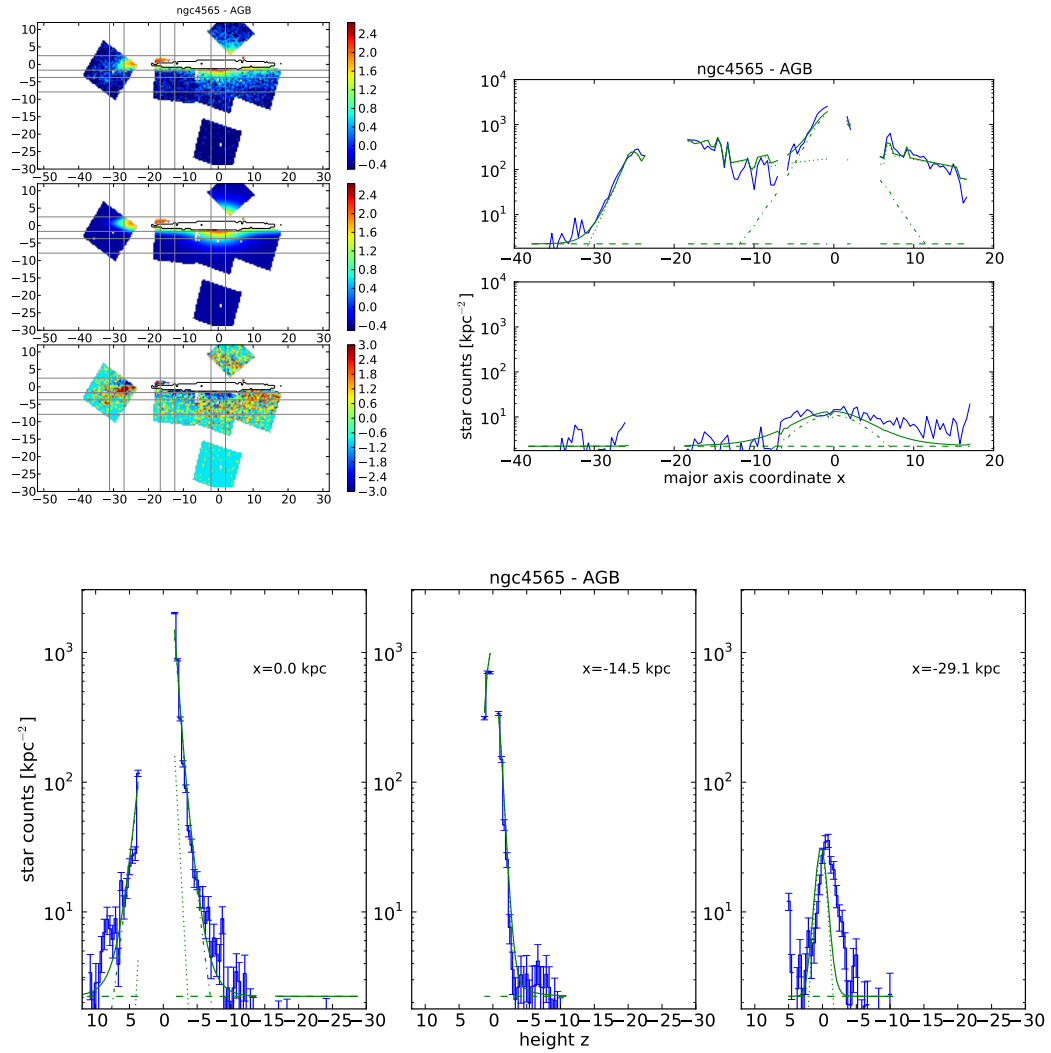
Figure C.5.: *upper left*: stellar density map of AGB stars in NGC 891: upper panel - data; middle panel - model; lower panel - residuals. *upper right*: radial profiles. *bottom*: vertical profiles.
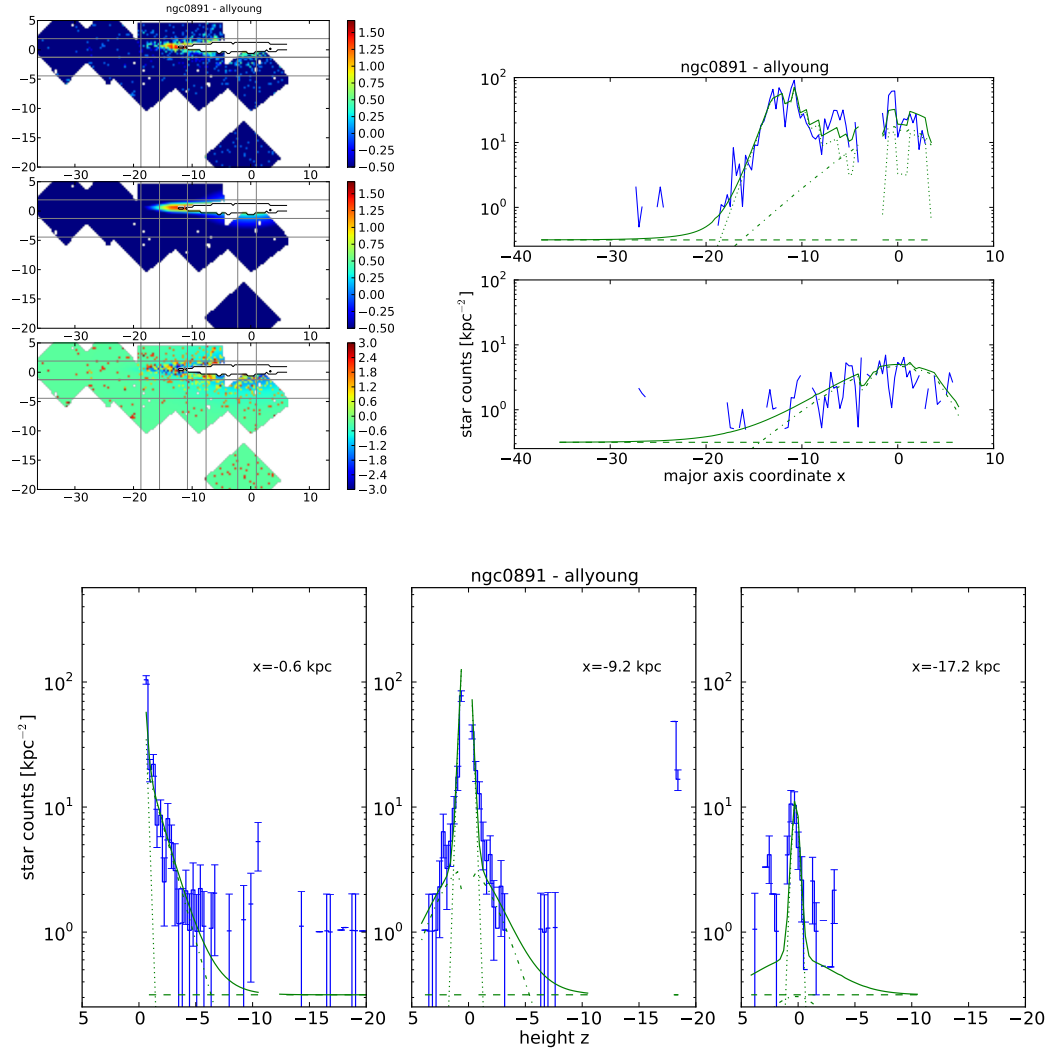
Figure C.6.: *upper left*: stellar density map of young stars in NGC 891: upper panel
- data; middle panel - model; lower panel - residuals. *upper right*: radial profiles.
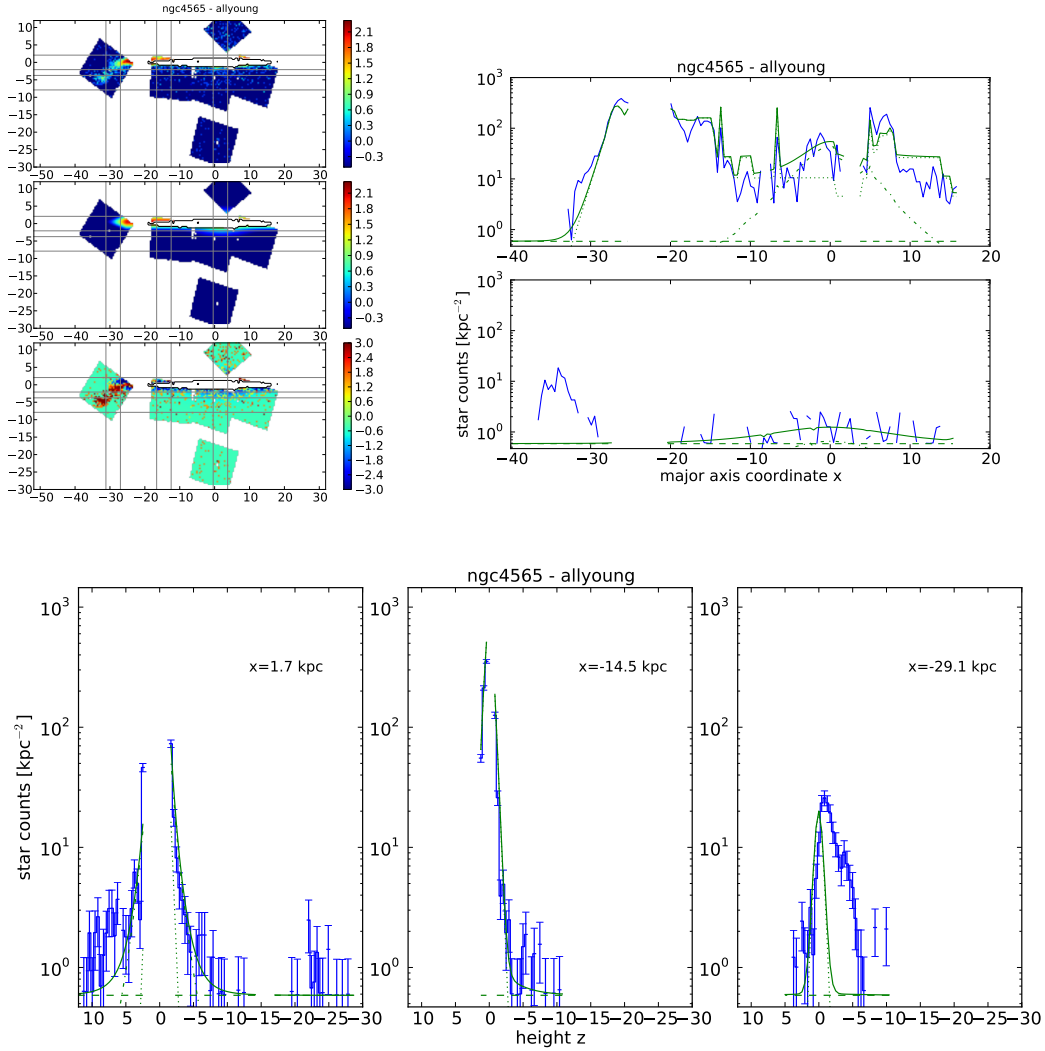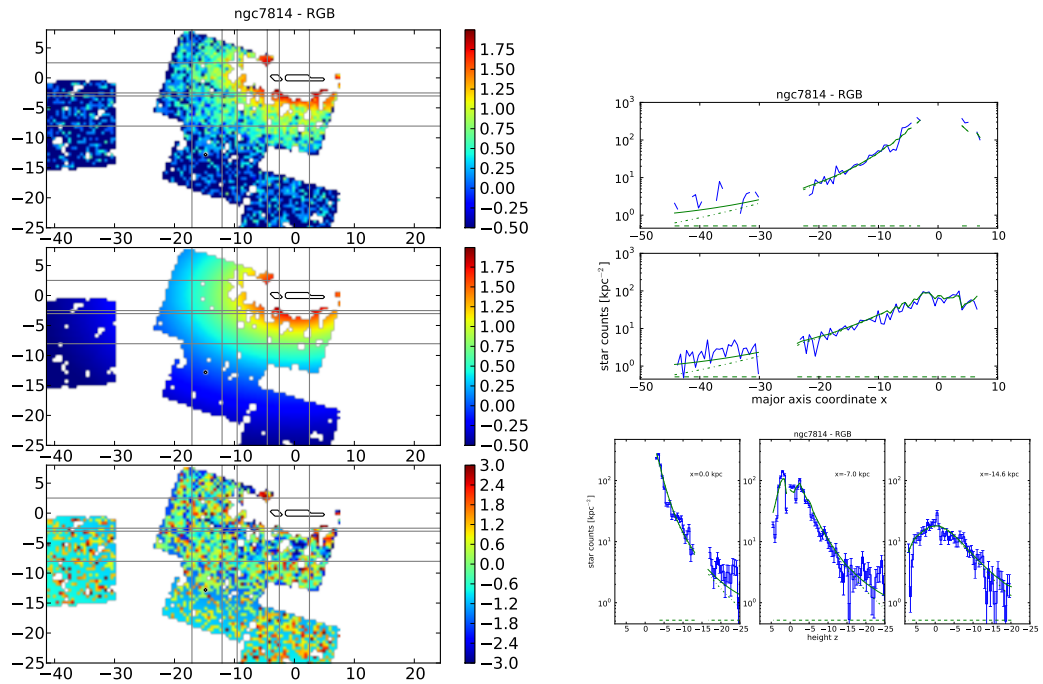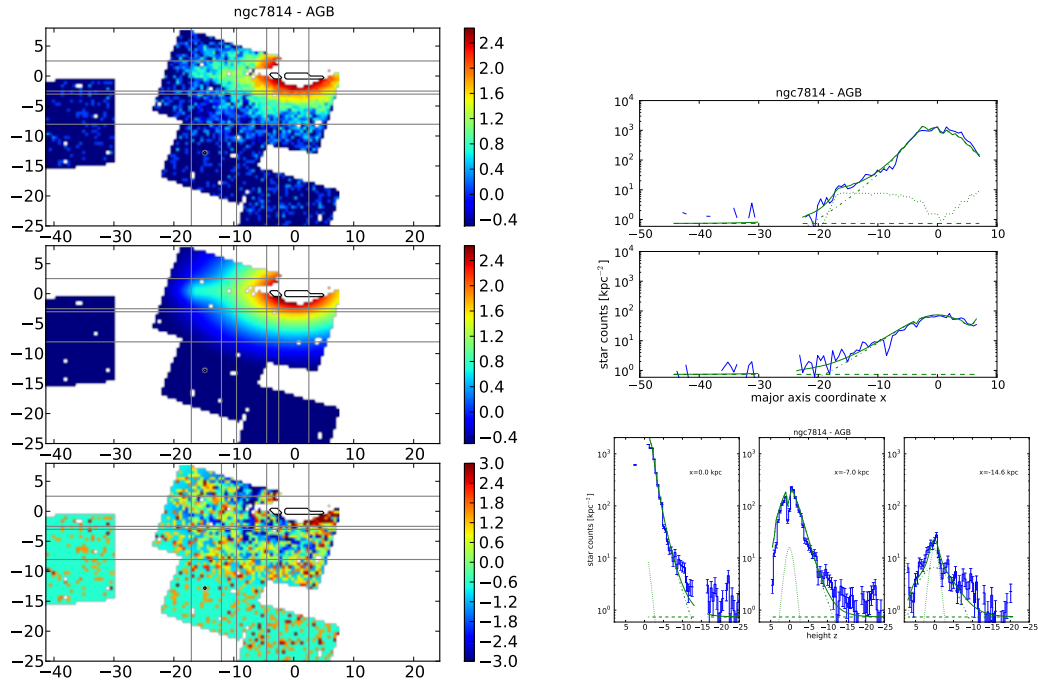*bottom*: vertical profiles.

NGC 4565
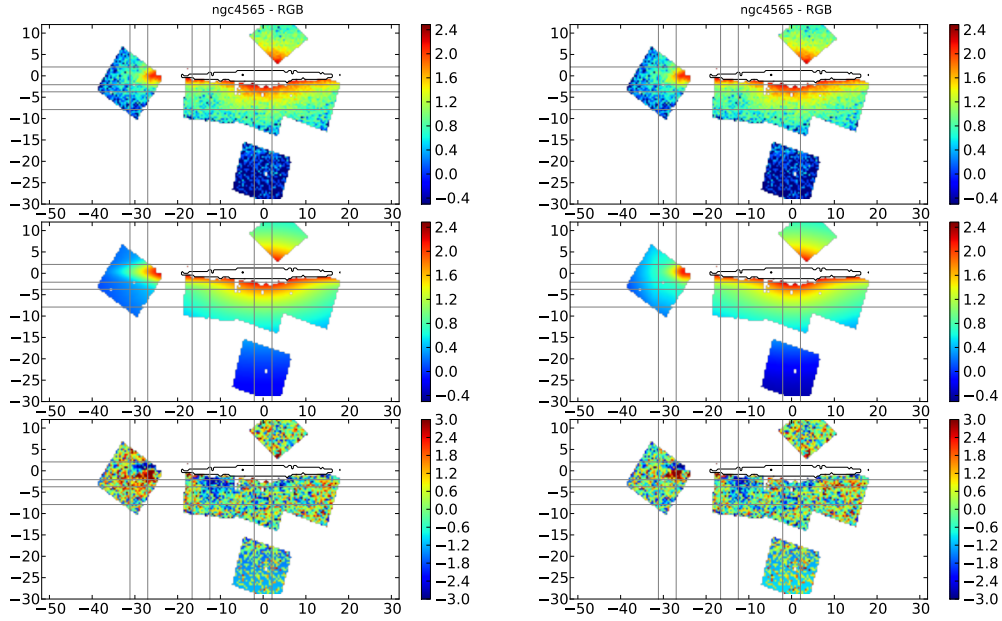
Figure C.7.: stellar density map (in logarithmic scale) of RGB stars in NGC 4565: upper panel - data; middle panel - model; lower panel - residuals. Grey lines show the edges of the bins from where the radial and vertical profiles are extracted. *Left*: model with a single disk; *right*: model with two (thin and thick) disks.

Figure C.8.: Radial profiles at two different heights. Blue shows is the data, green the model: solid – total model, dotted – disk component(s), dash-dotted – Sersic component, dashed – background. *Left*: model with a single disk; *right*:model with two (thin and thick) disks.

Figure C.9.: Vertical profiles of RGB density at three different positions in the galaxy, with the single disk 2D-models. Blue lines show the data, green the model: solid – total model, dotted – disk component(s), dash-dotted – Sersic component, dashed – background. The small panels below the profiles show the data to model ratios.

Figure C.10.: Vertical profiles of RGB density at three different positions in the galaxy, with the two disks 2D-models. Blue lines show the data, green the model: solid – total model, dotted – disk component(s), dash-dotted – Sersic component, dashed – background. The small panels below the profiles show the data to model ratios.
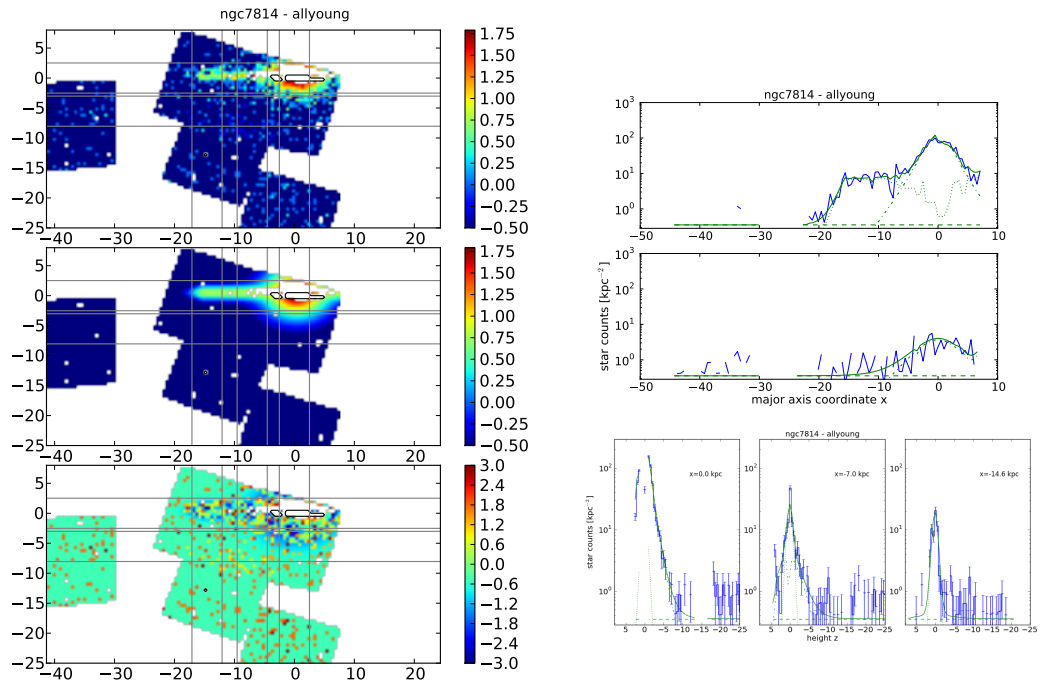
Figure C.11.: *upper left*: stellar density map of AGB stars in NGC 4565: upper panel
- data; middle panel - model; lower panel - residuals. *upper right*: radial profiles.
bottom: vertical profiles.

Figure C.12.: *upper left*: stellar density map of young stars in NGC 4565: upper panel - data; middle panel - model; lower panel - residuals. *upper right*: radial profiles. *bottom*: vertical profiles.

NGC 7814

Figure C.13.: *left*: stellar density map of RGB stars in NGC 7814: upper panel - data; middle panel - model; lower panel - residuals. *upper right*: radial profile. *lower right*: vertical profile.

Figure C.14.: *left*: stellar density map of AGB stars in NGC 7814: upper panel - data; middle panel - model; lower panel - residuals. *upper right*: radial profile. *lower right*: vertical profile.

Figure C.15.: *left*: stellar density map of young stars in NGC 7814: upper panel - data; middle panel - model; lower panel - residuals. *upper right*: radial profile. *lower right*: vertical profile.

Danksagungen - Acknowledgments

Selbstständigkeitserklärung

Hiermit versichere ich, dass ich die vorliegende Arbeit selbstständig verfasst und keine anderen als die im Literaturverzeichnis angegebenen Quellen und Hilfsmittel benutzt habe. Die Arbeit wurde an keiner weiteren Universität eingereicht.

Potsdam, den 20. März 2015

David Streich